NUMERICAL AND EXPERIMENTAL APPLICATIONS OF INVERSE FINITE ELEMENT METHOD FOR SHAPE AND STRESS SENSING OF SHELL STRUCTURES

By

Mohammad Amin Abdollahzadeh

Submitted to the Graduate School of Engineering and Natural Sciences

in partial fulfillment of

the requirements for the degree of

Doctor of Philosophy

Sabanci University

July 2022

NUMERICAL AND EXPERIMENTAL APPLICATIONS OF INVERSE FINITE ELEMENT METHOD FOR SHAPE AND STRESS SENSING OF SHELL STRUCTURES

Mohammad Amin Abdollahzadeh

Ph.D. Dissertation, July 2022

Supervisor: Asst. Prof. Dr. Adnan Kefal

Co-Supervisor: Prof. Dr. Mehmet Yildiz

ABSTRACT

Keywords: Structural health monitoring, shape sensing, shell structures, inverse finite element method

Plate and shell structures are used in many industries, including marine, aerospace, automotive, energy, and petrochemical. The condition of these components is of great importance as they directly affect the health status of people and the environment. Therefore, implementing a reliable structural health monitoring (SHM) system is paramount to ensuring the structural integrity of these applications. Shape sensing is an important part of SHM that deals with the real-time reconstruction of structural displacements and stress fields using a network of strain gages. Shape sensing is an inverse problem, and the inverse finite element method is one of the best candidates to solve this problem in real-time. This dissertation aims to further evaluate the iFEM approach by comparing the efficiency and accuracy of the existing iFEM plate/shell elements. Additionally, an improved iFEM element is developed for better shape sensing of thick and moderately thick sandwich and multilayer composites. The capability of the iFEM method for shape sensing of thin-walled structures subjected to geometrically nonlinear deformations is investigated in this thesis as well. Finally, the potential of the iFEM method for shape sensing of structural components in the marine and aerospace industries is explored. The results of these investigations have been published in three journal papers and two conference proceedings, which are presented individually in four chapters of this study.

ÖZET

Plaka ve kabuk yapılar, denizcilik, havacılık, otomotiv, enerji ve petrokimya dahil olmak üzere birçok endüstride kullanılmaktadır. Bu yapıların mekanik durumu, insanların ve çevrenin sağlık kondisyonunu doğrudan etkiledikleri için büyük önem taşımaktadır. Bu nedenle, güvenilir bir yapısal sağlık izleme (SHM) sisteminin uygulanması, bu yapıların yapısal bütünlüğünü sağlamak için çok önemlidir. Şekil algılama, birçok gerinim sensörü kullanarak yapısal yer değiştirmelerin ve gerilim alanlarının gerçek zamanlı yeniden yapılandırılmasıyla ilgilenen SHM'nin önemli bir alanıdır. Şekil algılama tersten algoritma ile çalışan bir yöntemdir ve ters sonlu elemanlar yöntemi (iFEM), bu problemi gerçek zamanlı olarak çözmek için en iyi yaklaşımlardan biridir. Bu tez, mevcut iFEM plaka/kabuk elemanlarının verimliliğini ve doğruluğunu karşılaştırarak iFEM yaklaşımını daha fazla değerlendirmeyi amaçlamaktadır. Ek olarak, kalın ve orta kalınlıkta sandviç ve çok katmanlı kompozitlerin daha iyi şekil algılaması için geliştirilmiş bir iFEM elemanı geliştirilmiştir. Bu tezde, geometrik olarak doğrusal olmayan deformasyonlara maruz kalan ince duvarlı yapıların şekil algılaması için iFEM yönteminin yeteneği de araştırılmıştır. Son olarak, denizcilik ve havacılık endüstrilerinde yapısal bileşenlerin şekil algılaması için iFEM yönteminin potansiyeli araştırılmaktadır. Bu araştırmaların sonuçları, bu çalışmanın dört bölümünde ayrı ayrı sunulan üç dergi makalesinde ve iki konferans bildirisinde yayınlanmıştır.

ACKNOWLEDGEMENT

I would like to express my deepest gratitude to my supervisor Asst. Prof. Dr. Adnan Kefal for his sincere encouragement, continuous support, and admirable advice throughout the research and for giving me the opportunity to explore various aspects of the field of computational mechanics and composite materials.

A very special thanks to my co-supervisor Prof. Mehmet Yildiz for his guidance, encouragement, and excellent advice throughout the research.

My special thanks to my dear friends and supporters during these years, Shayan Ramezanzadeh, Pouya Zoughipour, Roozbeh Saghatchi, Vahid Charkhesht, Kamal Asadi Pakdel, Isa Emami Tabrizi, Emre Komurcu, Fatih Uzun, Fatih Basoglu, Raja Muhammad Awais Khan, Hafiz Qasim Ali and Baidaa Alkhateab.

I am very grateful to my parents and wife for their immense love and care. They have always encouraged me to discover my potential and motivated me to pursue my dreams. They have sacrificed a lot for me to reach this stage in my life.

The financial support provided by the Scientific and Technological Research Council of Turkey (TUBITAK) under the grant No: 217M207 and No: 5200082 are greatly acknowledged.

Finally, I would like to thank Sabanci University and SU-IMC for their support in allowing me to conduct this research over the past years.

Dedicated to

To my father, whose determination is as strong as the mountain,

To my mother, whose heart is as big as the ocean, and

To my endless love and lovely wife, Shima

TABLE OF CONTENTS

LIST OF FIGURES

LIST OF TABLES

CHAPTER 1. General Introduction

1.1. A Statement of Problem

Plate and shell-like structures have a large share in the manufacturing of industrial technology, such as marine, aerospace, and automotive. These structural components are mainly exposed to harsh environmental and operational situations, which can cause damage to these components. When damage accumulates, catastrophic failure of the entire structure can occur, resulting in human casualties, environmental damage, and economic losses. Therefore, continuous monitoring is required to ensure the integrity of these structural components. Structural Health Monitoring (SHM) performs this task by integrating sensing systems into these types of structural components and collecting and processing the data to provide real-time information about their health state.

Shape and stress sensing is a key SHM technology that deals with real-time reconstruction of structural displacements and stress fields using a network of strain gages. Shape sensing is an inverse problem. To solve this inverse problem, several mathematical algorithms have been developed and presented in the literature. Tikhonov and Arsenin [1] introduced a regularization term that ensures a safe degree of smoothing to solve this inverse problem. Most inverse methods use more or less the same regularization form. For example, Maniatty et al [2] used regularization techniques to solve inverse elastic and elastoviscoplastic problems. In addition, Schnur and Zabaras [3] computed the surface tractions of a body from a discrete number of sensors providing internal displacements at the sensor positions. They then minimized the difference between the computed and measured displacements by employing a spatial regularization to solve this inverse problem. The spatial regularization has the role of stabilizing of the minimization process. Maniatty and Zabaras [4] also tried to estimate the errors in solving an inverse problem using coupled the spatial regularization technique with a statistical approach discussed by Tarantola [5]. In addition to inverse methods using a type of Tikhonov regularization, a variety of shape recognition algorithms have been proposed to solve real-time reconstruction of displacements in beam and/or plate structures subjected to bending loads [6-13]. Most of the aforementioned inverse methods do not take into account the complexity of the boundary conditions and structural

topology. They are also dependent to sufficient and accurate loading and material information about the structure. Furthermore, due to their inherent assumptions many of these methods are not capable to adapted to dynamic loads and nonlinear displacements and are limited to static and/or quasi-static loads. Finally, most of these inverse methods require time-consuming analysis and are therefore not suitable for real-time SHM systems. Considering all these drawbacks, they are generally not suitable for use in on-board SHM algorithms.

The inverse finite element method (iFEM) is a state-of-the-art method originally introduced by Tessler and Spangler [14-15] for real-time shape sensing of plate and shell structures. The general mathematical concept of the iFEM method uses a least squares variational principle that attempts to minimize the errors between the analytical and corresponding experimental strain values. To calculate the required analytical strain values, the iFEM formulation is performed using first-order shear deformation theory (FSDT), including the membrane, bending curvatures, and transverse shear strain measures. However, the experimental strain values are obtained using a series of strain sensors located on board or embedded in the structures. It is worth noting that simulated strain data obtained using numerical analysis methods (e.g., FEM) can be used in place of experimental strain values when evaluating the shape sensing of complex geometries. The minimization process leads to a system of linear algebraic equations that can be solved to determine the unknown displacements in real-time. Once the displacement field is reconstructed, the strains throughout the field can be calculated using the strain-displacements relationships. Then, the three-dimensional stress state of the structure can be calculated using the full-field strains and the material properties of the structure. Finally, the three-dimensional stresses can be fitted to an equivalent stress using an appropriate failure criterion (e.g., von Mises yield criterion), allowing real-time damage predictions.

1.2. Objectives of the Research

The current Thesis has four main objectives as follows:

1. To compare the accuracy and performance of shape and stress sensing between existing inverse elements for plates/shells in the literature (i.e., iMIN3, iQS4 and iCS8). In this review study, this objective is achieved by evaluating four benchmark problems consisting of a wing-shaped plate, a curved shell, a stiffened curved shell,

and a curved shell with a degraded part in the center. The last case aims to compare the accuracy of the detection of damages by iFEM elements. To the best of authors' knowledge this is the first time in the literature that a comparative and review study investigates the shape and stress sensing and damage prediction performance of different iFEM inverse elements. These objectives are achieved in Abdollahzadeh et al. [16] as part of the research described in this thesis (Chapter 2).

2. For deformation sensing of thick and moderately thick sandwich composite plate and shell structures numerically and experimentally using novel RZT-based iFEM elements (i.e., iRZT4). This study also investigates the performance of the new iFEM-RZT element in reconstructing torsional deformations in multilayer structures. In addition, a polynomial smoothing method is coupled with the iFEM-RZT approach in this study to produce a continuous form of the experimental strain data over the entire region of the laminated structure. As far as the authors are aware, there is no study in the literature that considers these aspects. The results of this study were published in Abdollahzadeh et al. [17] as part of the research described in this thesis (Chapter 3).

3. To numerical and experimental investigation of iFEM's ability to reconstruct large deformations of thin laminated plate and shell composite structures. In this context, geometrically nonlinear deformations of thin composite structures subjected to bending and/or post-buckling loads are evaluated using the inverse element iFEM-iQS4. Also, a technique for pre-extrapolation of strains is applied to obtain a more uniform variation of strains over the whole area of the plate. The overall strategy of this study is in Abdollahzadeh et al [18]. which is presented in Chapter 4 of the dissertation. To the best of the authors' knowledge, this is the first time that thin laminated structures subjected to large deflections have been evaluated using the iFEM method.
4. To Discuss numerical applications of the inverse finite element method for shape sensing of structural components in the marine, aerospace, and automotive industries. To this end, three-dimensional shape sensing of an aircraft fuselage and a representative ship hull structure are considered, and analyzed using the iFEM-iQS4

inverse shell element. The capability of iFEM analyzes in case of loss (damaged/broken) a set of strain data is also demonstrated in this study. To the best of the authors' knowledge, no previous iFEM study has been performed in this context. These objectives are achieved in Abdollahzadeh et al [19-20] as part of the research in this thesis (Chapter 5).

1.3. Description of Remaining Chapters

The remaining parts of this thesis is constituted by the following chapters:

- Chapter 2: In this chapter, the existing inverse elements are compared in terms of their capability of full-field displacement and stress reconstruction and damage prediction. The general mathematical formulation of these inverse elements is briefly explained and the fundamental differences in the associated shape functions of these elements are thoroughly examined.

- Chapter 3: This chapter presents advantages of a new four-node RZT based iFEM element for shape sensing of moderately thick sandwich plate/shell composites. The mathematical formulation of this element is described in detail. This evaluation is completed using two numerical examples. Consequently, one experimental example is done to validate the numerical analyses.

- Chapter 4: This chapter describes the ability of iFEM to investigate thin laminated structures subjected to large deformations (geometrically nonlinear deformations). The mathematical formulation and numerical/experimental examples serve to elucidate the topic of interest.

- Chapter 5: This chapter aims to discuss numerical applications of iFEM for shape sensing of structural components in the fields of marine and aerospace engineering. For this purpose, two complex geometries are considered to model the representative shape of an aircraft fuselage and a ship hull structure. In this chapter also the iFEM formulation is briefly discussed.

- Chapter 6: This chapter summarizes the main findings, highlights the novelty and contribution of this research study to the field, discusses the gaps and suggests future work, and concludes with concluding remarks.

CHAPTER 2. A Comparative Study on Shape and Stress Sensing of Flat/Curved Shell Geometries Using C0-Continuous Family Of iFEM Elements

In this chapter, we methodologically compare accuracy and performance of C0-continuous flat and curved inverse-shell elements (i.e., iMIN3, iQS4, and iCS8) for inverse finite element method (iFEM) in terms of shape, strain, and stress monitoring, and damage detection on the various plane and curved geometries subjected to different loading and constraint conditions. For this purpose, four different benchmark problems are proposed, namely, a tapered plate, a quarter of a cylindrical shell, a stiffened curved plate, and a curved plate with a degraded material region in stiffness, representing damage. The complexity of these test cases is increased systematically to reveal the advantages and shortcomings of the elements under different sensor density deployments. The reference displacement solutions and strain-sensor data used in the benchmark problems are established numerically utilizing direct finite element analysis. After performing shape-, strain-, and stress-sensing analyses, the reference solutions are compared with the reconstructed solutions of iMIN3, iQS4, and iCS8 models. For plane geometries with sparse sensor configurations, these three elements provide rather close reconstructed-displacement fields with slightly more accurate stress sensing using iCS8 than iMIN3/iQS4. It is demonstrated on the curved geometry that cross-diagonal meshing of a quadrilateral element pattern (e.g., leading to four iMIN3 elements) improves the accuracy of the displacement reconstruction as compared to single-diagonal meshing strategy (e.g., two iMIN3 elements in a quad-shape element) utilizing iMIN3 element. Nevertheless, regardless of any geometry, sensor density, and meshing strategy, iQS4 performs better shape and stress sensing than iMIN3. As the complexity of the problem is elevated, the predictive capabilities of the iCS8 element become obviously superior to that of flat inverse-shell elements (e.g., iMIN3 and iQS4) in terms of both shape sensing and damage detection. Comprehensively speaking, we envisage that the set of scrupulously selected test cases proposed herein can be reliable benchmarks for testing/validating/comparing for the features of newly developed inverse elements.

2.1. Introduction

Thin shell structures with monolithic/stiffened curved and flat geometries are commonly utilized in diverse engineering applications including ships and marine platforms, aerospace vehicles, and civil structures, among others. These structures should be strong enough to bear not only their own weights but also extreme environmental loads such as high wind pressure, catastrophic ocean waves, and rainstorms without losing their structural integrity. These loads may result in material degradations due to the formation of cracks, voids, and stress intensification locations. In addition to the load-induced damages, the corrosive environmental conditions encourage the occurrence of additional failure modes including stress-corrosion cracking, fretting cracks, and thickness reductions due to material erosion. Structures operating under these conditions eventually experience sudden failures and ruptures in their primary components, hence being rendered useless. Besides, sudden damages lead to economic loss, environmental pollution, and even may cause human casualties. To prevent such events and predict these undesirable damages in real-time, a structural health monitoring (SHM) system with a reliable and robust displacement and stress monitoring capabilities should be installed in the structures aboard [21-23].

SHM is a multidisciplinary technology that can provide a real-time estimation of strain and stress fields, overall structural deformations, and damage positions through utilizing ensemble of sensors discretely located on/in the structure acquiring physical/mechanical information such as strain, temperatures, acceleration, pressure, etc. Over the last few decades, significant progress has been made in different forms of SHM technologies for various material and structural systems [24-25]. Damage detection of cracked shell structures [26-27]. SHM of simple and complex structural topologies made of isotropic materials (e.g., steel/aluminum structures [22-23, 28]) or orthotropic materials (e.g., multilayered composite and sandwich structures [29-30]) are studied under static and dynamic loading conditions. Particularly, damage, delamination, and fatigue in laminated composite and foam-core sandwich structures were identified using embedded fiber optic sensors [31-33].

Apart from the conventional SHM approaches, a significant amount of attention has been dedicated towards the real-time reconstruction of the structurally deformed shapes via strain sensors, i.e., a key technology for SHM systems, commonly referred to as

"displacement monitoring" or "shape sensing". Mathematically speaking, shape sensing is an inverse problem. For the solution of this inverse problem, various mathematical formulations and algorithms have been proposed and investigated experimentally and/or numerically for beam/plate/shell structures. In general, these algorithms can be classified in the following two main categories: (1) modal/analytical/curve-fitting approaches [14-19], and (2) inverse finite element method (iFEM) [20-21]. Davis et al. [6] used analytical trial functions for shape and vibration mode sensing in order to regenerate static-beam response using fiber Bragg grating (FBG) sensor data. The main drawback of their approach is the requirement of excessive numbers of strain sensors and trial functions to model complex modal shapes. Kang et al. and Bogert et al. [7-8] evaluated the dynamic response of a beam- or plate-like structure through computing modal coordinates using strain-displacement relationship and discrete strain measurements obtained from surface-mounted FBG sensors. However, since the numbers of estimated mode shapes are restricted to the numbers of strain sensors, the accuracy of their approach may diminish for shape sensing under dynamically complex loading conditions, thus limiting the generality of this approach. Kim and Cho [11] analytically approximated the deflection of a beam using a high-order polynomial function whose weights were found through curve fitted experimental strains. Ko et al. [12] generalized Kim and Cho's approach further and demonstrated its implantation to shape sensing of a wing-shaped beam model with airfoil cross-section subjected to bending deformations. However, the approaches [37-38] are bereft of predicting accurate torsional deformations due to the simplifications made in the kinematic relations utilized in the model. Chierichetti [39] introduced a non-linear numerical method called load confluence algorithm (LCA) which requires the numerical estimation of force before reconstructing the dynamic response of a beam. Nevertheless, since the LCA approach first reconstructs the loads, the statistical complexity of the loading condition may lead to undesirable errors in the prediction of the displacement field. Overall, the above-stated shape-sensing methods encounter difficulties in dealing with structures with complex geometries and boundary conditions, and hence cannot be easily generalized for shape sensing of any structures.

Among these inverse-methods, the iFEM methodology has been demonstrated to be the most-general shape-sensing algorithm because of its mathematical attributes, i.e., the utilization of a least-squares variational principle based on experimental and numerical

strain-displacement relations [40-41]. In other words, this variational principle relies on the minimization of the squared norm errors between experimentally measured and numerically evaluated section strains. For a given structure, the experimental section strains can be calculated by using tri-axial surface strains obtained from strain rosettes that can be in the form of FBGs or conventional strain gauges. The numerical counterparts of such section strains can also be readily established for an infinitesimally small domain, i.e., an inverse finite element. The minimization of the iFEM least-squares functional with respect to the unknown displacements enables one to cast the final set of equations in a matrix-vector form, which can be solved through imposing problem-specific constraint boundary conditions into the final equations. Such a solution first reveals the full-field structural displacements, leading to shape sensing in three-dimensional space. In the post-processing stage, the solution of the displacement field can be transformed into the strains via strain-displacement relations. Finally, the constitutive relations of a given material can be used to evaluate the individual stress components, leading to stress monitoring in the framework of iFEM methodology. To recapitulate, the potential advantages of iFEM algorithm can be stated concisely as; (1) the independence from the external loads, (2) the suitability for modeling the complex structural geometries with intricate constraints, (3) the utilization of only discrete strain measurements without needing material information, and (4) the applicability to real-time analysis [22-23].

The iFEM methodology was first introduced for plate structures based on the kinematic relations of first-order shear-deformation theory (FSDT) [15]. Then, its original variational principle was adapted to the Timoshenko beam theory for shape sensing of beam structures [34], which is validated against experimental studies [35-37]. Subsequently, the FSDT-based iFEM formulation was extended to the utilization of the zigzag kinematics of refined zigzag theory (RZT) [38] for shape sensing of composite structures [39-41]. Since the iFEM formulation requires discretization of the structural domain with inverse elements, various inverse beam-, plate- and shell elements were developed. The FSDT-based iFEM elements available in literature includes a three-node triangular inverse-shell element (iMIN3) [42], a four-node quadrilateral inverse-shell element (iQS4) [43], and an eight-node curved quadrilateral inverse-shell element (iCS8) [44]. All these elements possess C0-continuous shape functions. In particular, both iMIN3 and iQS4 utilize the first-order anisoparametric shape functions developed for a triangle [45] and quadrilateral [46] finite elements,

respectively. Such anisoparametric functions were obtained through imposing Tessler-Dong [47] constant shear-edge conditions along the element boundaries. On the other hand, the iCS8 element employs the Lagrangian serendipity (isoparametric) shape functions of an eight-node quadrilateral element [48]. So far, the iMIN3 element was extensively scrutinized for numerical and experimental shape-sensing applications of plate structures with and without large deformations [49-50]. Besides, the iQS4 was numerically demonstrated to be a practical element in modeling and obtaining accurate sensor configurations for displacement monitoring of complex marine structures such as bulk carriers, chemical tankers, and offshore structures, among others [51-54]. As for the iCS8 element, its potential benefit for shape sensing of curved geometries with a low number of sensor measurements was demonstrated on curved marine structures [55]. Although iQS4 was demonstrated to be applicable accurately for shape sensing of slender composite structures [56], it is prudent to state that there exist other iFEM elements mainly implemented for thick sandwich structures, such as RZT-based inverse-plate/shell elements [39-40, 57].

To the best of author's knowledge, none of the previous research on the iFEM includes an extensive comparison of the C^0-continuous inverse-shell elements (i.e., iMIN3, iQS4, iCS8) in terms of their efficiency and accuracy for shape sensing of the various geometries with sparse and/or dense sensor deployments. Moreover, the original studies of these inverse-shell elements [42-44] do not include any systematic investigation on the validation of elements through analyzing benchmark geometries ranging from simple to complex features with/without any material degradation. In this study, the aforementioned issues in the literature are addressed through performing various shape-sensing analyses of the plane, curved, monolithic, and stiffened engineering geometries with these three iFEM shell elements. Therefore, the original contribution of this study to the existing state-of-the-art includes not only the comparison of three inverse-shell elements but also provides benchmark solutions, which can be used for the development of application-specific new inverse-element types. Since the fundamental kinematic relations of these three inverse elements are implemented based on FSDT, the iFEM weighted-least-squares functional of each element contains the contributions of the membrane, bending, and transverse-shear section strains, thereby allowing for a quantitative comparison among these three elements. To do so, the same geometry is discretized using the same number of elements, and also the same path of

sensor lines is followed with the same number of sensor measurements. In addition, different sparse sensor placement strategies are examined with the aim of achieving the most practical and economical number of sensors in the discretization domain. Overall, four different plane/curved geometries, e.g., flat, curved, stiffened curved, and curved with material degradation, having different loading and constraint condition are analyzed as the benchmark cases. For the last benchmark, an eye-shaped domain in the center of the curved plate is modeled as a material with degenerated (damaged) mechanical properties. With this problem, the damage detection capabilities of the C^0-continuous inverse-shell elements are also explored based on the same damage-detection criterion [58-59], thus providing benchmark guidance on the selection of iFEM shell elements as a part of SHM.

2.2. The iFEM Formulation based on FSDT

The iMIN3, iQS4, and iCS8 inverse-shell elements are the three main iFEM discretization units used in the literature to perform shape sensing of plate-like structural components in engineering applications. The displacement definitions of all these elements are based on the kinematic relations of the FSDT. The iMIN3 is the first inverse-shell element introduced in the literature [42] and possesses a flat triangular geometry containing three-nodes with six degrees of freedom (DOF) per each node as shown in Fig. 2-1(c). Although this inverse element has shown to be a good candidate to model structures with arbitrary shapes, the discretization of a complex geometry may require a higher number of elements as compared to quad-shaped inverse-elements, hence requiring utilization of more strain sensors. An alternative to the iMIN3 element, one may prefer to use a four-node quadrilateral inverse-shell element (iQS4) [43] for the discretization of complex geometry with a lower number of elements. Similar to the iMIN3 element, the iQS4 also has a flat geometry with each node containing six DOF, i.e., the positive translational and rotational directions depicted in Fig. 2-1(a). For modeling complex geometries, the main advantage of using both iMIN3 and iQS4 is associated with the inclusion of the drilling rotation, which prevents the singularity issues in case of discretizing a built-up structural geometry and enables a better shape-sensing capability for membrane deformations. Apart from these elements, an eight-node inverse curved shell element, iCS8, was introduced to tackle shape sensing of curved structural members [44]. Unlike iMIN3 and iQS4, the in-plane geometry of this new element

is constructed using curvilinear coordinates of ξ and η as shown in Fig. 2-1(b), whereas the thickness coordinate, ζ, is rectangular to the in-plane coordinates along with the thickness of the element.

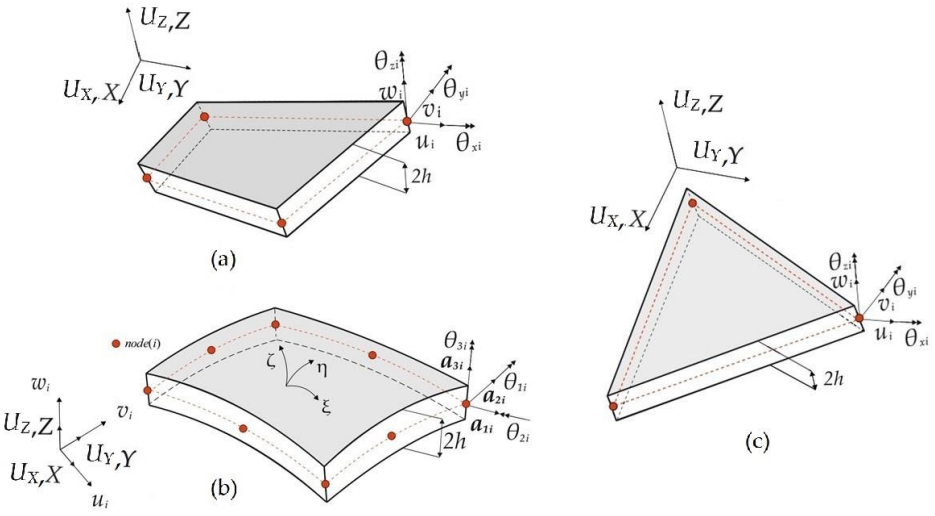

Fig. 2-1. Geometries of (a) iQS4, (b) iCS8, and (c) iMIN3 inverse-shell elements with associated global and local coordinate systems as translational and rotational DOF.

Each node of the iCS8 contains three translational DOF defined according to a global rectangular Cartesian coordinate system. Moreover, there are two local rotational DOFs employed to construct the kinematics relations suitable for FSDT. Furthermore, an artificial drilling rotation is included in the displacement relations to avoid singular solutions when modeling stiffened curved geometries. The main advantage of iCS8 can be attributed to its geometrically conforming nature to the structures with lower mesh density. Overall, the iMIN3 and iQS4 elements utilize second-order anisoparametric shape functions to interpolate the translational kinematic variables, whereas the iCS8 element use second-order (Lagrangian serendipity) isoparametric shape functions to approximate the displacement components. The detailed mathematical definitions corresponding to shape functions, displacement approximations, and displacement-strain relations about the inverse elements studied herein can be found in [42-44]. Once the displacement field of each individual element is determined, the strain components at any point of the plate/shell domain can be analytically calculated in terms of the nodal displacement vector, $\mathbf{u}^e$, of an element as:

$$\left[\boldsymbol{\varepsilon} \quad \boldsymbol{\gamma}\right] \equiv \left[\boldsymbol{\varepsilon}(\mathbf{u}^e) \quad \boldsymbol{\gamma}(\mathbf{u}^e)\right] = \left[\mathbf{B}^{\varepsilon}\mathbf{u}^e \quad \mathbf{B}^{\gamma}\mathbf{u}^e\right] \tag{1a}$$

$$\mathbf{u}^e = \left[\mathbf{u}_1^e \quad \mathbf{u}_2^e \quad \cdots \quad \mathbf{u}_n^e\right]^T \tag{1b}$$

where the $\boldsymbol{\varepsilon}$ and $\boldsymbol{\gamma}$ vectors represent the in-plane and transverse-shear strains, respectively. In Eq. (1b), the subscript n denotes the number of nodes of an individual element, e.g., iMIN3, iQS4, and iCS8. Moreover, the $\mathbf{B}^{\varepsilon}$ and $\mathbf{B}^{\gamma}$ matrices contain the derivative of the shape functions associated with the displacements corresponding to membrane-bending and transverse-shear deformations, respectively. Note that, for flat inverse-elements, coupled membrane-bending response can be easily described as the sum of the membrane and bending section strains as:

$$\boldsymbol{\varepsilon}(\mathbf{u}^e) = \mathbf{e}(\mathbf{u}^e) + z\boldsymbol{\kappa}(\mathbf{u}^e) = (\mathbf{B}^m + z\mathbf{B}^b)\mathbf{u}^e = \mathbf{B}^{\varepsilon}\mathbf{u}^e \tag{2}$$

where the vectors $\mathbf{e}(\mathbf{u}^e)$ and $\boldsymbol{\kappa}(\mathbf{u}^e)$ represent the membrane strains and bending curvatures in the given order. The strain-displacement relation matrices, $\mathbf{B}^m$ and $\mathbf{B}^b$, corresponding to these individual section strains were explicitly provided for flat iMIN3 and iQS4 elements in [42-43]. Such decoupled form of strain definition (i.e., Eq. 2) may require cumbrous mathematical partitions for the iCS8. The explicit form of $\mathbf{B}^{\varepsilon}$ matrix for the curved iCS8 element can be found in reference [44].

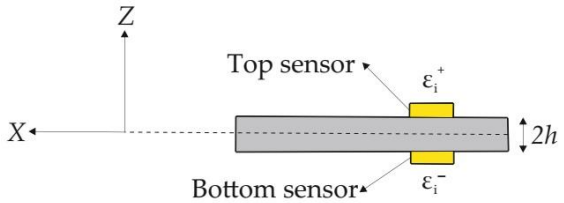

Fig. 2-2. Experimental strain data collected from the top and bottom surfaces of a plate structure.

The main input of the iFEM methodology is the experimental strain measurements collected from the onboard strain sensors located at discrete positions of a given plate/shell-like structure as shown in Fig. 2-2. Consider that the $\boldsymbol{\varepsilon}_i^+$ and $\boldsymbol{\varepsilon}_i^-$ experimental surface strains are collected from top ($z = +h$) and bottom ($z = -h$) thickness coordinates of different in-plane positions, $\mathbf{x}_i$ $(i = 1, 2, ...n_s)$. Herein, the '+' and '-' superscripts are used to denote top and bottom surfaces, respectively, and the n_s indicates the number of strain rosettes available

on either bounding surface. Using these in-situ surface strains, the experimental counterparts of the numerical strain data can be calculated as:

$$\left[\mathbf{e}_i^{\varepsilon} \quad \boldsymbol{\kappa}_i^{\varepsilon}\right] \equiv \left[\frac{1}{2}(\boldsymbol{\varepsilon}_i^{+} + \boldsymbol{\varepsilon}_i^{-}) \quad \frac{1}{2h}(\boldsymbol{\varepsilon}_i^{+} - \boldsymbol{\varepsilon}_i^{-})\right] \quad (i = 1, 2, ..., n_s) \tag{3}$$

where the $\mathbf{e}_i^{\varepsilon}$ and $\boldsymbol{\kappa}_i^{\varepsilon}$ vectors represent the experimental counterparts of the membrane, $\mathbf{e}(\mathbf{u}^e)$, and bending, $\boldsymbol{\kappa}(\mathbf{u}^e)$, section strains given in Eq. (2), respectively. Such experimental strains can be combined together to obtain a coupled membrane-bending section strain experimentally as:

$$\boldsymbol{\varepsilon}_i^{\varepsilon} = \mathbf{e}_i^{\varepsilon} + z\boldsymbol{\kappa}_i^{\varepsilon} \equiv \mathbf{e}_i^{\varepsilon} + \zeta h\boldsymbol{\kappa}_i^{\varepsilon} \quad (i = 1, 2, ..., n_s) \tag{4}$$

where the $\boldsymbol{\varepsilon}_i^{\varepsilon}$ vector represents the experimental counterpart of the $\boldsymbol{\varepsilon}(\mathbf{u}^e)$ strains measured at the positions of $\mathbf{x}_i$, i.e., continuous along with the thickness coordinates, $\zeta \in [-1,1]$, $z \in [-h,h]$. Experimental transverse shear strains, $\boldsymbol{\gamma}^{\varepsilon}$, cannot directly be obtained from the $\boldsymbol{\varepsilon}_i^{+}$ and $\boldsymbol{\varepsilon}_i^{-}$ measurements. Nevertheless, when performing shape sensing of slender structures, the contributions of transverse-shear strains to bending deformations can be safely omitted. Based on experimentally measured and the numerically calculated section strains, the weighted least-squares functional of iFEM methodology can be defined for shape-sensing simulations by using iMIN3, iQS4, and iCS8 elements as:

$$\Phi(\mathbf{u}^e) = \frac{1}{V}\int_V \left(w_{\varepsilon} \left\| \boldsymbol{\varepsilon}(\mathbf{u}^e) - \boldsymbol{\varepsilon}^{\varepsilon} \right\|^2 + w_{\gamma} \left\| \boldsymbol{\gamma}(\mathbf{u}^e) - \boldsymbol{\gamma}^{\varepsilon} \right\|^2 \right) dV \tag{5}$$

where the V parameter represents the volume of an individual inverse-shell element, w_{ε} and w_{γ} are the weighting coefficients associated with the in-plane and transverse-shear strains. These coefficients can be set to unity, $w_{\varepsilon} = w_{\gamma} = 1$, if both experimental measurements, $\boldsymbol{\varepsilon}^{\varepsilon}$ and $\boldsymbol{\gamma}^{\varepsilon}$, exist within a given inverse element. Otherwise, they should be set to a small number compared to unity, such as $w_{\varepsilon} = w_{\gamma} = 10^{-4}$, in case of a missing experimental section strain in the element domain. More details on the weighting coefficient selection strategies can be found in subsection 3.1. Minimizing the $\Phi(\mathbf{u}^e)$ functional with respect to the unknown $\mathbf{u}^e$

displacements of an inverse element, the compact form of final equation set can be obtained as:

$$\frac{\partial \Phi(\mathbf{u}^e)}{\partial \mathbf{u}^e} = \mathbf{k}^e\mathbf{u}^e - \mathbf{f}^e = 0 \Rightarrow \mathbf{k}^e\mathbf{u}^e = \mathbf{f}^e \tag{6}$$

where the $\mathbf{k}^e$ and $\mathbf{f}^e$ are local analytical shape matrix and local experimental shape vector in the given order. The explicit forms of these quantities for iMIN3, iQS4, and iCS8 elements were provided in [42-44]. These local equations given in Eq. (6) can be transformed into a global Coordinate system by using an appropriate transformation matrix, $\mathbf{T}^e$, and then can be assembled for a given discretization composed of N_{el} number of the inverse element as:

$$\mathbf{KU} = \mathbf{F} \tag{7a}$$

$$\mathbf{K} = \bigcup_{e=1}^{N_{el}} \left[(\mathbf{T}^e)^T \mathbf{k}^e \mathbf{T}^e \right],\ \mathbf{F} = \bigcup_{e=1}^{N_{el}} \left[(\mathbf{T}^e)^T \mathbf{f}^e \right],\ \mathbf{U} = \bigcup_{e=1}^{N_{el}} \left[(\mathbf{T}^e)^T \mathbf{u}^e \right] \tag{7b}$$

where the $\bigcup$ operator represents the classical finite element assembly process, and the $\mathbf{K}$, $\mathbf{U}$, and $\mathbf{F}$ denote the global shape matrix, displacement vector, and experimental shape vector, respectively. The solution of the Eq. (7a) is suitable for the real-time monitoring process since the $\mathbf{F}$ vector is the only parameter that requires an update during each strain-data-acquisition in real-time. At the final step, the problem-specific displacement constraints can be imposed on the Eq. (7a), thus obtaining a reduced form of global equations that can be solved through an inversion/factorization process as:

$$\mathbf{K}_R\mathbf{U}_R = \mathbf{F}_R \ \Rightarrow\ \mathbf{U}_R = \mathbf{K}_R^{-1}\mathbf{F}_R \tag{8}$$

Hence, the overall deformed shape, can be reconstructed by combining the constraints conditions with the reduced displacement vector. Then total displacement, U_T, and von Mises strain and stress, ε_{vm} and σ_{vm}, can be readily calculated as:

$$U_T = \sqrt{U_X{}^2 + U_Y{}^2 + U_Z{}^2} \tag{9a}$$

$$\varepsilon_{vm} = \frac{\sqrt{2}}{3}\sqrt{(\varepsilon_1 - \varepsilon_2)^2 + (\varepsilon_2 - \varepsilon_3)^2 + (\varepsilon_1 - \varepsilon_3)^2} \tag{9b}$$

$$\sigma_{vm} = \frac{1}{\sqrt{2}}\sqrt{(\sigma_1 - \sigma_2)^2 + (\sigma_2 - \sigma_3)^2 + (\sigma_1 - \sigma_3)^2} \tag{9c}$$

where the U_X, U_Y, U_Z symbols represent the displacements along global axes, and the ε_1, ε_2, ε_3 and σ_1, σ_2, σ_3 symbols indicate the principal strains and stresses, respectively. The accuracy of the individual iFEM elements studied herein is assessed by calculating the percent difference between the reconstructed structural responses and their reference solution (i.e., obtained from high-fidelity FEM analysis) as:

$$\text{Percent Difference (\%)} = \left| \frac{\delta_{iFEM} - \delta_{FEM}}{\delta_{FEM}} \right| \times 100 \tag{10}$$

where the δ parameter can correspond to either total displacement or von Mises strain/stress.

2.3. Numerical Examples

In this study, we have solved four scrupulously selected benchmark cases that enable one to be able to reveal the advantages and disadvantageous of the three inverse-shell elements under the same sensor configurations. All the study cases provided in this paper are selected in a smart way to cover almost all types of the practical in-plane, and out-of-plane structures (i.e., plates, and shells). these cases include a tapered (wing-shape), a curved, a stiffened curved, and an imperfect(damaged) curved structure. furthermore, the boundary conditions in each case are set in a way to experience various types of deformations including stretch, bending, and torsion to be reliably considered as benchmark cases.

2.3.1. A Tapered Plate

A tapered plate with the dimensions, discretization, and sensor configurations shown in Fig. 2-3 is analyzed based on three different iFEM elements. The plate has a thickness of 10 [mm] and made of steel with the elastic modulus of 210 [GPa] and the Poisson's ratio of 0.3. The left edge of the plate is fully clamped against translational and rotational displacements and a body force of 63.765 [kN/m^3] is applied on the plate domain. As depicted in Fig. 2-3(a), the edges of the domain of interest are composed of nine subdivisions, leading to 81 quad-shaped (iQS4/iCS8) elements. For constructing the tria-shaped (iMIN3) subdomains, the 81 quadrilateral elements were divided into two triangular elements with a

single diagonal as shown in Fig. 2-3(b). Given that the plate is made of an isotropic material, and its geometry is symmetric with respect to the reference mid-plane, the strains at the top/bottom surface of the same in-plane positions will possess the same absolute values when subjected to the pure bending/torsional loads. Hence, the sensor can be located at top surface of the plate only. Here, the sensor is placed along with the edgewise iFEM elements of the domain, resulting in 32 elements being instrumented with sensors (Fig. 2-3). Since the expected deformations of the plate are bending dominated, the normal strain along the x-axis would vary significantly starting from the clamped region to the tip. Moreover, due to the tapered shape of the plate, there is an expected torsional deformation, which may cause different strain values and variations along the top and bottom edges of the plate. Furthermore, this torsional deformation also causes variations of the normal strain along the y-axis and the maximum values of such strain distribution are likely to be observed at the boundaries of the domain (i.e., clamped and tip region). As depicted in Fig. 2-3, we distribute the sensors at the boundaries along with both longitudinal and transverse coordinates of the domain. Otherwise stated, the sensor placement model conforms to the perimeter of the domain of the interest, thereby enabling one to monitor coupled bending-torsional deformations.

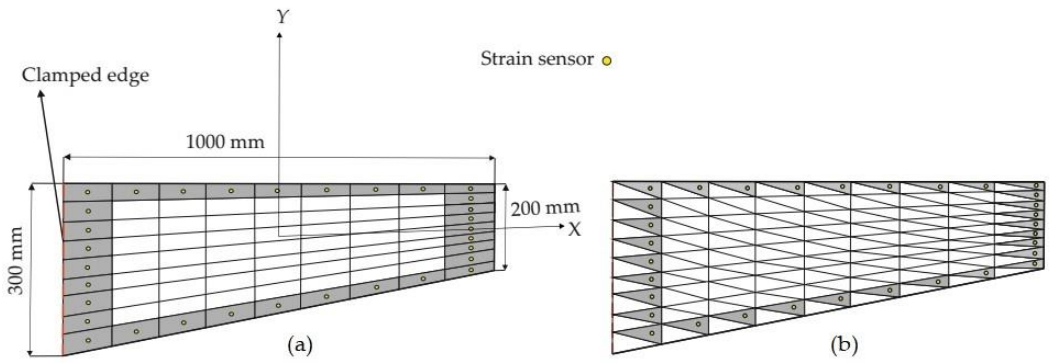

Fig. 2-3. (a) Dimensions of the tapered plate with sensor placement model on iQS4/iCS8 mesh and (b) iMIN3 mesh.

As described earlier in Eq.(5) of section 2, we need to define suitable weighting coefficients (i.e., ε and, γ) in order to preserve and guarantee the strain-interpolation continuity over the iFEM discretization. The weighting coefficient should be set to small values in case of using sensor-less elements. In order to the selection of these small constants, we pursued the following strategy. First, we defined the possible range of the small values

(i.e., 10^{-1} to 10^{-9}) for each constant. Then we computed the result of the interested field (e.g., total displacement) by setting these constants to the mentioned values until their convergence. Finally, we chose the results of the nearest values to the reference FEM analysis. considering these strategies, the weighting coefficients associated with the transverse shear sections strains were set to 10^{-3}. In addition, for the elements without any sensors, their weighting coefficients of the membrane-bending strains were assigned to 10^{-3}. In the following first, a direct FEM analysis with a fine mesh consisted of 729 elements is performed to obtain accurate displacement results that can be used as a reference solution for the iFEM analysis. Moreover, the strain values obtained from the high-fidelity FEM analyses are used to simulate the experimental in-situ strain measurements at the center of the iFEM elements. Subsequently, three different iFEM analyses are performed by using the iCS8, iQS4, and iMIN3 elements.

The iFEM results are compared in terms of displacements and stresses with respect to the direct FEM analysis as given in Figs. 2-4,2-5. Here, one can clearly observe from Fig. 2-4 that all iFEM elements generate nearly the identical displacement contours indistinguishable from those of FEM throughout the plate domain. However, the percent differences between iMIN3, iQS4, iCS8 and reference solutions for the maximum total displacements are approximately 5.42%, 0.21%, 0.53%, respectively. Therefore, the maximum displacement obtained from iQS4 and iCS8 are closer to the maximum reference displacements than the iMIN3. This observation can be attributed to two important physical/mathematical aspects: (1) the total number of sensors per total number of edgewise iFEM elements, and (2) shape function construction. As for the iMIN3 sensor placement model, fifty percent of the edgewise elements are populated with sensors while all edgewise elements in the iQS4 and iCS8 models possess one-to-one sensor placement. Referring to the shape function construction, anisoparametric shape functions of the iMIN3 element use the area-parametric coordinates of a triangle, whereas the iQS4 element's anisoparametric shape functions utilize the bilinear isoparametric mapping functions. Since the area-parametric coordinates have a less accurate interpolation capability than the Lagrangian mapping functions, the displacement approximation achieved by iQS4 and iCS8 elements is superior to that of iMIN3. Although iQS4 and iCS8 have inherently different shape functions, they perform in the same manner in terms of displacement reconstruction on a flat plate.

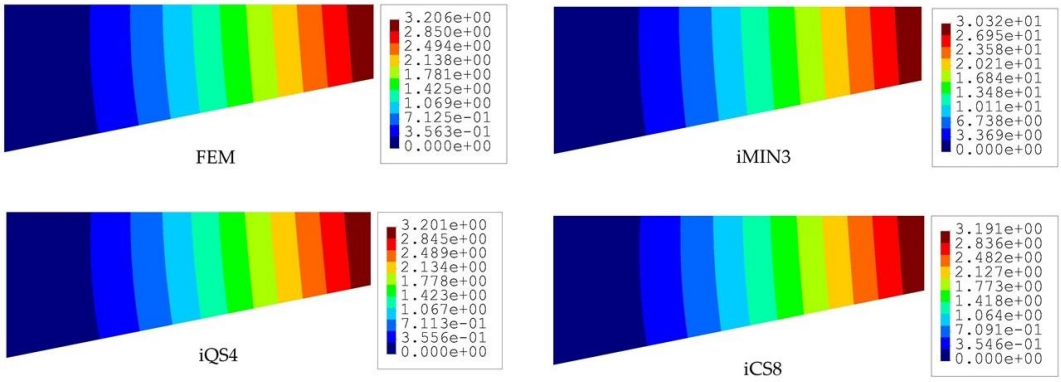

Fig. 2-4. Contours of total displacement [mm] for the tapered plate.

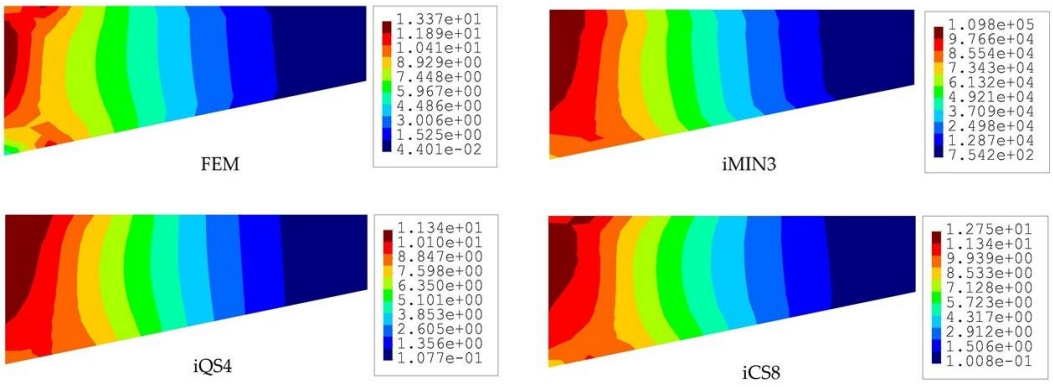

Fig. 2-5. Contours of von Mises stress [MPa] for the tapered plate.

To compare the performance of these three iFEM elements further, we perform a posteriori calculation and obtain the von Mises stress distributions across the plate domain as shown in Fig. 2-5. Although all three elements produce similar variations of stress contours along the length of the tapered plate, the iCS8 element renders a better reconstruction of the von Mises stresses in the vicinity of the clamped region as compared to the flat elements. The percent differences between reference solutions and iFEM elements (iMIN3, iQS4, and iCS8) for the maximum von Mises stress are about 17.87%, 15.33%, and 11.66% in the given order. This quantitative assessment bespeaks the higher order accuracy of the iCS8 elements for stress sensing, which is associated with the fact that strain distribution in the iCS8 element is not uniform along with spatial coordinates and possesses a high-order polynomial with respect to the flat elements. This is further supported by the non-oscillatory and smooth stress contours obtained by the iCS8 element, which is almost identical to those of FEM analysis.

2.3.2. A Curved Plate

To compare the advantages and shortcomings of the three iFEM elements for displacement reconstruction of complex geometries, we considered a simply supported cylindrical thin-shell structure (herein referred to as "curved plate"). The curved plate has a radius, length, and thickness of 100 [mm], 120 [mm], and 2 [mm], respectively. The material properties of the curved plate are the same as the previous example. As illustrated in Fig. 2-6(a), four edges of the plate are simply supported. Moreover, the top surface of the plate is subjected to a sinusoidal pressure of the form, $q(z,\theta) = q_0 \sin(\theta)\cos(\pi z / L)$, with pressure magnitude of $q_0 = 5$ [MPa], where the z and θ coordinates are bounded by $z \in [-L/2, L/2],\ \theta \in [0, \pi]$. Due to the symmetrical nature of the computational domain (i.e., geometry, material, loading, and constraints), only one-fourth of the curved plate can be prudently analyzed using appropriate symmetry boundary conditions as depicted in Fig. 6(b). To compare convergence performance of the iFEM elements in terms of the mesh/sensor density, three different mesh resolutions (i.e., 3×1, 5×2, and 15×5 elements) ranging from coarse to fine mesh/sensor densities are constructed using iMIN3, iQS4, and iCS8 elements. For the sake of clarity, examples of coarse mesh resolutions (3×1) are illustrated in Fig. 2-7. Being particular to the iMIN3 models, two different discretization schemes are proposed, namely single and cross diagonal patterns (i.e., iMIN3s and iMIN3c), as shown in Fig. 2-7. Here, tria-shape elements (i.e., offspring element) are generated by diagonally dividing the quadrilateral elements (i.e., parent element), thereby forming either two or four offspring.

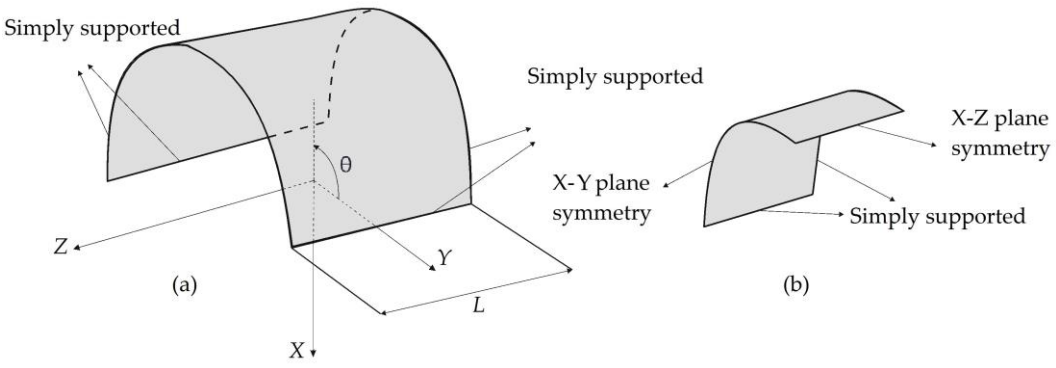

Fig. 2-6. (a) Cylindrical shell; (b) one-fourth of the shell: curved plate with symmetric boundary conditions.

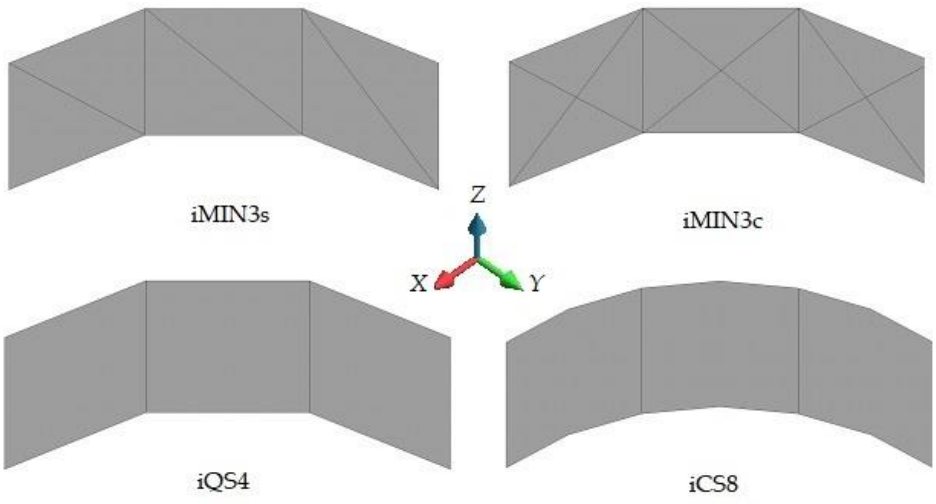

Fig. 2-7. Mesh resolution of 3×1 for the curved plate using four different discretization strategies.

To provide strain data as an input to the iFEM models as well as establish a reference solution for the curved plate, a direct FEM analysis was performed utilizing a sufficiently fine mesh composed of 105×45 quadrilateral elements with 29,256 DOF. The simulated data (i.e., representing the experimental data) is assigned to the geometric center of each relevant iFEM element. For iMIN3s and iMIN3c models, the experimental strain value at the centroid of each specific parent inverse-element (iQS4/iCS8) is equally assigned to all offspring (iMIN3) elements. In this manner, the number of sensors for each tria- or quad-mesh becomes identical such that there is no strain-less element in the triangular configurations. In this benchmark, the weighting constants associated with the membrane-bending and transverse-shear section strains are set to $w_{\varepsilon}=1$ and $w_{\gamma}=10^{-3}$ for all iFEM discretization, respectively. Afterward, the iFEM analysis for each mesh resolution of a given element type is performed and the results are presented and compared with respect to each other and reference solution in terms of contours of total displacements in Figs. 2-8, 2-9 and 2-10. One can see from Fig. 2-8 that at low mesh resolution, iCS8 element generates displacement contours much more consistent with reference contours than that produced by iMIN3s/c and iQS4 models. Additionally, for moderate mesh resolution, the better shape-sensing capability of the curved elements in terms of accurate total displacement contours has prevailed over the flat elements as shown in Fig. 2-9. Furthermore, as the mesh density increases (refer to Figs. 2-9,2-10), the

difference between the results of all elements disappears and their displacement contours become almost indistinguishable from the reference solution.

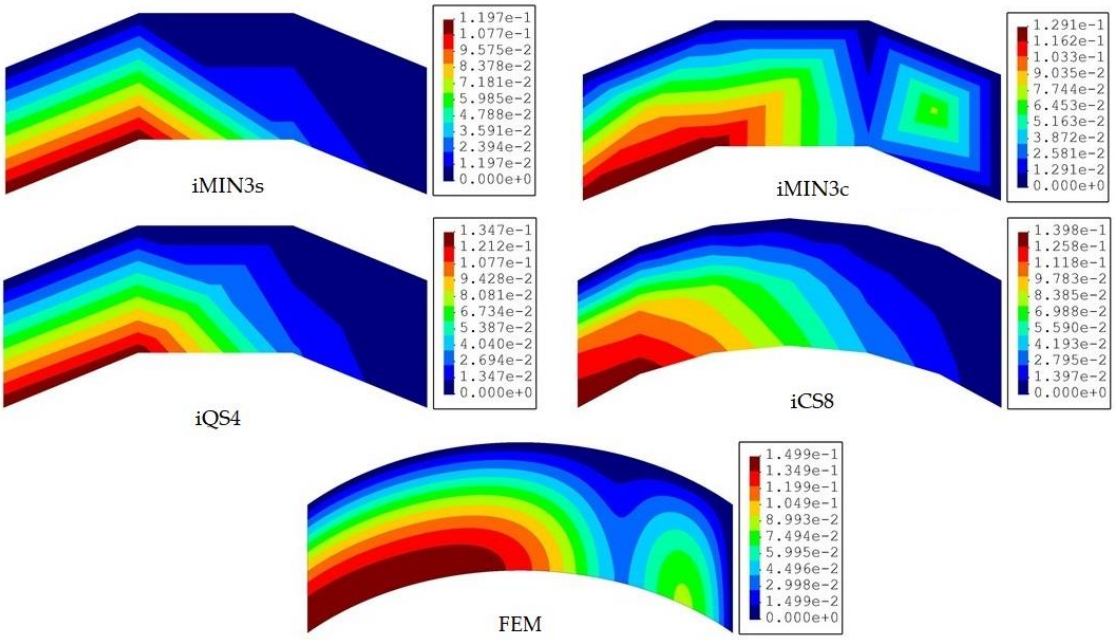

Fig. 2-8. Contours of total displacement [mm] obtained from iFEM (coarse mesh) and high-fidelity FEM analyses for the curved plate.

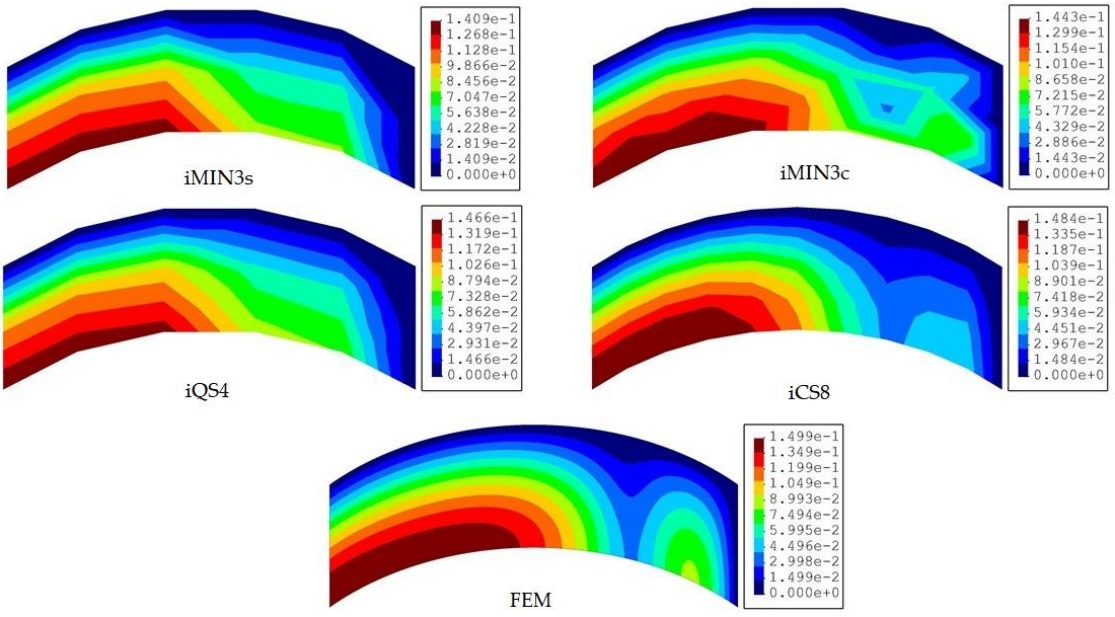

Fig. 2-9. Contours of total displacement [mm] obtained from iFEM (moderate mesh) and high-fidelity FEM analyses for the curved plate.

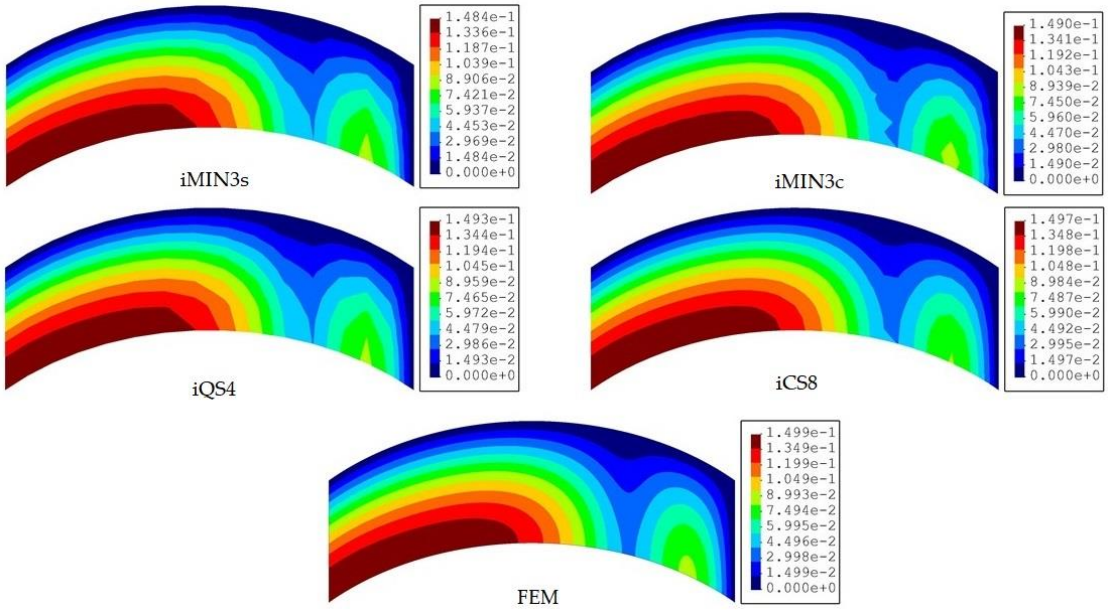

Fig. 2-10. Contours of total displacement [mm] obtained from iFEM (fine mesh) and high-fidelity FEM analyses for the curved plate.

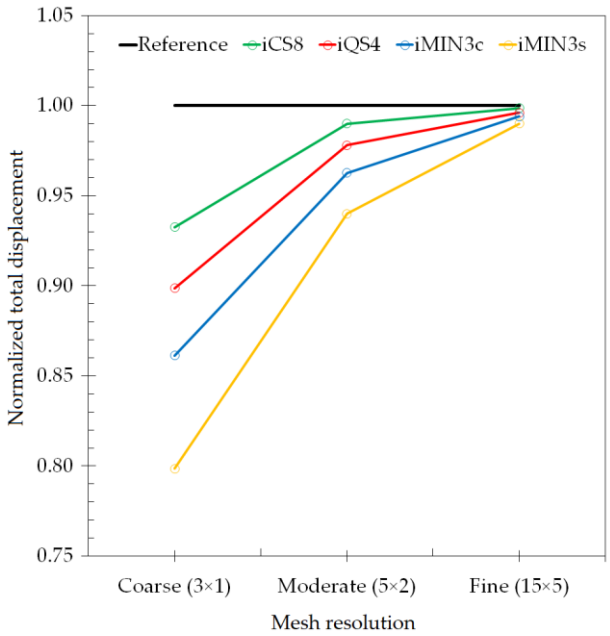

Fig. 2-11. Comparison of normalized total displacements versus increasing mesh resolution for the curved plate.

To provide a quantitative comparison for all elements, the maximum values of the total displacements of each iFEM analysis are normalized with respect to that of FEM analysis, and these results are plotted versus the increasing mesh resolution in Fig. 2-11. One can

conclude that for the modeling of a curved geometry the curved element produces the lowest displacement errors with respect to the reference solution even using the coarse discretization in the iFEM analysis. As elaborated previously, the preeminent performance of iCS8 over all the other elements is associated with the high-order (serendipity) Lagrangian shape functions and the inclusion of a greater number of nodes, which enables a better physical representation of the geometry even in the case of low mesh resolutions. It would be also interesting to compare the performance of the single- and cross-diagonal mesh models of the iMIN3 element. Accordingly, in Fig. 2-11, the iMIN3s predicts maximum normalized displacements more erroneous than the results of iMIN3c. Hence, even the same number of sensors is being used in iMIN3s/c models; the iMIN3c entails a higher precision because of the central node included in the parent quadrilateral elements, thereby enabling a better interpolation of the structural deformations in the parent domain. When the performance of the iQS4 and iMIN3c are compared in terms of displacement reconstruction, the iQS4 estimates displacements more accurately over the curved geometry, hence yielding the highest precision among the family of flat elements. Therefore, in the rest of the study, we only compare the performance of curved (iCS8) and more accurate flat elements (iQS4).

2.3.3. A Stiffened Curved Plate

Previous numerical examples have proven that the iMIN3s/c meshing strategies are not as accurate as other meshing methods using flat/curved inverse elements (namely, iCS8 and iQS4) in terms of reconstructing structural deformations. Therefore, we eliminate the comparative assessments of iMIN3 element in the remaining test cases and herein continue with the implementation of iCS8 and iQS4 on more complicated geometry, i.e., a stiffened curved plate with dimensions depicted in Fig. 2-12(a). It is expected that the strain/stress distribution should include severe and non-smooth variations due to the presence of stiffeners as well as the curvilinear geometry of the plate. Therefore, this benchmark problem lends itself to revealing the capabilities of two high- performance iFEM elements (iQS4 and iCS8) comparatively in terms of both shape and stress sensing. Specifically, the curved plate has a length, radius, and uniform thickness of 2000 [mm], 1000 [mm], and 30 [mm], respectively. The plate has equally spaced transverse stiffeners with height and thickness of 200 [mm] and 30 [mm]. The plate and stiffeners are made of an isotropic (steel) material with the elastic

modulus, Poisson's ratio, and density of 200 [GPa], 0.3, and 7800 [kg/m^3], in the given order. All edges of the plate are simply supported through allowing for rotational DOF and constraining translational DOF only. Here, the stiffened curved plate is subjected to the gravity of 9.81 [m/s^2], thus resulting in the body force of 7800×9.81 [N/m^3].

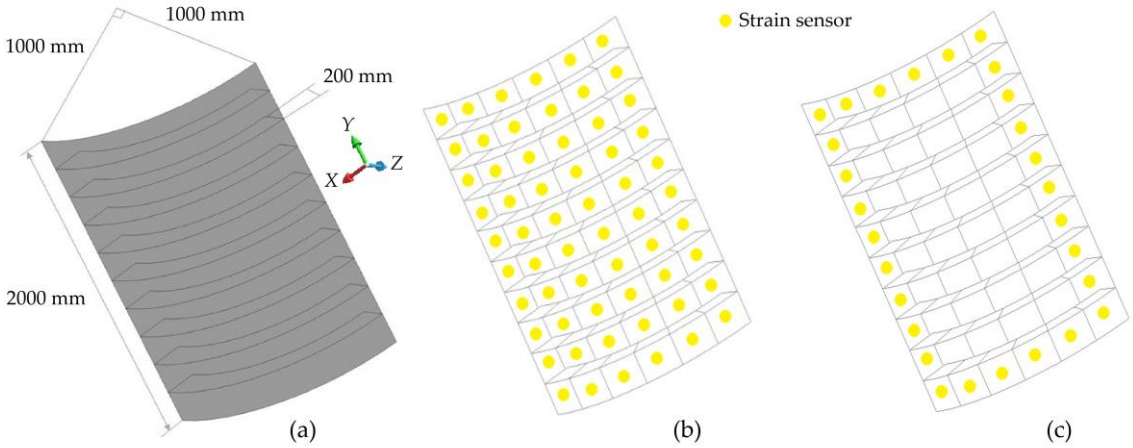

Fig. 2-12. (a) Dimensions of the stiffened curved plate; (b) sparse and (c) very sparse sensor placement models.

As in the case of previous test cases, the forward structural analysis is first performed using a high-fidelity FEM model composed of 1026 elements to generate reference solution as well as strain-sensor data, i.e., input of the iFEM analysis. The present iFEM analyses are performed using a discretization composed of uniformly distributed 114 quad-shape inverse-elements, namely as iCS8 and iQS4 element. For this test case, three types of sensor placement models, namely 'full', 'sparse', and 'very sparse' with the labels f, s, vs, are used on the same iFEM mesh resolution. In the full model, all elements include strain sensors with 114×2 total number of strain rosettes. As for the sparse sensor placement model, only inverse-elements on the surface of the plate are assigned to input strain data, thus requiring the usage of 60×2 many strain rosettes. For the last sensor configuration (vs model), the total number of strain rosettes is reduced to 28×2 many since only the inverse-elements along the edges of the curved plate are instrumented with sensors. For clarity, representative sensor-placement configurations (s and vs models) are illustrated in Fig. 2-12(b-c). All weighting constants for strain-less elements (without experimental strain data) are set to 10^{-4} while they are defined as $w_{\varepsilon}=1$ and $w_{\gamma}=10^{-4}$ for all elements with strain rosettes in the different iFEM models.

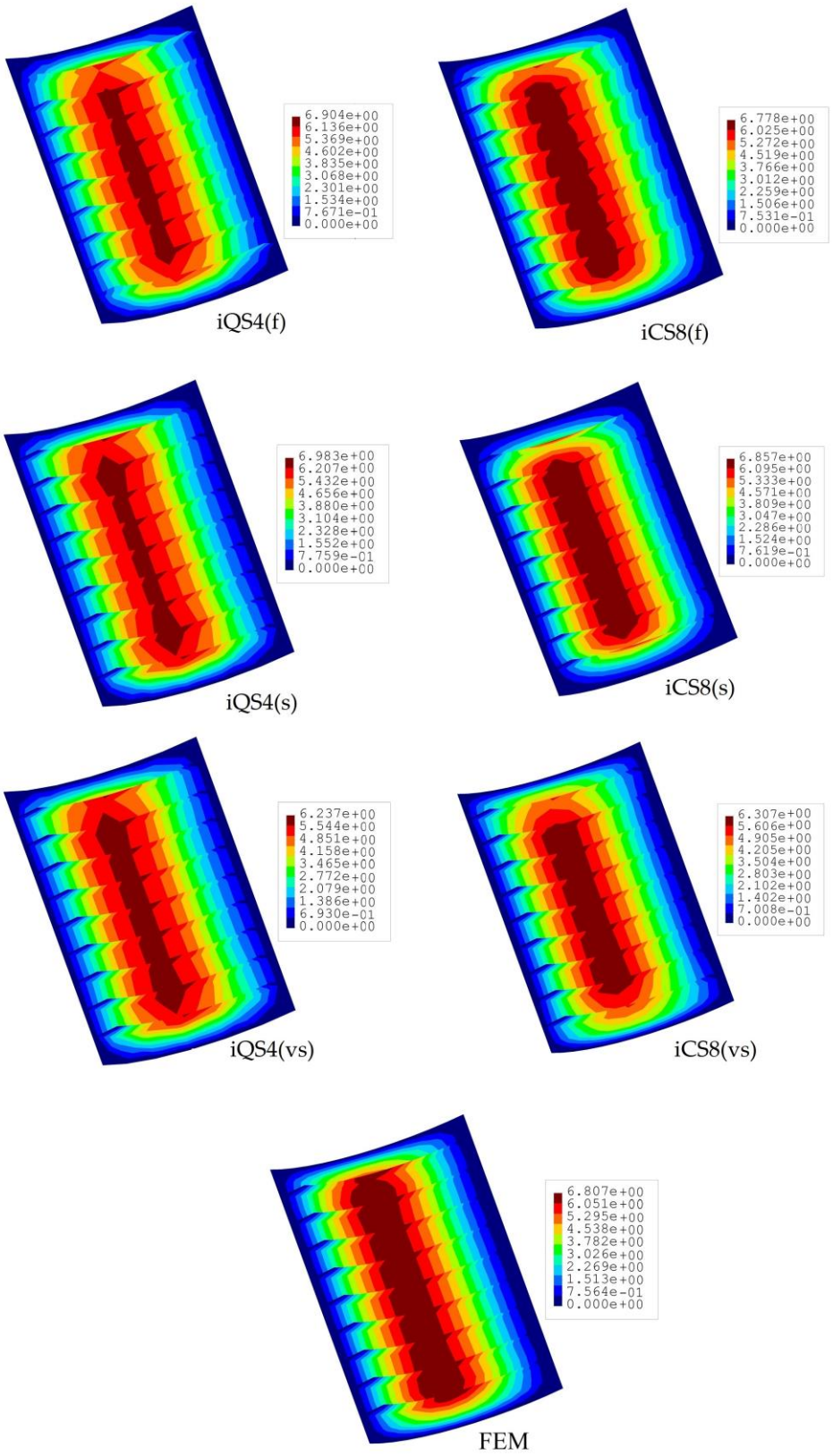

Fig. 2-13. Contours of total displacement [mm] for stiffened curve plate.

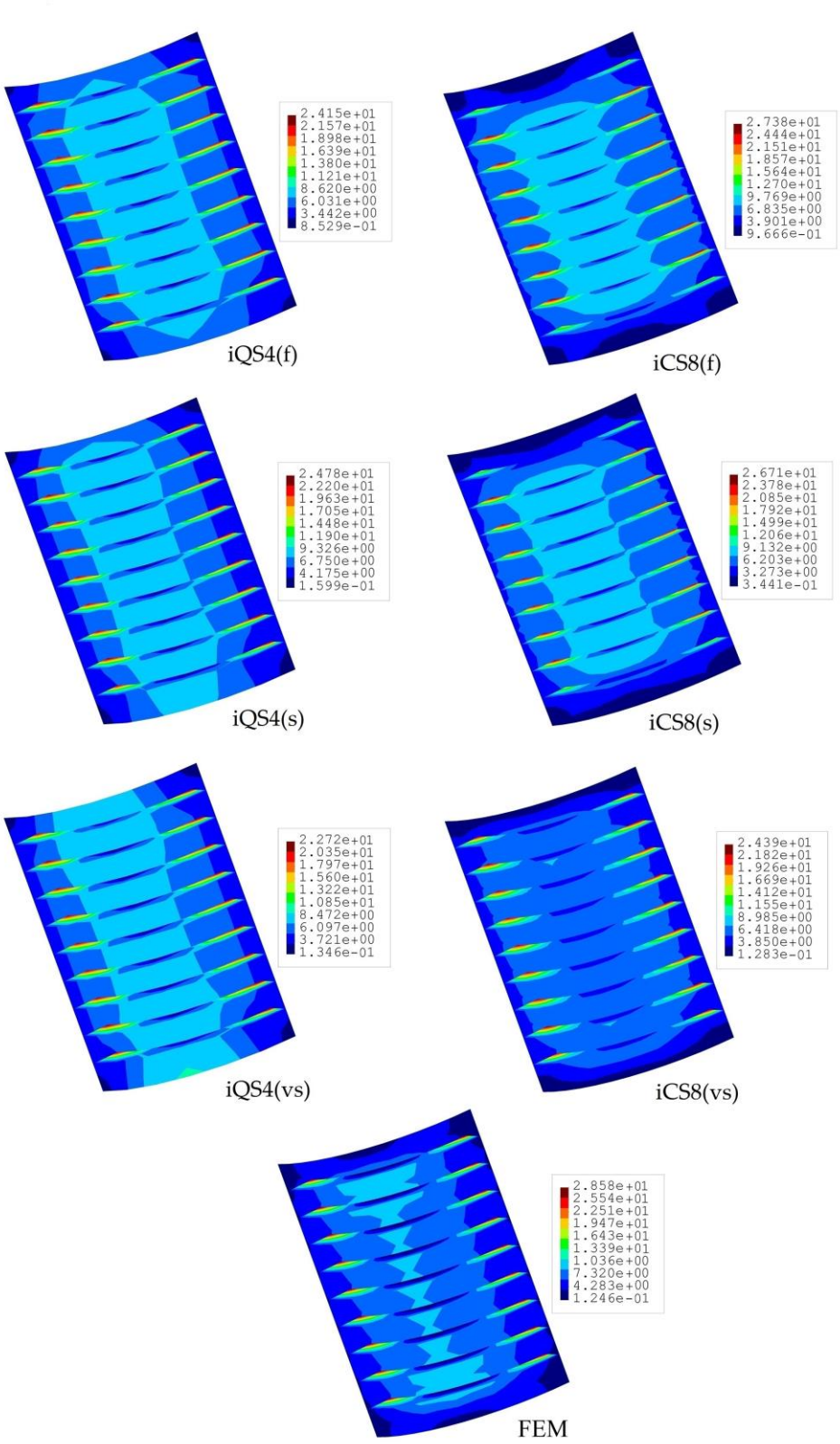

Fig. 2-14. Contours of von Mises stress [MPa] for stiffened curved plate.

In Fig. 2-13, the total displacements contours of iQS4 and iCS8 elements with different sensor density are compared with each other and with respect to the reference solution. As can be seen from the Fig., the iQS4 produces a more localized maximum total displacement field along the centerline of the plate than those of iCS8 and the reference solution for all three sensor-placement configurations. Hence, this clearly indicates that the iCS8 element reconstructs the total displacement field much better than the iQS4 element for the given curved (complex) stiffened geometry. Quantitatively speaking, the percent differences for the maximum total displacements between iFEM and FEM analyses are calculated as (1.43%, 2.59%, 8.37%) and (0.43%, 0.73%, 7.35%) for the iQS4 and iCS8 (f, s, vs) models, respectively. At higher sensor density, the iCS8 element predicts total displacement that have at least 3 times lower error than that of iQS4 element while this error reduces down to 1.15 at very sparse sensor deployment. Despite a closer error level between flat/curved elements for the vs model, it can be understood from the percent errors that as the sensor density increases, the predictive capability of the iCS8 becomes much better than the iQS4 element. Nonetheless, for any sensor density, iCS8 yields a superior shape sensing than iQS4, which can be ascribed to the conforming nature of the quad-shape curved element. A similar comparison is also provided for the von Mises stress fields as shown in Fig. 2-14. Likewise, the percent differences for von Mises stress between iFEM and FEM analyses are 13.30%, 15.50%, and 20.50%, respectively, for iQS4 models with f, s, and vs sensor deployments. Correspondingly, they are 4.20%, 6.54%, and 14.94%, for the iCS8 models. An important observation is that although there are no sensors on the stiffeners in the s and vs sensor deployments, both flat and curved elements of iFEM can predict accurate stress variations across stiffeners to an adequate degree. Overall, it is shown that the iCS8 element surpasses the predictive capability of the iQS4 not only in terms of the displacement field but also equivalent stress field.

Three previous benchmark cases were assessed again by the standard deviation measurement principle to ensure the accuracy of the obtained results. herein, not only the node with the maximum value but also all the nodes are contributed to increasing the stability of the results of different iFEM elements. The standard deviation was computed using Eq. (11) and the related results are listed in Table1.

$$\text{Standard deviation} = \sqrt{\frac{\bigcup_{i=1}^{N_n}(\delta_i^{iFEM} - \delta_i^{FEM})}{N_n}} \tag{11}$$

Where N_n represents the total number of nodes and δ parameter corresponds to either total displacement or von Mises stress.

Table 2-1. Standard deviation of U_T displacement and σ_{vm} of corresponding to iFEM models.

iFEM elements	Case1			Case2(moderate)				Case3(sparse)	
	iMin3s	iQS4	iCS8	iMin3s	iMIN3c	iQS4	iCS8	iQS4	iCS8
U_T	0.116	0.014	0.009	0.0228	0.0221	0.0220	0.0219	0.530	0.411
σ_{vm}	0.508	0.116	0.067					3.620	2.772

2.3.4. A Curved Plate with a Damaged Region

In many engineering structures, there might be internal features in the form of holes, slots, or cutouts due to the topological design or assembly requirement. These regions experience drastic strain/stress variation that needs to be closely monitored to ensure the structural integrity of the component under operational conditions. Such internal features can be modeled as a material region with degraded elastic constants or without any stiffness. Since these domains can be considered as pre-damaged locations, it will be very important and critical to accurately reconstruct the displacement and stress variation from the discrete sensor information collected at the far-field region of these pre-damaged positions. To this end, it is crucial to select effective iFEM elements for geometry-specific problems. Therefore, in this study, we have extended our benchmark cases further such that the performance of two main iFEM elements is scrutinized comparatively in terms of their predictive capabilities for full-field shape and strain sensing of pre-damaged structure. Specifically, this test case focuses on a curved plate with an eye-shaped cutout, representing either an internal feature or a pre-damaged section of a structural component. The present investigation on the curved plate can also entail the performance evaluation of curved/flat elements for their usage in damage localization and detection sensitivity.

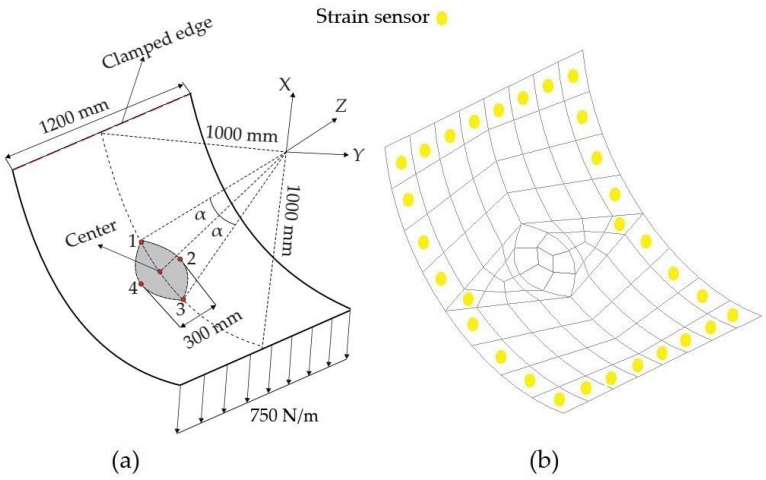

Fig. 2-15. (a) Dimensions of the curved plate with a damaged region at the center; (b) sensor placement model for iCS8/iQS4 discretization.

The dimensions of the curved plate are provided in Fig. 2-15(a), where the eye-shaped region is symmetrically located with respect to the center of the curved plate with an angle of $\alpha = \pi/16$. Two edges of this region are created by passing arcs from points of 1, 2, 3 and 1, 4, 3, in the given order. As depicted in Fig. 2-15(a), the top edge of the plate is fully clamped, namely no rotational and translation DOF, and a line-distributed force of 750 [N/m] is applied at the bottom edge of the plate. Initially the curved plate is considered to be free of any damaged, representing undamaged condition. Under the operating conditions, the plate is assumed to develop a defective eye-shaped region. Here, this region is particularly chosen to intensify the strain variation near the damaged region, thereby setting up a more challenging test case. To represent the intact and damaged (degraded) regions of the curved plate, two different elastic moduli are used, namely 210 [GPa] and 21 [MPa] for intact and defective regions, respectively, having the same Poisson's ratio of 0.3. Similar to the previous test cases, a direct FEM analysis is used for simulating experimental sensor data and establishing reference solutions for both undamaged and damaged conditions of the plate. After FEM analyses, two iFEM analyses are performed using the discrete strain data collected from the undamaged and damaged conditions of the curved plate. As shown in Fig. 2-15(b), the iFEM model is composed of 88 quad-shape elements (representing either iCS8 or iQS4) and the edgewise elements accommodate the strain sensors, thereby resulting in 30 many sensors in the model. During the iFEM analysis of the present geometry, the weighting

constants are set to the values of the previous case study (corresponding to the sparse sensor configurations, namely either s or vs model). Once the displacement is reconstructed using iCS8 and iQS4 models, the von Mises strains are calculated for each node $i = 1, 2, ..., n_{node}$ where n_{node} represents the total number of nodes available in the iFEM models. Then, for localizing the damage, the damage indication factor, Ω_i, is computed as [46-47]:

$$\Omega_i = \left| \varepsilon_i^D - \varepsilon_i^U \right| / \varepsilon_{\max}^D \tag{12}$$

where the ε_i^D and ε_i^U parameters represent the iFEM-based reconstructed von Mises strains at the nodes for the damaged and undamaged conditions of the curved plate, respectively, and the $\varepsilon_{\max}^D$ denotes the maximum value of the reconstructed von Mises strains for the damaged case. Finally, Eq. (11) is used to estimate and compare the damage detection capability of iQS4 and iCS8 elements for the present test case.

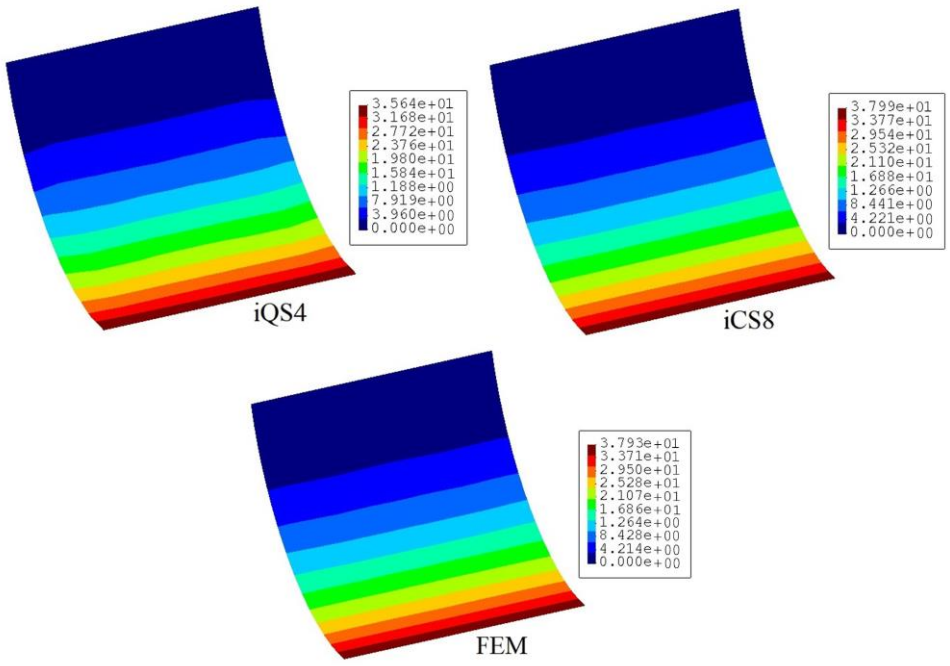

Fig. 2-16. Contours of total displacement [mm] for the damaged condition of the curve plate.

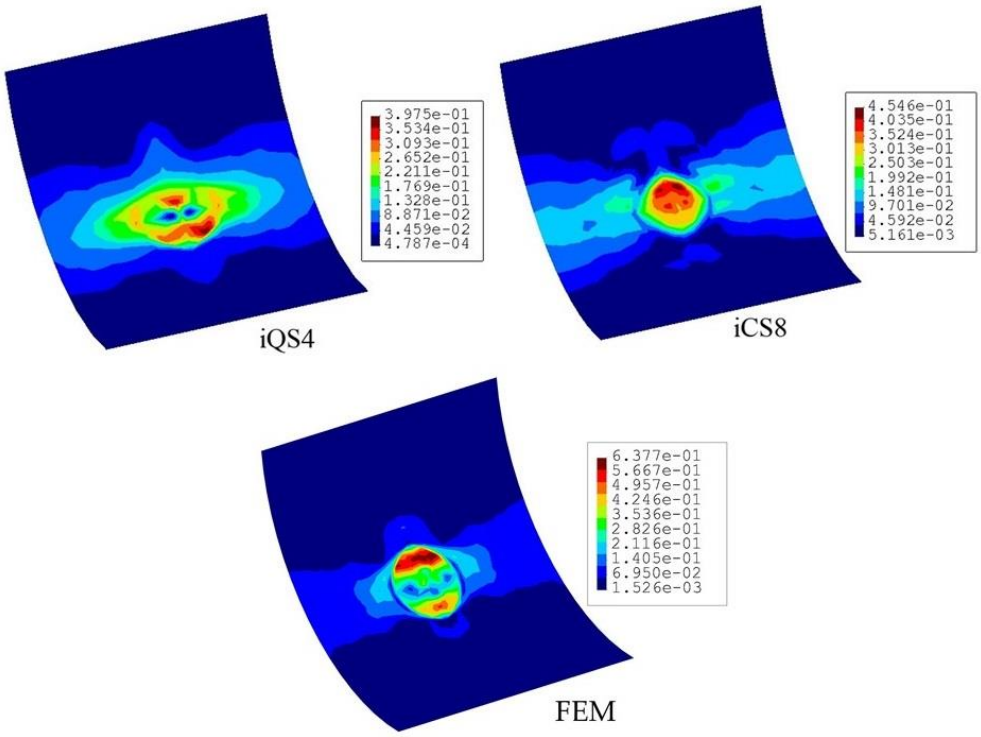

Fig. 2-17. Contours of damage indication factor for the curved plate with a damaged region.

Fig. 2-16 compares the reconstructed displacement of flat and curved elements with respect to the reference solution for the damaged configuration. As is evident from the comparison, the displacement contours do not imply the possible location of the damaged region. Nevertheless, according to maximum displacement produced by iCS8 and iQS4, the result of the curved element is in a better agreement with the reference solution than the flat element. In numbers, the percent difference between iCS8 and reference solution for the maximum displacement is 0.15% whereas it is 6.03% for the iQS4 element, thus confirming the higher precision of curved element for shape sensing of cylindrical geometry even using sparse sensor configuration. To reveal the damage localization capabilities of these elements, in Fig. 2-17 is provided the contours of damage indication factor plotted over the curved geometry using iFEM and FEM analyses. It is clearly seen from these contours that the iCS8 element localizes the damage as well as detects its eye-shape better than the flat element. Hence, it can be concluded that iCS8 element offers a better shape sensing and structural health monitoring features for real-time monitoring of complex geometries.

2.4. Conclusions

Shape-, strain-, and stress-sensing performance of iMIN3, iQS4, iCS8 elements are investigated and compared for various plate and shell structures by gradually increasing their geometrical complexity. These geometries include flat, curved, stiffened-curved, and a curved plate with a damaged region. For all iFEM elements, the weighted-least-squares functional is constructed according to the FSDT displacement kinematics. When the geometry of the structure is blade-like, as intuitively expected, there is no distinctive difference among all iFEM-reconstructed displacement results with respect to the reference solution. A slightly better stress-sensing accuracy is observed for iCS8 element over the other elements for the flat geometry. This improved in the stress prediction of iCS8 is attributed to its high-order serendipity shape functions allowing for an extra mid-node in the stress prediction. As the complexity of the geometry of the test cases increase (i.e., curved and stiffened-curved), it is proven that the predictive capability of iCS8 element becomes obviously superior to the flat elements for shape sensing with low number of sensors and coarse mesh configuration. This is because the second order isoparametric mapping functions of iCS8 allow for a smoother approximation of the curved geometries by using lower number of elements. When the flat element is compared to each, it is observed that iQS4 yields a better displacement reconstruction than that of iMIN3 meshing strategies. These meshing configurations consist of single- and cross-diagonal divisions of a quad-element into tria-elements. Remarkably, the shape-sensing ability of iMIN3 can be enhanced if the cross-diagonal meshing strategy is utilized. Finally, the damage detection feature of the elements is explored on a curved plate with a geometrically complex damage region. Accordingly, the damage detection sensitivity of the curved element is observed to much better than that of the flat element. It should be noted that this study compares iFEM elements in terms of accuracy and efficiency. However, the computational complexity is not considered. Since the iCS8 element has more nodes and consequently more DOFs compared to flat elements, the computation time is also higher. Overall, all the test cases presented herein can serve as “benchmark problems” for the newly developed iFEM shell/plate elements. In the authors' opinion, the optimization of sensor placement for shell and plate structures using iFEM can be considered as a complementary study of the current paper for future research.

CHAPTER 3. A Combined Experimental/Numerical Study on Deformation Sensing of Sandwich Structures Through Inverse Analysis of Pre-Extrapolated Strain Measurements

Real-time reconstruction of displacement field from a network of discrete strain sensors is referred to as "shape (deformation) sensing" for which inverse finite element method (iFEM) has been extensively studied and proven to be an efficient, robust, and accurate algorithm. In this study, practical shape-sensing capability of an enhanced iFEM formulation, which utilizes the kinematics of refined zigzag theory (RZT) as its baseline, is numerically and experimentally investigated for moderately thick sandwich plates/shells. To this end, a novel four-node inverse-shell element (iRZT4) is developed and implemented to discretize the governing equations of the iFEM-RZT formulation. Moreover, the iFEM-RZT approach is coupled with a polynomial-based strain pre-extrapolation technique to achieve a highly precise prediction for numerical and experimental case studies using different sensor deployment strategies. Various test cases namely stiffened plate and curved sandwich shells subjected to bending loads, and a wing-shape sandwich panel exposed to torsional loading condition are solved to evaluate the performance of the iRZT4 element. For these problems, the results of iFEM-RZT analysis with/without *'a priori*' smoothing of experimental strain data are compared with high-fidelity FEM reference solutions as well as the results of the classical iFEM formulation. In addition, through-the-thickness full-field displacement maps obtained from digital image correlation (DIC) are used to verify the iFEM and FEM results. These comparisons reveal that using a sparse sensor placement model for an iRZT4 discretization paired with the polynomial smoothing approach leads to the most precise, efficient, and reliable deformation reconstruction for moderately thick sandwich structures, among other strategies.

3.1. Introduction

Nowadays composite panels are widely used to build structural elements, e.g., aerospace components, aircraft, ship hulls, automobile bodies, and drones [60-68]. Composite materials enhance the mechanical properties (i.e., stiffness and strength) while reducing weight. Despite these advantages, composite laminates and sandwich panels are

exposed to harsh environmental conditions such as storms, winds, and wave impacts during their service life that may cause different modes of failure in these materials such as face/core debonding [69], impact damage [70], and delamination [71]. These kinds of damages can lead to catastrophic rupture of the entire structure and thereby result in economic losses, environmental issues, and human casualties. Thus, implementing a reliable, compatible, and onboard structural health monitoring (SHM) system is a necessity to prevent undesirable failure modes in engineering structures [72, 22-23]. SHM is an interdisciplinary technique that can provide a real-time estimation of physical/mechanical properties such as strain, pressure, and temperature using discrete sensors installed structure onboard. The main objective of SHM is to examine structural performance and potentially detect damage and failure conditions. Therefore, the development of an efficient and reliable SHM system that prevents those unwanted situations has become an issue of primary importance. In recent decades, numerous investigations have been performed based on the SHM systems on different kinds of materials (e.g., isotropic, and orthotropic [73, 29-30]), structural elements (e.g., beams, and shells), and various damage types of laminated composites (e.g., delamination, and indentation).

Shape sensing is the real-time reconstruction of deformations from in-situ strain measurements obtained by a network of sensors and serves as a vital complementary technology for the SHM systems. In recent years, embedded fiber optic networks e.g., Fiber Brag Grating (FBG) sensors have been extensively implemented in various engineering structures due to their high sensitivity, and measurement accuracy as well as deployment practicality (ease to embed). Therefore, FBG sensors are favorable to be used in multilayered structures for shape sensing purposes as highlighted on various review studies on the fiber optic shape sensing systems. [74-78]. Recently, different methods such as modal, analytical, and curve fitting schemes have been proposed for solving the inverse problem of shape sensing [6-13]. In addition, Tikhonov and Arsenin [1] introduced a regularization technique with a stable smoothness degree to solve this inverse problem, which has been used as the baseline of most shape sensing studies [2-5]. Moreover, various other studies have been dedicated to conducting shape sensing of beam structures experimentally with a variety of numerical algorithms [79-80]. However, these algorithms inherently lack the required accuracy and stability to be considered as a general shape sensing methodology for structures

subjected to complex loading conditions and possessing variable structural features and material properties. Apart from inverse algorithms mentioned herein, the inverse Finite Element Method (iFEM) has been lately demonstrated to be a comprehensive and robust technique that fulfills the requirements of a general shape sensing approach. The iFEM was firstly introduced by Tessler and Spangler [14,15] for real-time displacement monitoring of plate structures. This method provides various benefits listed below for diverse engineering applications:

i- Capability to assess the static or dynamic response of any structural component (beam, plate, shell, and solid) regardless of its geometrical topology and constraint boundary conditions.

ii- Utilizing only a discrete set of strain sensor data without requiring any primary knowledge of loading or material information.

iii- Possessing a general and robust mathematical formulation based on minimization of a least-squares functional that can be readily discretized and solved using C0-continuous inverse elements in real-time.

During the last decade, different types of inverse elements have been developed based on first-order shear deformation theory (FSDT) which makes iFEM applicable to real-time monitoring of beam, plate, and shell structures. FSDT based iFEM elements include a three-node inverse-shell element, namely iMIN3 [42], an efficient two-node inverse-beam/-frame element [34-81], a four-node quadrilateral inverse-shell element abbreviated as iQS4 [43], and an eight-node curved inverse shell element known as iCS8 [44]. A recent review study has been dedicated to comparing the practical shape sensing and damage detection capabilities of these inverse shell elements (i.e., iMIN3, iQS4, and iCS8) [16]. Up to now, these iFEM elements have been scrutinized both experimentally and numerically for displacement and stress monitoring of marine structures including chemical tankers [51], Panamax container ships [28], bulk carriers [52], and offshore wind turbine towers [53,54]. Furthermore, Kefal and Oterkus [82] have recently developed an isogeometric iFEM formulation for shape sensing of curved shell structures. Afterwards, various researchers also employed the isogeometric analysis coupled with iFEM for deformation reconstruction of beam-like geometries [83,84]. Additionally, the iFEM approach was used for deformed shape

estimation of thin plates undergoing large deflections [85]. Besides, three-dimensional deformations of slender composite structures were reconstructed with a highly acceptable precision using iQS4/iFEM element [56]. However, for the shape sensing of thick and moderately thick laminated structures, FSDT based iFEM formulations may have accuracy deficits due to the linearity of the kinematic relations. Therefore, these formulations may need to be enhanced for the correct prediction of through-the-thickness deformations in multilayered composites and sandwich structures.

Such a refinement was initially proposed by Cerracchio et al. [39] through utilizing iFEM together with kinematic relations of a recent single layer theory, known as refined zigzag theory (RZT) [38]. This iFEM-RZT formulation was later enhanced by Kefal et al. [40] by employing a corrected form of least-squares functional which uses the complete set of section strain in RZT including membrane, bending, zigzag, and full transverse-shear section strains. Moreover, they developed an efficient three-node inverse-shell element (i3-RZT) to solve the shape sensing problem of thick sandwich shell structures. Afterward, Kefal and Yildiz [57] utilized the i3-RZT element to numerically assess various sensor placement strategies for shape sensing and structural health monitoring of wing-shaped sandwich panels. This numerical application was later extended to experimentally verify the accuracy of the enhanced iFEM-RZT formulation [40] using a model-scale test setup of a wing-shaped sandwich structure subjected to bending loads [86], whereby the iFEM-RZT formulation was also refined for twill woven composite materials. Apart from this, a smoothed iFEM-RZT formulation was recently developed to reduce the number of sensors without losing the prediction accuracy for the deformation reconstruction [87]. In both studies of Kefal et al. [CS/MSSP], a four-node inverse-plate element (iRZT4) [88] was employed to conduct iFEM-RZT analysis based on experimental strain measurements.

To the best of the authors' knowledge, apart from the i3-RZT element, no investigation has dealt with thick sandwich shell structures using the iFEM-RZT approach. Moreover, the experimental and/or numerical studies of iFEM-RZT have not considered the reconstruction of torsional deformation in multilayered structures. Furthermore, the current state-of-the-art for iFEM-RZT does not involve polynomial smoothing techniques for 'a priori' analysis of strains to generate a continuous form of experimental strain measurements for conducting

shape sensing via a fewer number of sensors. The main and novel aim of the current study is to address these issues by extending the capabilities of the iRZT4 element to model shape sensing of thick sandwich shell structures. To this end, the membrane modeling capability of the iRZT4 element is enhanced by quadratic shape functions with an additional set of degrees of freedom (DOF) including drilling and artificial zigzag rotations. Such refinement of the iRZT4 formulation can avoid singular solutions when modeling shell geometries and thus extend the practical utility of the iFEM-RZT framework to displacement monitoring of complex/curved/built-up composite shell geometries with superior accuracy. Besides, apart from Oboe et al. [89] who have recently utilized polynomial-based strain extrapolation in the iFEM-FSDT approach only, the present study implements the polynomial strain pre-extrapolation technique to the iFEM-RZT analysis of the thick sandwich structures for the first time in literature. Furthermore, we perform an experimental torsion test on a wing-shaped sandwich panel and collect strain measurements from embedded FBGs and surface mounted strain rosettes. Then, this experimental data is rigorously processed by the iFEM-RZT approach using the iRZT4 inverse-shell element to reveal its shape sensing accuracy as compared to that of the iFEM-FSDT/iQS4 element. Overall, such novel aspects of the present effort advance the current state-of-the-art of the iFEM research.

The current investigation is structured as follows. In Section 2, the practical quadrilateral inverse-shell element, i.e., iRZT4, is mathematically formulated in detail to computationally implement the iFEM-RZT analyses for both numerical and experimental cases. In Section 3, first, three-dimensional numerical examples (a stiffened composite plate and a thick curved sandwich shell) are modeled and analyzed using iFEM-RZT and -FSDT approaches by making use of simulated strain data generated in the commercial FEM software (i.e., ANSYS APDL). Afterward, the influence of coupling the iFEM-RZT with a strain pre-extrapolating technique is evaluated and demonstrated for a different type of sparse sensor deployments. In the remainder of Section 3, for the experimental case, a tapered wing-shaped sandwich composite plate, which was previously designed and manufactured by authors [86], is analyzed by onboard and embedded strain measurement systems (i.e., strain rosettes and FBG sensors) under torsional loading boundary condition. For this purpose, various steps of the experiment, testing machine, measurement devices, and applied boundary conditions are given in detail. Then, the novel smoothing approach is conducted

using various degrees of polynomials and its continuous output strains are used in iFEM-RZT analysis with iRZT4 elements. Additionally, iFEM-FSDT and reference FEM analyses are conducted for comparison and verification, respectively and the associated results are described. Finally, in Section 4, several conclusions have been highlighted as the main advantages of utilizing improved iFEM-RZT/iRZT4 methodology coupled with polynomial smoothing approach.

3.2. Mathematical Modeling of the Shape-Sensing Problem

3.2.1. The iRZT4 Element based on iFEM-RZT Methodology

In this section, the mathematical formulation of a new RZT-based four-node quadrilateral inverse plate/shell element, so-called iRZT4, will be presented. This element was originally developed for shape sensing of laminated plate structures [88] and utilized to discretize the governing equation of the iFEM-RZT method [40]. We herein extend the capability of the iRZT4 element to displacement monitoring of shell geometries by incorporating additional degree of freedom (DOF). To present the new iRZT4 shell element formulation, a local Cartesian coordinate system (x_1, x_2, z) is placed at the center of the reference (middle) surface of the element as shown in Fig. 3-1(a), where the x_1, x_2 axes represent the in-plane coordinates, and the z axis refers to the thickness coordinate ranging from $-h$ to $+h$ (therefore total thickness is $2h$), with the $z_{(j)}$ coordinate identifying the *j*-th interface position within the laminate as depicted in Fig. 3-1(b). The iRZT4 inverse shell element has nine DOF per its each node including three u_i, v_i, w_i translational, three $\theta_{1i}, \theta_{2i}, \theta_{zi}$ rotational, and three $\psi_{1i}, \psi_{2i}, \psi_{zi}$ zigzag DOFs. The positive directions of these DOFs are aligned with the positive x_1, x_2, z axes of the element coordinate system as depicted in Fig. 3-1(a).

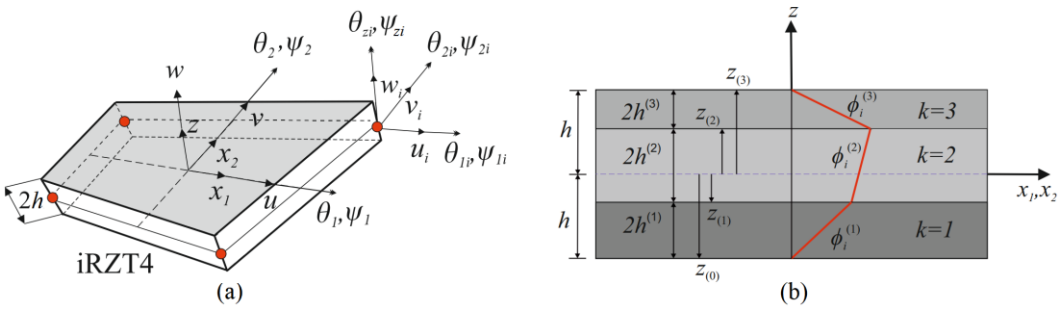

Fig. 3-1. (a) Geometry of an iRZT4 inverse shell element with associated coordinates and its nodal translational, rotational, and zigzag DOFs (b) Layer notation for a three-Layer laminate.

To solve the inverse problem of shape sensing based on the iFEM-RZT method, firstly, the in-plane displacement components, $u_1^{(k)}$ and $u_2^{(k)}$, and the out-of-plane displacement u_z at any material point within the *k*-th layer of the laminate are defined in accordance with RZT kinematic relations as [38]:

$$u_1^{(k)}(x_1,x_2,z) = u(x_1,x_2) + z\theta_2(x_1,x_2) + \phi_1^{(k)}(z)\psi_2(x_1,x_2) \tag{1a}$$

$$u_2^{(k)}(x_1,x_2,z) = v(x_1,x_2) - z\theta_1(x_1,x_2) - \phi_2^{(k)}(z)\psi_1(x_1,x_2) \tag{1b}$$

$$u_z(x_1,x_2,z) = w(x_1,x_2) \tag{1c}$$

where the u, v, w functions represent the positive translational kinematic variables along positive x_1, x_2, z axes, respectively, and the θ_1, θ_2, and ψ_1, ψ_2 functions are used to define the counter-clockwise bending and zigzag rotational kinematic variables around the positive x_1 and x_2 axes, in the given order as shown in Fig. 3-1(a). Note that these seven kinematic variables are the functions of x_1 and x_2 coordinates and independent from the thickness coordinate, z. In Eq. (1), the superscript (k) indicates the k-th lamina, and the functions $\phi_1^{(k)}$ and $\phi_2^{(k)}$ represent the through-the-thickness piecewise linear zigzag functions which can be expressed as [38]:

$$\phi_i^{(k)} = z\beta_i^{(k)} + \alpha_i^{(k)} \ (i = 1,2) \tag{2}$$

where the $\beta_1^{(k)}, \beta_2^{(k)}$ symbols represent the slopes of the zigzag functions, and $\alpha_1^{(k)}$, $\alpha_2^{(k)}$ are the lamina-level constants that satisfy the equilibrium of the zigzag functions at the interface of the adjacent layers. These terms can be defined as follows:

$$\beta_i^{(k)} = G_i / Q_{ii}^{(k)} (i = 1,2 \; ; \; k = 1,2..., N) \tag{3a}$$

$$\alpha_i^{(k)} = \beta_i^{(k)} h + \sum_{j=2}^{k} 2h^{(j-1)} G_i \left(\frac{1}{Q_{ii}^{(k)}} - \frac{1}{Q_{ii}^{(j-1)}} \right) \text{(i = 1,2)} \; , \quad G_i = \left(\frac{1}{h} \sum_{j=1}^{N} \frac{h^{(j)}}{Q_{11}^{(j)}} \right)^{-1} \text{(i = 1,2)} \tag{3b}$$

where N is the number of plies in the laminate, and the G_i and $Q_{ii}^{(k)}$ symbols denote the weighted average transverse shear stiffness of the whole laminate and the transformed transverse-shear moduli of each ply, in the given order. It is necessary to calculate element-level section strains (strain measures) both analytically and experimentally in accordance with the iFEM-RZT methodology. For the analytical calculation, isoparametric mapping of both x_1 and x_2 coordinates of the iRZT4 element can be performed by leveraging the isoparametric s and t coordinates as:

$$x_1(s,t) = \sum_{i=1}^{4} N_i \, x_{1i}, \quad x_2(s,t) = \sum_{i=1}^{4} N_i \, x_{2i} \tag{4}$$

where, the $x_{1i}, x_{2i} \; (i = 1,2,3,4)$ symbols indicate the reference (local) coordinates of the element according to (x_1, x_2, z) system and the $N_i \equiv N_i(s,t)$ functions are the bilinear isoparametric shape functions provided in Appendix explicitly. This isoparametric transformation can readily enable one to numerically integrate the iFEM-RZT equations over the surface area of an iRZT4 inverse-shell element by using the Gauss quadrature rule. In addition, the seven kinematic variables of the RZT formulation can be approximated through quadratic interpolation functions and iRZT4 element's DOF as:

$$u = \sum_{i=1}^{4} (N_i \, u_i + L_i \, \theta_{zi}) \tag{5a}$$

$$v = \sum_{i=1}^{4} (N_i \, v_i + M_i \, \theta_{zi}) \tag{5b}$$

$$w = \sum_{i=1}^{4} \left(N_i \, w_i - L_i \, (\theta_{1i} - \psi_{1i}) - M_i \, (\theta_{2i} - \psi_{2i}) \right) \tag{5c}$$

$$\chi = \sum_{i=1}^{4} N_i \, \chi_i \quad (\chi = \theta_1, \theta_2, \psi_1, \psi_2) \tag{5d}$$

where the $L_i \equiv L_i(s,t)$ and $M_i \equiv M_i(s,t)$ functions represent the second order anisoparametric shape functions [86], which are given in Appendix for mathematical completeness of the present study. Substituting Eq. (5) into Eq. (1), and then taking relevant derivatives of the resultant equation with respect to the element coordinates as stated by the linear elasticity, the in-plane and transverse-shear strains of a material point can be established as:

$$\begin{Bmatrix} \varepsilon_{11}^{(k)} \\ \varepsilon_{22}^{(k)} \\ \gamma_{12}^{(k)} \end{Bmatrix} = \begin{Bmatrix} u_{1,1}^{(k)} \\ u_{2,2}^{(k)} \\ u_{1,2}^{(k)} + u_{2,1}^{(k)} \end{Bmatrix} \equiv \mathbf{e}(\mathbf{u}^e) + z\boldsymbol{\kappa}(\mathbf{u}^e) + \boldsymbol{\mu}^{(k)}(\mathbf{u}^e, z) \tag{6a}$$

$$\begin{Bmatrix} \gamma_{1z}^{(k)} \\ \gamma_{2z}^{(k)} \end{Bmatrix} \equiv \begin{Bmatrix} u_{1,z}^{(k)} + u_{z,1} \\ u_{2,z}^{(k)} + u_{z,2} \end{Bmatrix} = \mathbf{H}_{\beta}^{(k)} \begin{Bmatrix} \boldsymbol{\gamma}(\mathbf{u}^e) \\ \boldsymbol{\eta}(\mathbf{u}^e) \end{Bmatrix} \tag{6b}$$

with the comma subscript defining derivative operator with respect to local coordinate axes, $(\cdot)_{,\alpha} = \frac{\partial(\cdot)}{\partial x_\alpha}$ $(\alpha = 1,2)$ and $(\cdot)_{,z} = \frac{\partial(\cdot)}{\partial z}$. In Eq. (6b), the $\mathbf{H}_{\beta}^{(k)}$ matrix is a transverse-shear auxiliary term given as:

$$\mathbf{H}_{\beta}^{(k)} = \begin{bmatrix} 1+\beta_1^{(k)} & 0 & -\beta_1^{(k)} & 0 \\ 0 & 1+\beta_2^{(k)} & 0 & -\beta_2^{(k)} \end{bmatrix} \tag{6c}$$

and the nodal displacement DOF of the iRZT4 element, $\mathbf{u}^e$ vector, given as:

$$\mathbf{u}^e = \begin{bmatrix} \mathbf{u}_1^e & \mathbf{u}_2^e & \mathbf{u}_3^e & \mathbf{u}_4^e \end{bmatrix}^T \tag{6d}$$

$$\mathbf{u}_i^e = \begin{bmatrix} u_i & v_i & w_i & \theta_{1i} & \theta_{2i} & \theta_{zi} & \psi_{1i} & \psi_{2i} & \psi_{zi} \end{bmatrix}^T \quad (i = 1,2,3,4) \tag{6e}$$

In Eq. (6a-b), the $\mathbf{e}(\mathbf{u}^e)$, $\boldsymbol{\kappa}(\mathbf{u}^e)$, and $\boldsymbol{\mu}^{(k)}(\mathbf{u}^e)$ vectors represent the membrane, bending, and zigzag section strains of the RZT whereas the vectors, $\boldsymbol{\gamma}(\mathbf{u}^e)$ and $\boldsymbol{\eta}(\mathbf{u}^e)$, stand for the first and second transverse-shear section strains of the RZT, respectively. These strain

measures can be scrupulously defined in terms of either derivatives of RZT kinematic variables or derivatives of the iRZT4 inverse-shell element's shape functions as:

$$\mathbf{e}(\mathbf{u}^e) = \begin{bmatrix} u_{,1} & v_{,2} & u_{,2} + v_{,1} \end{bmatrix}^T = \mathbf{B}^e \mathbf{u}^e \tag{7a}$$

$$\boldsymbol{\kappa}(\mathbf{u}^e) = \begin{bmatrix} \theta_{2,1} & -\theta_{1,2} & \theta_{2,2} - \theta_{1,1} \end{bmatrix}^T = \mathbf{B}^\kappa \mathbf{u}^e \tag{7b}$$

$$\boldsymbol{\mu}^{(k)}(\mathbf{u}^e) = \begin{bmatrix} \phi_1^{(k)}\psi_{2,1} & -\phi_2^{(k)}\psi_{1,2} & \phi_1^{(k)}\psi_{2,2} - \phi_2^{(k)}\psi_{1,1} \end{bmatrix}^T = \mathbf{H}_\phi^{(k)} \mathbf{B}^\mu \mathbf{u}^e \tag{7c}$$

$$\boldsymbol{\gamma}(\mathbf{u}^e) \equiv \begin{bmatrix} \gamma_1 & \gamma_2 \end{bmatrix}^T \equiv \begin{bmatrix} w_{,1} + \theta_2 & w_{,2} - \theta_1 \end{bmatrix}^T = \mathbf{B}^\gamma \mathbf{u}^e \tag{7d}$$

$$\boldsymbol{\eta}(\mathbf{u}^e) \equiv \begin{bmatrix} \gamma_1 - \psi_2 & \gamma_2 + \psi_1 \end{bmatrix}^T = \mathbf{B}^\eta \mathbf{u}^e \tag{7e}$$

with an auxiliary term for zigzag strains defined as:

$$\mathbf{H}_\phi^{(k)} = \begin{bmatrix} \phi_1^{(k)} & 0 & 0 & 0 \\ 0 & \phi_2^{(k)} & 0 & 0 \\ 0 & 0 & \phi_1^{(k)} & \phi_2^{(k)} \end{bmatrix} \tag{7f}$$

where the matrices $\mathbf{B}^\chi$ $(\chi = e, \kappa, \mu, \gamma, \eta)$ contain the shape functions' derivatives of the iRZT4 element and their explicit forms are provided in Appendix.

3.2.2. In Situ Section Strains

For the experimental calculation of section strains defined in Eq. (7a-e), it is necessary to collect in situ strain data from the surface structure by means of strain sensors (e.g., strain rosette and/or embedded FBG sensors). The experimental surface strain measurements obtained from these sensors can be expressed as follows:

$$\boldsymbol{\varepsilon}_i^+ = [\varepsilon_{11}^+ \quad \varepsilon_{22}^+ \quad \gamma_{12}^+]_i^T \tag{8a}$$

$$\boldsymbol{\varepsilon}_i^- = [\varepsilon_{11}^- \quad \varepsilon_{22}^- \quad \gamma_{12}^-]_i^T \tag{8b}$$

$$\boldsymbol{\varepsilon}_i^j = [\varepsilon_{11}^j \quad \varepsilon_{22}^j \quad \gamma_{12}^j]_i^T \tag{8c}$$

where the subscripts 11, 22, and 12 are utilized to describe the normal strains along the x_1 and x_2 directions, and the shear strain in the x_1x_2-plane, respectively. Moreover, the i subscript is used to represent the n number of sensor measurements collected from the $(x_1, x_2)_i$ $(i = 1, 2, 3, ..., n)$ in-plane positions at the reference surface of the iRZT4 element.

Furthermore, '+' and '−' superscripts indicate the conventional surface-mount strain gauges/rosettes on the upper (top) and lower (bottom) surfaces of laminate, respectively, whereas the '*j*' superscript represents the optic FBG sensors embedded within the *j*-th interface of the laminate as illustrated in Fig. 3-2.

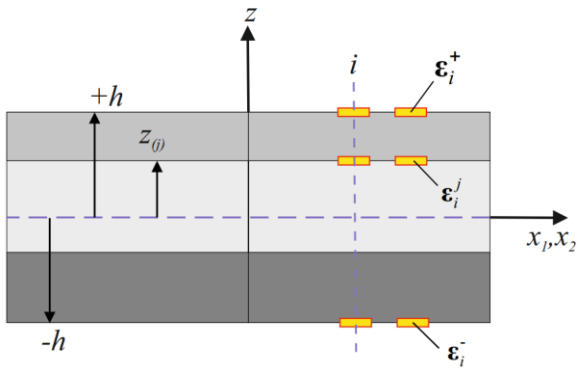

Fig. 3-2. Layout of strain sensors on the top and bottom surfaces, and at the j-th interface.

Since the zigzag functions on the upper and lower surfaces of the laminate are zero, the experimental equivalents of the membrane and bending curvature strains can be calculated explicitly according to the original plate formulation of iFEM as [15]:

$$\mathbf{E}_i = \frac{1}{2}\left(\boldsymbol{\varepsilon}_i^+ + \boldsymbol{\varepsilon}_i^-\right) \quad (i = 1,2,...,n) \tag{9a}$$

$$\mathbf{K}_i = \frac{1}{2h}\left(\boldsymbol{\varepsilon}_i^+ - \boldsymbol{\varepsilon}_i^-\right) \quad (i = 1,2,...,n) \tag{9b}$$

where $\mathbf{E}_i$ and $\mathbf{K_i}$ represent the experimental counterparts of the membrane, $\mathbf{e}(\mathbf{u}^e)$, and bending, $\boldsymbol{\kappa}(\mathbf{u}^e)$, section strains, in the given order. Also, experimental zigzag section strains can be computed using the iFEM-RZT formulation as [39,40]:

$$\mathbf{M}_i^j = \boldsymbol{\varepsilon}_i^j - \mathbf{E}_i - z_{(j)}\mathbf{K}_i \qquad (i = 1,2,...,n) \tag{10}$$

where the *j*-th interface can be selected as $1 < j < (N-1)$. For example, considering a three-ply ($N = 3$) composite structure illustrated in Fig. 2, the top and bottom strain rosettes need to be located at $z_{(0)}$ and $z_{(3)}$ coordinates, respectively. Additionally, the interlaminar coordinates of either $z_{(1)}$ or $z_{(2)}$ can be selected to embed the FBG sensors for careful calculation of the Eq. (10). Therefore, selecting only one interlaminar position of sensor

embedment is adequate to account for experimental measurement of the zigzag section strains. Unlike the membrane, bending, and zigzag section strains, the experimental counterparts (i.e., $\boldsymbol{\Gamma}_i$ and $\mathbf{H}_i$) of the transverse-shear strains cannot be extracted directly using surface strain data $(\boldsymbol{\varepsilon}_i^+, \boldsymbol{\varepsilon}_i^-, \boldsymbol{\varepsilon}_i^j)$. To account for these strain measures, one can review the recent studies of Kefal et al. [40, 88], which implements the smoothing element analysis (SEA) [90,91] to computationally obtain transverse-shear section strains from derivatives of the experimental surface strains $(\boldsymbol{\varepsilon}_i^+, \boldsymbol{\varepsilon}_i^-, \boldsymbol{\varepsilon}_i^j)$. However, when performing shape sensing for thin and moderately thick composite plates/shells (e.g., the current case study), the $\boldsymbol{\Gamma}_i$ and $\mathbf{H}_i$ contributions to the bending deformation of the laminate are negligibly small, thereby being meticulously omitted in the proceeding iFEM-RZT formulation.

3.2.3. The Weighted-Least-Squares Functional

For an individual iRZT4 element, the analytical and experimental strain measures can be placed in the iFEM-RZT least-squares-functional, $\Phi_e(\mathrm{u}^e)$, as [40, 57]:

$$\begin{aligned}\Phi_e(\mathbf{u}^e) = w_e \left\|\mathbf{e}(\mathbf{u}^e) - \mathbf{E}\right\|^2 + w_\kappa \left\|\boldsymbol{\kappa}(\mathbf{u}^e) - \mathbf{K}\right\|^2 + w_\mu \left\|\boldsymbol{\mu}^{(k)}(\mathbf{u}^e, z_{(j)}) - \mathbf{M}^j\right\|^2 \\ + w_\gamma \left\|\boldsymbol{\gamma}(\mathbf{u}^e) - \boldsymbol{\Gamma}\right\|^2 + w_\eta \left\|\boldsymbol{\eta}(\mathbf{u}^e) - \mathbf{H}\right\|^2\end{aligned} \tag{11}$$

where w_e, w_κ, w_μ refer to the weighting coefficients associated with the membrane, bending curvature, and zigzag strains in the given order. For an iRZT4 element with an attached strain sensor, these constants should be set to unity. Otherwise, to ensure the strain integrity condition over the entire domain, the associated weighting constants should be set to a relatively small value as compared to unity, such as $w_e = w_\kappa = w_\mu = 10^{-6}$. Similarly, if the experimental counterparts of first and second transverse shear strains, $\boldsymbol{\Gamma}_i$ and $\mathbf{H}_i$, are not available, then their weighting coefficients can be set to a small value as $w_\gamma = w_\eta = 10^{-6}$. More details about choosing weighting coefficient are described in [40,41]. The squared norms of Eq. (11) can be shown in normalized Euclidean norms as:

$$\left\|\mathbf{e}(\mathbf{u}^e)-\mathbf{E}\right\|^2=\iint_{A^e}\left(\mathbf{e}(\mathbf{u}^e)-\mathbf{E}\right)^2 dx_1dx_2 \tag{12a}$$

$$\left\|\boldsymbol{\kappa}(\mathbf{u}^e)-\mathbf{K}\right\|=4h^2\iint_{A^e}\left(\boldsymbol{\kappa}(\mathbf{u}^e)-\mathbf{K}\right)^2 dx_1dx_2 \tag{12b}$$

$$\left\|\boldsymbol{\mu}^{(k)}(\mathbf{u}^e,z_{(j)})-\mathbf{M}^j\right\|^2=\iint_{A^e}\left(\boldsymbol{\mu}^{(k)}(\mathbf{u}^e,z_{(j)})-\mathbf{M}^j\right)^2 dx_1dx_2 \tag{12c}$$

$$\left\|\boldsymbol{\gamma}(\mathbf{u}^e)-\boldsymbol{\Gamma}\right\|^2=\iint_{A^e}\left(\boldsymbol{\gamma}(\mathbf{u}^e)-\boldsymbol{\Gamma}\right)^2 dx_1dx_2 \tag{12d}$$

$$\left\|\boldsymbol{\eta}(\mathbf{u}^e)-\mathbf{H}\right\|^2=\iint_{A^e}\left(\boldsymbol{\eta}(\mathbf{u}^e)-\mathbf{H}\right)^2 dx_1dx_2 \tag{12e}$$

where the A^e symbol indicates the area of an individual iRZT4 element. The formulation in Eqs. (12a-e) are valid when only one sensor is present at the centroid of the iRZT4 inverse element. In the case of multiple sensors, their contribution which comes from the other points rather than the centroid of the element should be taken into consideration by imposing appropriate weighting constants [44,56]. Minimizing the $\Phi_e(\mathbf{u}^e)$ functional with respect to the unknown $\mathbf{u}^e$ nodal displacement leads to the following equation:

$$\frac{\partial\Phi_e(\mathbf{u}^e)}{\partial\mathbf{u}^e}=\mathbf{k}^e\mathbf{u}^e-\mathbf{f}^e=0\ \Rightarrow\ \mathbf{k}^e\mathbf{u}^e=\mathbf{f}^e \tag{13}$$

where the $\mathbf{f}^e$ is the local shape vector, which is a function of experimental strain data, while the $\mathbf{k}^e$ is the local shape matrix which is calculated analytically based on iRZT4 element. The enhanced iFEM-RZT equations obtained herein can be given as [62]:

$$\mathbf{k}^e=\iint_{A^e}\left(\begin{array}{l} w_e\mathbf{B}^{\mathbf{e}T}\mathbf{B}^{\mathbf{e}}+w_\kappa 4h^2\mathbf{B}^{\boldsymbol{\kappa}T}\mathbf{B}^{\boldsymbol{\kappa}}+\cdots \\ \qquad\cdots w_\mu\mathbf{B}^{\boldsymbol{\mu}T}(\mathbf{H}_\phi^{(k)}(z_{(j)}))^T\mathbf{H}_\phi^{(k)}(z_{(j)})\mathbf{B}^{\boldsymbol{\mu}}+w_\gamma\mathbf{B}^{\boldsymbol{\gamma}T}\mathbf{B}^{\boldsymbol{\gamma}}+w_\eta\mathbf{B}^{\boldsymbol{\eta}T}\mathbf{B}^{\boldsymbol{\eta}} \end{array}\right)dx_1dx_2 \tag{14a}$$

$$\mathbf{f}^e=\iint_{A^e}\left(\begin{array}{l} w_e\mathbf{B}^{\mathbf{e}T}\mathbf{E}+w_\kappa 4h^2\mathbf{B}^{\boldsymbol{\kappa}T}\mathbf{K}+\cdots \\ \qquad\cdots w_\mu\mathbf{B}^{\boldsymbol{\mu}T}(\mathbf{H}_\phi^{(k)}(z_{(j)}))^T\mathbf{M}^j+w_\gamma\mathbf{B}^{\boldsymbol{\gamma}T}\boldsymbol{\Gamma}+w_\eta\mathbf{B}^{\boldsymbol{\eta}T}\mathbf{H} \end{array}\right)dx_1dx_2 \tag{14b}$$

Herein, the integrals of the left-hand-side-matrix $\mathbf{k}^{\mathbf{e}}$ and the right-hand-side-vector $\mathbf{f}^e$ can be calculated numerically by the Gaussian integration method. After calculating the $\mathbf{k}^e$ matrix using Eq. (14a) for an iRZT4 element, one artificial stiffness constant must be placed in the diagonal positions of the $\mathbf{k}^e$ matrix corresponding to each artificial zigzag degree of freedom. In this way, spurious modes or singular solutions resulting from the inclusion of the

artificial degree of freedom can be easily avoided. These constants can be chosen and placed at diagonal positions corresponding to the degree of freedom $\psi_{zi}(i=1,2,3,4)$ for each node in the matrix $\mathbf{k}^e$ as follows:

$$\mathbf{k}^e_{(j)(j)} = \lambda \times \min(\mathbf{k}^e_{(j-1)(j-1)}, \mathbf{k}^e_{(j-2)(j-2)}) \quad (j=9i;\ i=1,2,3,4) \tag{15}$$

where λ represents a small value (e.g., $\lambda = 10^{-5}$) and the first and second indices inside the parentheses of the $\mathbf{k}^e_{(j)(j)}, \mathbf{k}^e_{(j-1)(j-1)}, \mathbf{k}^e_{(j-2)(j-2)}$ terms represent the row and column positions of the elements belonging to the $\mathbf{k}^e$ matrix. Moreover, a suitable transformation matrix, $\mathbf{T}^e$, must be used to transform the mentioned local matrix and vector given in Eq. (13) to the global coordinate system. Afterward, the global equations associated with each inverse element are assembled to constitute a general shape matrix, $\mathbf{K}$, shape vector, $\mathbf{F}$, and displacement vector, $\mathbf{U}$ as follows:

$$\mathbf{K}\mathbf{U} = \mathbf{F} \tag{16a}$$

$$\mathbf{K} = \bigcup_{e=1}^{N_{el}} \left[\mathbf{T}^{eT} \mathbf{k}^e \mathbf{T}^e \right],\ \mathbf{F} = \bigcup_{e=1}^{N_{el}} \left[\mathbf{T}^{eT} \mathbf{f}^e \right],\ \mathbf{U} = \bigcup_{e=1}^{N_{el}} \left[\mathbf{T}^{eT} \mathbf{u}^e \right] \tag{16b}$$

$$\mathbf{T}^e = \begin{bmatrix} \mathbf{T} & \mathbf{0} & \cdots & \mathbf{0} \\ \mathbf{0} & \mathbf{T} & \mathbf{0} & \mathbf{0} \\ \vdots & \mathbf{0} & \ddots & \vdots \\ \mathbf{0} & \mathbf{0} & \cdots & \mathbf{T} \end{bmatrix},\ \mathbf{T} = \begin{bmatrix} \mathbf{l}^T & \mathbf{p}^T & \mathbf{n}^T \end{bmatrix}^T \tag{16c}$$

where the $\bigcup$ symbol shows the finite element assembly process for N_{el} number of discrete inverse element and $\mathbf{l}$, $\mathbf{p}$, $\mathbf{n}$ vectors are defined as unit vectors of the x_1, x_2, z axes according to the global coordinate system, respectively. As the final step, geometric and constraint boundary conditions are imposed into Eq. (16a) leading to a reduced form of global equations. The reduced displacement vector, $\mathbf{U}_R$, can be calculated via an inversion procedure as:

$$\mathbf{K}_R \mathbf{U}_R = \mathbf{F}_R \ \Rightarrow\ \mathbf{U}_R = \mathbf{K}_R^{-1} \mathbf{F}_R \tag{17}$$

where the $\mathbf{K}_R$ and $\mathbf{F}_R$ terms correspond to the reduced forms of the global shape matrix and vectors used in Eq. (16a). Afterwards, to establish an equivalent structural state, total displacement of the iRZT4 shell mid-surface can be computed as:

$$U_{\mathrm{T}} = \sqrt{u^{2} + v^{2} + w^{2}} \tag{18}$$

In the present study, to investigate the accuracy and efficiency of the iFEM results, the percent difference between the reconstructed structural responses (i.e., total displacement) and reference solution is calculated as:

$$\text{Percent Difference (\%)} = \left| \frac{U_{\mathrm{T}}^{\mathrm{iFEM}} - U_{\mathrm{T}}^{ref}}{U_{\mathrm{T}}^{ref}} \right| \times 100 \tag{19}$$

where the $U_{\mathrm{T}}^{\mathrm{iFEM}}$ and U_{T}^{ref} symbols indicate the total displacements predicted by iFEM formulation and its reference analysis such as high-fidelity FEM analysis and/or experimental measurement techniques (e.g., digital image correlation analysis).

3.2.4. The Strain Pre-extrapolation technique

In the current study, all the results obtained from iFEM-RZT analyses for numerical and experimental cases are re-evaluated using the strain pre-extrapolation technique. To this end, the so-called polynomial smoothing approach is employed by constructing a curve (mathematical function) that has the best fit to a series of strain data points along a selected sensor line. Coupling polynomial smoothing technique with iFEM-RZT enables usage of fewer strain sensors for an accurate shape-sensing process, thereby leading to a low-cost approach. To implement the proposed methodology for numerical case studies, only half of the discrete strain measurement points are utilized by using different types of sensor placement strategies. For the experimental example, number of sensors is kept constant while a high-resolution iFEM mesh is utilized to generate extra elements in the whole domain. Afterward, multinomial curves are fit through the available discrete experimental strain measurement points in order to substitute the missing strain values with virtual strain data.

The least squares method is used for fitting polynomials through discretely obtained strain data. The general form of a polynomial with k^{th} order takes the form:

$$y = a_k x^k + \cdots + a_1 x + a_0 \tag{20}$$

Where a represents polynomial coefficient, and the term k shows the degree of the polynomial. The method of least squares minimizes the difference between the estimated values of the polynomial and the expected values from the dataset. The coefficient of the

polynomial regression model is determined by solving the following system of linear equations.

$$\begin{bmatrix} N & \sum_{i=1}^{N} x_i & \cdots & \sum_{i=1}^{N} x_i^k \\ \sum_{i=1}^{N} x_i & \sum_{i=1}^{N} x_i^2 & \cdots & \sum_{i=1}^{N} x_i^{k+1} \\ \vdots & \vdots & \vdots & \vdots \\ \sum_{i=1}^{N} x_i^k & \sum_{i=1}^{N} x_i^{k+1} & \cdots & \sum_{i=1}^{N} x_i^{2k} \end{bmatrix} \begin{bmatrix} a_0 \\ a_1 \\ \vdots \\ a_k \end{bmatrix} = \begin{bmatrix} \sum_{i=1}^{N} y_i \\ \sum_{i=1}^{N} x_i y_i \\ \vdots \\ \sum_{i=1}^{N} x_i^k y_i \end{bmatrix} \tag{21}$$

where N refers to the number of points to be regressed. This system of equations is derived from the polynomial residual function, and it is presented in the standard form of $Ma = b$. Cramer's rule allows one to solve the linear system of equations to find the regression coefficients using the determinants of the square matrix M. Each of the coefficients a_k can be determined using the following equation:

$$a_k = \frac{\det(M_i)}{\det(M)} \tag{22}$$

where M_i is the matrix with the i^{th} column replaced with the column vector b. For instance, M_0 could be calculated as follows:

$$M_0 = \begin{bmatrix} \sum_{i=1}^{N} y_i & \sum_{i=1}^{N} x_i & \cdots & \sum_{i=1}^{N} x_i^k \\ \sum_{i=1}^{N} x_i y_i & \sum_{i=1}^{N} x_i^2 & \cdots & \sum_{i=1}^{N} x_i^{k+1} \\ \vdots & \vdots & \vdots & \vdots \\ \sum_{i=1}^{N} x_i^k y_i & \sum_{i=1}^{N} x_i^{k+1} & \cdots & \sum_{i=1}^{N} x_i^{2k} \end{bmatrix} \tag{23}$$

The authors perform the Cramer's rule to solve the aforementioned linear system of equations, and thereby find the best curve fit through the discrete strain measurements.

3.3. Numerical and Experimental Examples

As mentioned in previous section, the main aim of this study is to investigate the new inverse shell element's (i.e., iRZT4) capability for shape sensing three-dimensional moderately thick sandwich structures. This new iFEM-RZT inverse element is developed based on a robust quadrilateral iFEM inverse element so called iQS4. The authors recently have investigated a comparative study between existing inverse elements including a three-

node (iMIN3) , a four-node (iQS4) , and eight-node (iCS8) inverse shell elements in terms of their efficiency and accuracy for the shape-sensing of various geometries [16]. The obtained results and observations of previous study shows the superior performance of the quadrilateral inverse shell elements (iQS4 and iCS8) as compared to the three-node inverse element (iMIN3) for tapered plate and curved geometries. It is shown that better performance of four- and eight-node inverse shell elements is attributed to shape function construction approach. Anisoparametric shape functions of the iMIN3 inverse element use the area-parametric coordinates of a triangle, while the iQS4 and iCS8 inverse shell elements use anisoparametric shape functions with bilinear isoparametric mapping technique. Since the area-parametric coordinates have a less accurate interpolation capability than the Lagrangian mapping functions, the displacement approximation achieved by quadrilateral elements is superior to that of the three-node inverse element. Since the best existing RZT-based three-node inverse element i.e., i3-RZT [40] is developed based on iMIN3 element, enhanced shape sensing performance of iRZT4 against i3-RZT is deemed. However, to show the superiority of four-node versus three-node inverse shell elements, the comparison between iRZT4 and i3-RZT elements is performed over a laminated stiffened plate. As an extra justification, the shape estimating capability of iFEM-iRZT4 element is compared to that of iFEM-iQS4 element for a curved laminated sandwich structure. Finally, for the purpose of experimental validation, a wing-shaped sandwich laminate with embedded discrete FBG sensors and surface mounted strain rosettes is designed, manufactured, and tested under torsional deformation.

The acquired strain data are used as input in iFEM-RZT and -FSDT formulation for shape sensing of the structure. Additionally, a high-fidelity FEM model is generated to establish a reference solution for assessing the accuracy of iFEM reconstructed displacements. Finally, a polynomial extrapolation strategy is employed to smooth the discrete and sparse in-situ strain data for improving the accuracy of the iFEM results and optimizing the sparse sensor deployment with a fewer number of sensors.

3.3.1 Longitudinally and Transversely Stiffened Sandwich Plate: Numerical Case Study I

Shape sensing application of a stiffened laminate is assessed to show the ability of the iRZT4 shell element to be used for three-dimensional built-up composite structures. As shown in Fig. 3-3(a) the laminate has a length of 3000 [mm], a width of 1000 [mm], and six stiffeners with a height of 150 [mm]. Support elements have the same constant thickness of 25 [mm] whereas the plate has a uniform thickness of 50 [mm]. The stiffened plate is a sandwich laminate made of unidirectional carbon fiber reinforced polymer matrix (CFRP) face sheets and PVC soft-core materials. The span to thickness ratio of the plate is equal to 60 which categorizes this sandwich laminate among moderately thick composites.

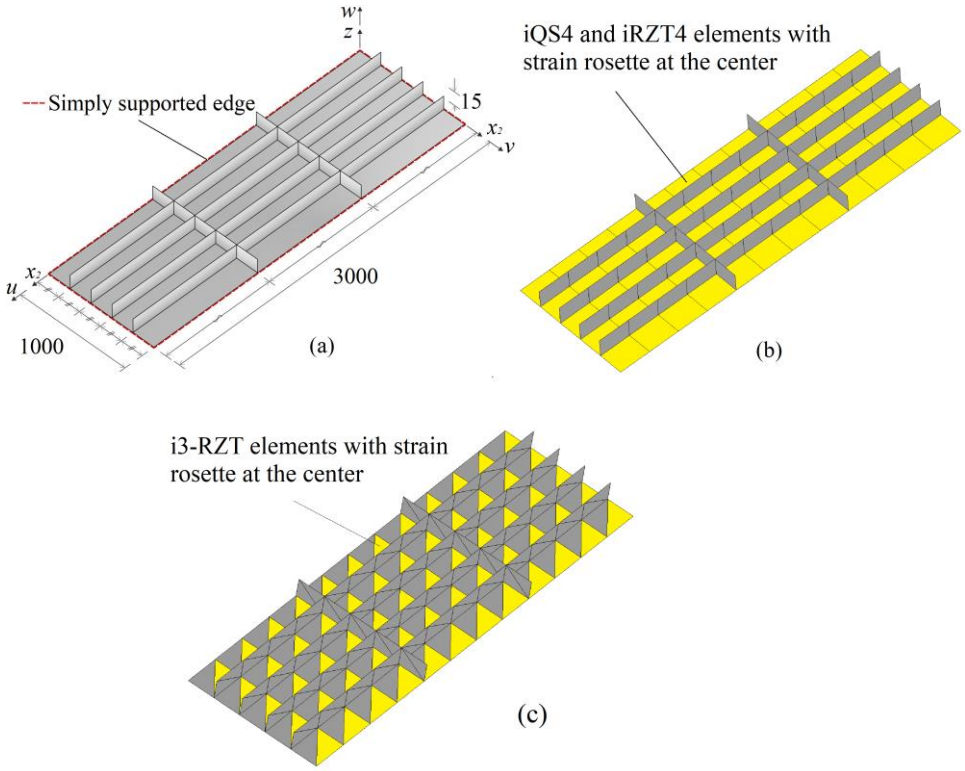

Fig. 3-3. a) Dimensions [mm] and boundary condition of the stiffened shell laminate; b) Mesh resolution and sensor placement for iFEM-iRZT4 and -iQS4 elements c) Mesh resolution and sensor placement for iFEM-i3-RZT elements

The mechanical properties of both CFRP face sheets and the PVC core materials are listed in Table 3-1. CFRP face sheets have normalized lamina thicknesses ($h^{(k)}/h$) of 0.2 whereas this value for the PVC core material is 0.6. The laminate stacking sequence is listed in Table 3-2. This multilayered structure is subjected to a constant pressure of 63.5 [KPa] along negative z direction and the edges of the laminate are simply supported as illustrated

in Fig. 3-3(a). The kinematic boundary conditions for the laminate in the $z=0$ plane is defined as follows:

$$\begin{aligned} &v = w = \theta_1 = \psi_1 = 0 \quad (x = 0, x = 3 \text{ [m]}), \\ &u = w = \theta_2 = \psi_2 = 0 \quad (y = 0, y = 1 \text{ [m]}) \end{aligned} \tag{20}$$

A FEM analysis is performed to create the reference solution and to provide required sensor data to be used in the iFEM-RZT formulation. Fig. 3-3(b), illustrates in-plane locations of onboard strain sensors. For the iFEM-RZT and -FSDT analyses, a low-resolution mesh is created using 118 inverse elements as depicted in Fig. 3-3(b).

The weighting coefficients of the membrane, bending curvature, and zigzag strains for the iRZT4 inverse shell elements, possessing sensors are set to unity. However, for sensor-less elements these constants are set to a small value (i.e., 10^{-6}). Moreover, weighting coefficients corresponding to transverse shear strains are chosen as $w_\gamma = 10^{-9}$, and $w_\eta = 10^{-3}$ for iFEM-RZT and $w_\gamma = 10^{-6}$ for iFEM-FSDT analyses. These weighting coefficients ensure the necessary strain interpolation connectivity among inverse elements with sensors.

Table 3-1. Mechanical properties of the orthotropic and isotropic materials

Lamina material		Young's modulus [GPa]	Poisson's ratio	Shear modulus[GPa]
C	Carbon-epoxy unidirectional composite	$E_1^{(k)} = 157.9$	$\upsilon_{12}^{(k)} = \upsilon_{13}^{(k)} = 0.32$	$G_{12}^{(k)} = G_{13}^{(k)} = 5.93$
		$E_2^{(k)} = E_3^{(k)} = 9.584$	$\upsilon_{23}^{(k)} = 0.49$	$G_{23}^{(k)} = 3.227$
P	PVC core	$E^{(k)} = 0.104$	$\upsilon^{(k)} = 0.3$	$G^{(k)} = 0.04$

In Fig. 3-4, the total displacement results of iFEM-RZT analyses using i3-RZT, and iRZT4 inverse shell elements, and iFEM-FSDT analysis by iQS4 inverse shell element on the geometry of the laminate are compared with the reference FEM solution result. As shown in Fig. 3-4, there are approximately 6% and 20% differences for the maximum values of the total displacement between the reference (FEM) result and those obtained using the iFEM-iRZT4 and -i3-RZT models, respectively. However, when comparing the FEM result with iFEM-FSDT the percent deference increases drastically to almost 85%. These margins of errors indicate an acceptable level for iFEM-RZT analyses versus iFEM-FSDT analysis. Moreover, the superior applicability and high precision of four-node iFEM-RZT element,

iRZT4 as compared to three-node inverse shell element i3-RZT for shape estimating of three-dimensional composite shell structures is observed. The more robust result of iRZT4 inverse element is also emphasize the previous study accomplished by authors [16]. In addition, as is seen in Fig. 3-4, the comparison of the displacement contours obtained from direct and inverse analyses demonstrates that the final deformed shape of the structure can be almost identically reconstructed by the iFEM-RZT approach. On the contrary, the iFEM-FSDT analysis underestimates the maximum displacements albeit having similar displacement contours to the reference solution. Hence, these results prove the superior full-field shape sensing capability of the iRZT4 element over iQS4 for three-dimensional moderately thick shell structures.

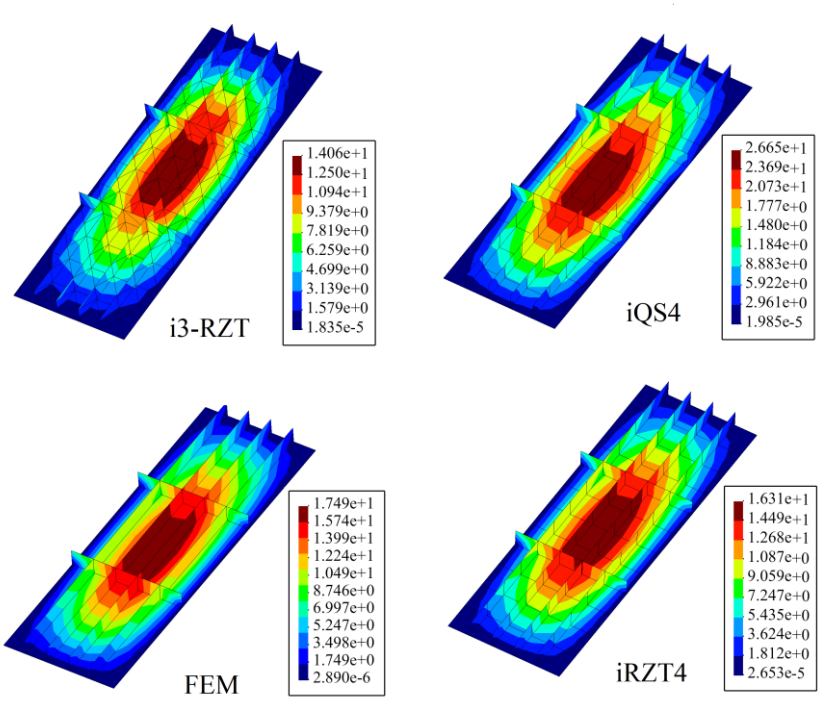

Fig. 3-4. Contour plots of total displacements [mm] of the stiffened sandwich laminate using FEM, iFEM-RZT, and -FSDT analyses.

Table 3-2. Laminate stacking sequences

Laminate	Normalized lamina thickness, $h^{(k)}/h$	Lamina materials	Lamina orientation [°]
Uniaxial Sandwich	0.2/0.6/0.2	C/P/C	0/0/0

One of the main aims of this study is to couple the iFEM-RZT approach and a polynomial smoothing technique to decrease the required number of strain measurements and attain much more precise results using the same number of sensors. Therefore, this numerical example is reevaluated using four different sparse sensor placement models as shown in Fig. 3-5. The first sensor model has an asymmetrical distribution with respect to the x_2 axis, while the other three sensor models (types II, III and IV) are symmetrically arranged. For the first model, the sensors are accommodated on six parallel rows along the x_2 axis with each row having five sensors. The other six rows are considered one in between without sensors. On the other hand, for second sensor placement, the strain rosettes and FBGs are installed in a checkered form. For third arrangement, there are six parallel rows of five sensors in a lateral direction wherein two rows are at the edges and the remaining sensors are paired at two sides of the lateral stiffeners. Finally, for the fourth case, sensor modeling consisted of three parallel pairs with ten sensors for each segment such that two lateral rows between sensors lines are left without sensors as clearly illustrated in Fig. 3-5. To numerically predict the missing in-situ strain values (for gray inverse elements), an extrapolation technique is employed through fitting five-degree polynomial curves between in-situ strain values of the inverse elements with discrete sensors (yellow inverse elements) aligned along x_1 axis. The weighting constants of the membrane, bending, and zigzag section strains corresponding to the elements on the plate are set to unity. However, for the elements on the stiffeners (i.e., without sensors) these constants are defined as a very small value (i.e.,10^{-6}). Additionally, the weighting coefficients of the transverse shear strains are set to $w_\gamma = 10^{-7}$, $w_\eta = 10^{-3}$ during iFEM-RZT analyses.

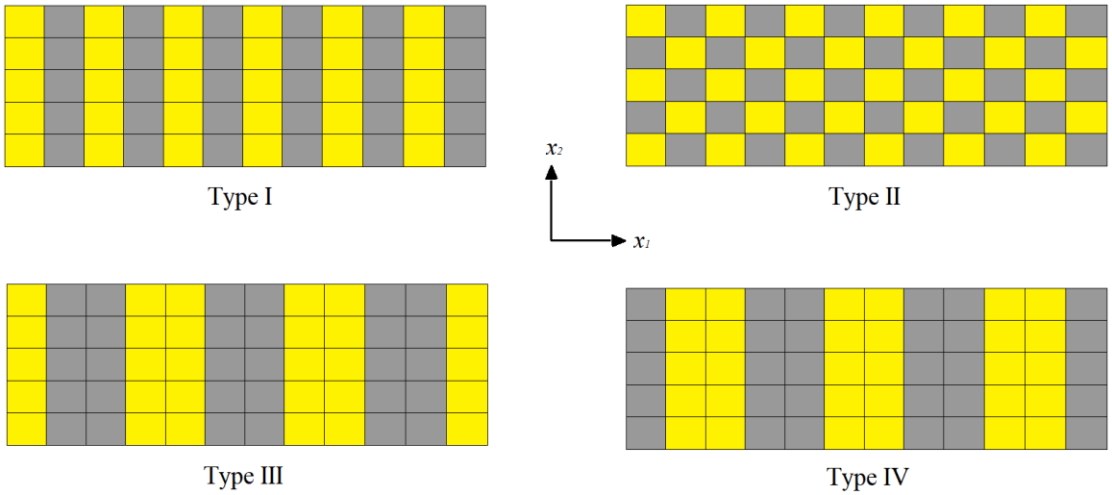

Fig. 3-5. Different types of sensors layouts.

As illustrated in Fig. 3-6, despite decreasing the number of the sensors to half of the previous test case iFEM-RZT analyses can still reconstruct precise enough full-field displacement contours in all four configurations of the sensor deployments studied herein. Furthermore, the comparison of the quantitative results reveals that in the first and third types of sensor placement strategies, the error percentage between iFEM-RZT and FEM analyses has increased to almost 15% while it remains at the same rate of 6% for the second sensor layout. This superior performance of the second layout as compared to the others (i.e., first and third sensor placement types) can be attributed to its checkered sensor distribution which enforces the iRZT4 model to fulfill the existing strain gap between the sensor lines in an accurate manner. Among these four types of sensor placements, the best performance belongs to the fourth type with only a 3% difference with the FEM reference solution. Since the central part of the structure experiences a significant amount of the strains under current constraint boundary conditions, the presence of one-third of all sensors at that segment makes this sensor model very efficient for the prediction of full-field displacement. As another important finding, the obtained results imply that by using a polynomial smoothing approach for iFEM-RZT no discrete strain values are needed to be collected from the locations adjacent to the stiffeners.

Additionally, as depicted in Fig. 3-7, the variation of the transverse displacement through the entire length of the structure is investigated to provide a more concrete comparison between the performance of the four types of sensor arrangements. The iFEM-

RZT analysis using the fourth sensor placement produces a highly accurate distribution of deflection which is almost indistinguishable from the reference solution result as seen in Fig. 3-7. Likewise, the deformation profile predicted by the second sensor placement model is similar to that of the FEM reference solution with a minor discrepancy at the middle of the structure. On contrary, the first and third types of sensor deployment have the least similarity to the FEM reference solution among all sensor layouts. It is noteworthy that the asymmetric placement of sensor type I is reflected in the variation line of the transverse displacement, as shown in Fig. 3-7. One can observe from the obtained results that using the extrapolation technique enables iFEM-RZT to predict the missing sensors' contribution over the whole structure domain in an efficient manner. Overall, as the main outcome of this numerical assessment, it can be stated that the iFEM-RZT method combined with the strain pre-extrapolation approach by using an appropriate sensor layout can provide reliable and cost-effective results.

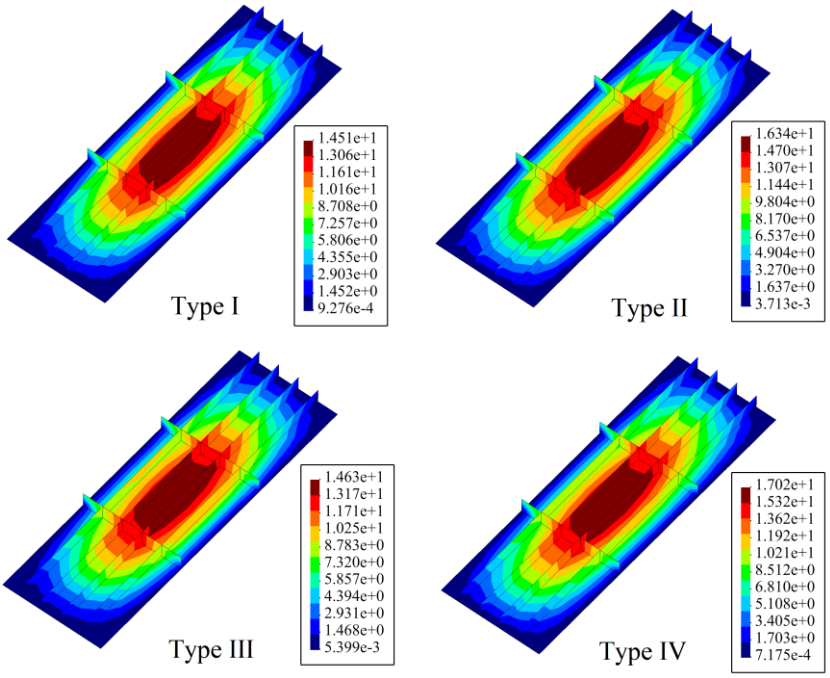

Fig. 3-6. Contour plots of total displacements [mm] of the stiffened sandwich laminate using iFEM-RZT method coupled with polynomial smoothing approach.

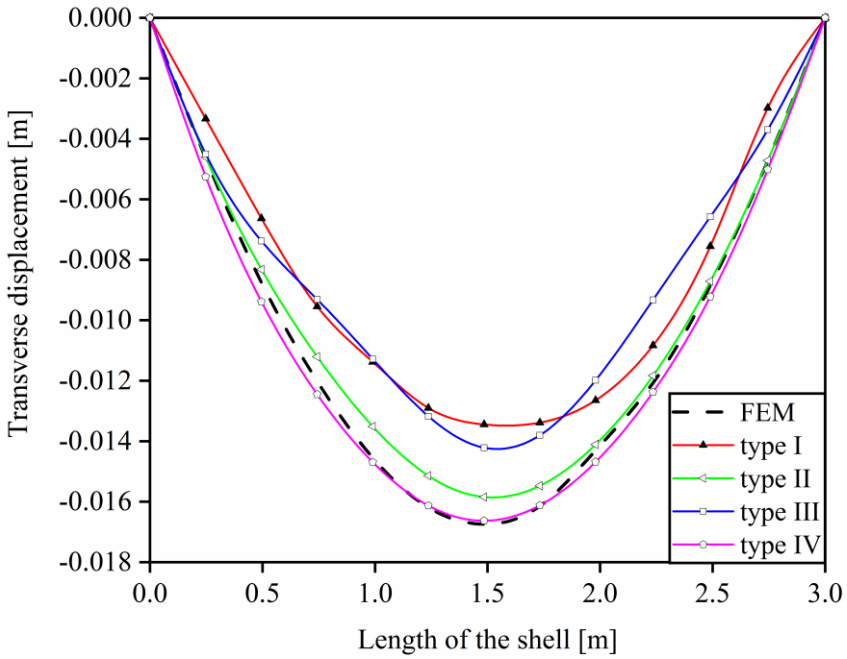

Fig. 3-7. Transverse displacement U_z (x,0.4,0.0) variation through the length of the shell.

3.3.2 A Curved Sandwich Shell Structure: Numerical Case Study II

A curved sandwich shell structure is evaluated using iFEM-RZT as the second numerical case study. The geometry of this curved shell is made by a quarter of a cylinder with a radius of 500 [mm], a width of 600 [mm], and a uniform thickness of 20 [mm] as depicted in Fig. 3-8(a). The radius to thickness ratio is 25 which classifies this sandwich laminate as a moderately thick composite structure. The same constitutive materials provided in Table 3-1 for the previous numerical case study are also used for this curved sandwich shell structure. The laminate stacking sequence for this numerical example is listed in Table 3-3. Since the curved composite panels are commonly used in aircraft which experience high gravitational accelerations due to altitude variations, they are designed to be stiff enough under subjected gravitational accelerations. To simulate such a condition in the current numerical case, the curved shell laminate is subjected to the gravity of 10g (98.1 [m/s2]) along negative and in-plane directions. Additionally, all the edges of the curved panel are fully clamped. Similar to the previous example, a high-fidelity FEM analysis (with a uniform mesh composed of 6400 quadrilateral shell elements) is performed to provide required strain data and a comparative reference solution for the iFEM analyses. On the other hand, the shape sensing of this curved geometry is carried out using a coarse mesh resolution (8×8

iFEM elements) illustrated in Fig. 3-8(b) where the top/bottom sensor measurements are collected from each inverse element. Since strain data is available for all inverse elements, in the current numerical case, the weighting constants associated with the membrane, bending, and zigzag section strains are set to unity. However, the weighting coefficients of transverse shear strains are chosen as $w_\gamma = 10^{-3}$ and $w_\eta = 10^{-5}$ for iFEM-RZT, and $w_\gamma = 10^{-3}$ for iFEM-FSDT.

Table 3-3. Laminate stacking sequences

Laminate	Normalized lamina thickness, $h^{(k)}/h$	Lamina materials	Lamina orientation [°]
Cross-ply Sandwich	$(0.5)_4/1.6/(0.5)_4$	$(C)_4/P/(C)_4$	$(0/90)_4/0/(90/0)_4$

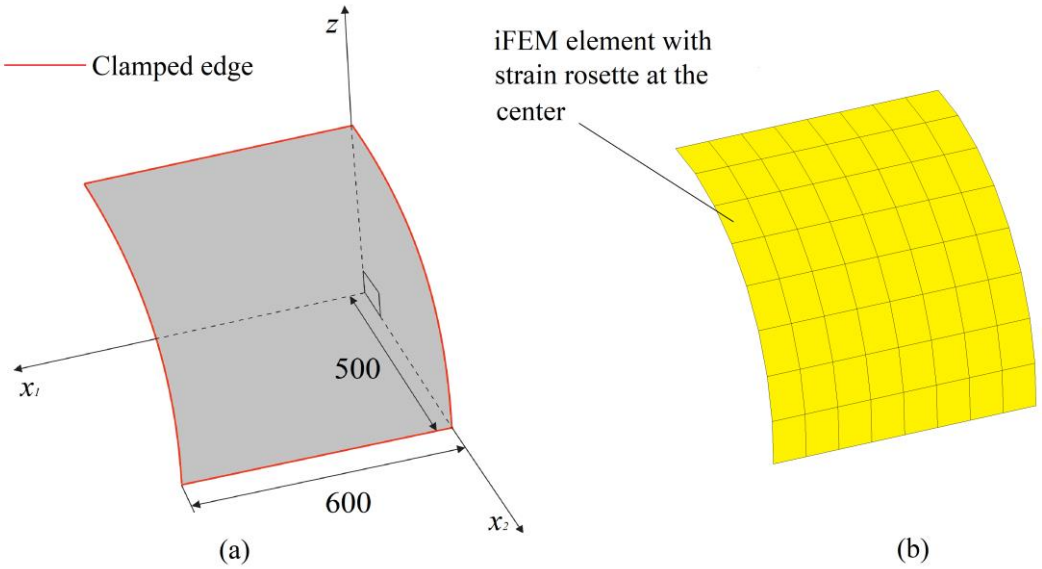

Fig. 3-8. a) Dimensions [mm] and boundary condition of the curved shell laminate; b) Mesh resolution for iFEM model with strain measurement sets at the center of the elements.

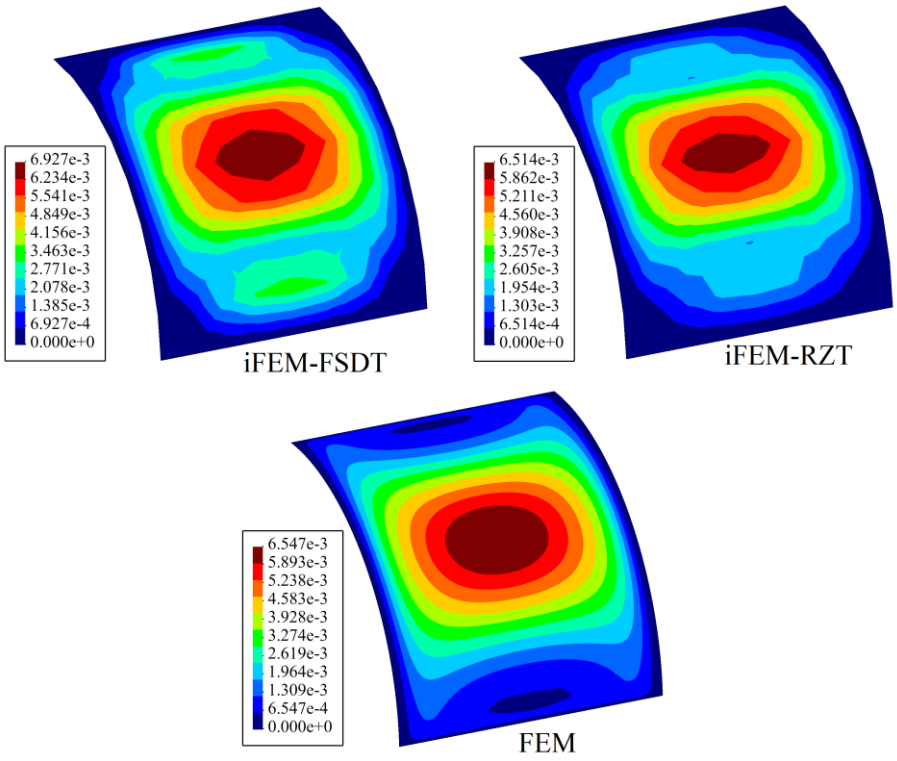

Fig. 3-9. Contour plots of total displacements [mm] of the curved sandwich laminate using FEM, iFEM-RZT, and -FSDT analyses.

As depicted in Fig. 3-9, the total displacement contours obtained from iFEM, and FEM analyses prove superior performance of iRZT4 as compared to the iQS4 inverse element. Comparison of the quantitative results shows almost 0.5% difference between the maximum amount of the total displacement for reference FEM solution and iFEM-RZT while this error percentage increases up to 6% between FEM and iFEM-FSDT analyses. Furthermore, obtained contours demonstrate a better predictive capability of iFEM-RZT in comparison to iFEM-FSDT. To sum up, both analyzed numerical examples namely stiffened and curved moderately thick laminated structures show a high level of efficiency and accuracy of iFEM-RZT as compared to iFEM-FSDT. The findings of these numerical case studies demonstrate practical applicability and high efficiency of the iRZT4 inverse-shell element for shape sensing of thick and moderately thick composite structures.

Herein, a polynomial smoothing approach is also implemented to optimized sensor locations for increasing the accuracy of the shape sensing results of the reduced sensor model. Since the displacement contours for the current case study are similar to those of the previous stiffened plate case, i.e., maximum strain distribution in the middle of the structure, we

choose a sensor deployment strategy similar to type IV as illustrate in Fig. 3-10(b). According to this configuration, only half of the elements are accommodated with sensors, depicted as yellow elements in Fig. 3-10(b). To this end, three-degree polynomial curves are fit through the discrete sensor positions along the z axis, and the weighting coefficients of the transverse shear strains are set to $w_\gamma = 10^{-3}$ and $w_\eta = 10^{-8}$.

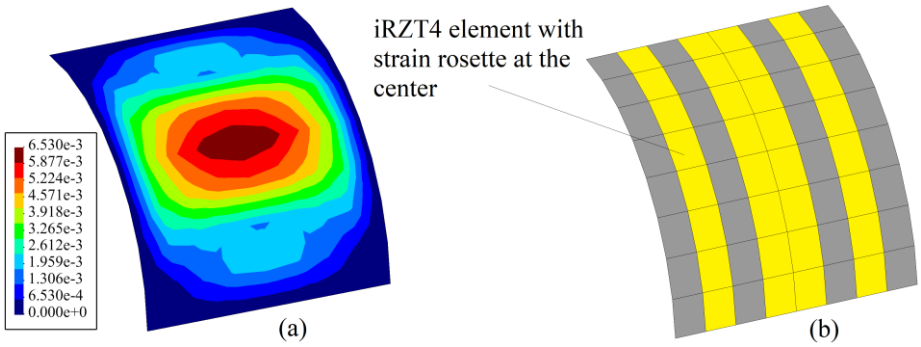

Fig. 3-10. a) Contour plots of total displacement [mm] of the curved sandwich laminate using iFEM-RZT method coupled with polynomial smoothing approach; b) Sensor layout used for polynomial smoothing.

Although the number of sensors is reduced to half in the case of smoothing analyses, the displacement contours are identical to that of iFEM-RZT with complete sensor deployment shown in Fig. 3-10(a). Moreover, the deference between direct and inverse analyses has decreased to 0.3%. These results indicate that a successful low-cost shape sensing in loaded composite structures can be obtained via utilization of a strain pre-extrapolation technique, optimum sensor deployment and selection of appropriate weighting constants.

3.3.3 A Wing-Shaped Sandwich Panel: Experimental Case Study

A wing-shaped plate with a length of 1000 [mm], left and right widths of 175 [mm] and 75 [mm] respectively, and a uniform thickness of 26 [mm] is manufactured as depicted in Fig. 3-11. Details of the manufacturing procedure and optimizing sensor arrangement can be found in [86]. The length to the thickness ratio of the plate is $\rho = 1000/26 = 38.5$. The sandwich structure is made of a TWILL T300 type carbon fiber woven fabric as a face sheet material, and a CORECELL M60 foam as soft-core material having orthotropic and isotropic material features, respectively. The left black area with a length of 100 [mm] is fully clamped

against translational and rotational deformations as well as the bottom right corner of the plate is restrained for translational deformations along z axis only as shown in Fig. 3-11. Furthermore, the top right corner of the laminate is subjected to a normal concentrated force of F_z = -620 [N] (along z axis) to yield a torsional deformation within the sandwich laminate. The exact in-plane positions of the sensors with respect to the origin indicated in Fig. 3-11 are listed in Table 3-4. The x_1, x_2 and z axes are referred to as 'length', 'width', and 'thickness' coordinates, in the given order.

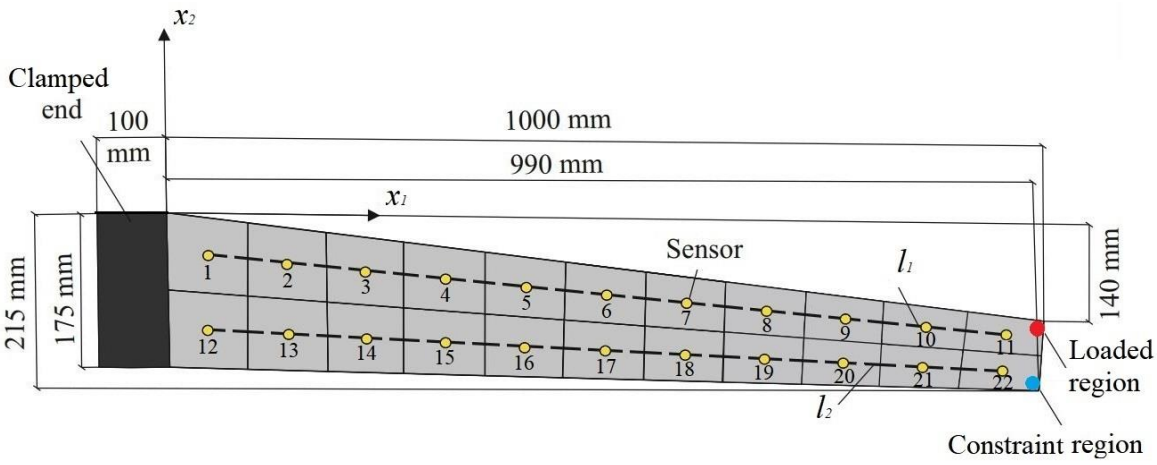

Fig. 3-11. Dimensions, boundary conditions, and sensor positions of the wing-shaped laminate

Table 3-4. Coordinates of sensors on wing shaped structure.

Sensor	x_1 [mm]	x_2 [mm]	Sensor	x_1 [mm]	x_2 [mm]
1	45	-49	12	45	-134
2	136	-59	13	135	-140
3	227	-70	14	226	-146
4	317	-80	15	316	-152
5	408	-91	16	406	-158
6	499	-101	17	496	-164
7	589	-112	18	586	-170
8	680	-122	19	677	-176
9	771	-133	20	767	-181
10	861	-143	21	857	-187
11	952	-154	22	947	-193

The mechanical properties of both carbon-epoxy twill-woven composite and M60 core materials are provided in Table 3-5 and the relevant details can be found in [86]. The thickness, laminate layup, and orientation of each lamina are specified in Table 3-6 as well.

Table 3-5. Mechanical properties of the orthotropic and isotropic materials

Lamina material		Young's modulus [GPa]	Poisson's ratio	Shear modulus[GPa]
CT	Carbon-epoxy twill woven composite	$E_1^{(k)} = E_2^{(k)} = 53.8085$	$\upsilon_{12}^{(k)} = 0.03285$	$G_{12}^{(k)} = 3.012$
		$E_3^{(k)} = 16.0$	$\upsilon_{13}^{(k)} = \upsilon_{23}^{(k)} = 0.2$	$G_{13}^{(k)} = G_{23}^{(k)} = 1.255$
M	Corecell M60 core	$E^{(k)} = 0.044$	$\upsilon^{(k)} = 0.1$	$G^{(k)} = 0.02$

As listed in Table 3-6, the twill-woven carbon face sheets have identical thicknesses of 6 [mm], whereas the thickness of the core material is 14 [mm]. Since the plate geometry is symmetrical with respect to the reference mid-plane, the applied loading condition does not produce any membrane strains and subsequently, top/bottom strain measurements are expected to be identical in absolute values. Hence, as illustrated in Fig. 3-11, instrumenting 22 discrete strain rosettes at the center of each iFEM element on the top surface of the structure is sufficient. In addition, 22 FBG sensors are embedded within the laminate at a thickness position of 1.2 [mm] away from the top surface of the laminate at the interface of layers $k = 3$ and $k = 4$. Both strain rosettes and the FBG sensors are aligned along the x_1 axis (length coordinate) of l_1 and l_2 lines as depicted in Fig. 3-12. To apply the discussed clamped boundary condition in the experiment, a specific portable test fixture is used which can be paired with any typical tensile test machine (e.g., INSTRON test machines) [87].

Fig. 3-12. Experimental deployment of the sensors on the laminate and strain-data collection systems.

As seen in Fig. 3-12, the strain data of the FBG sensors are acquired through two optical sensing interrogator modules whereas the in-situ strain data related to the rosettes are collected by National Instrument (NI) data acquisition system during the mechanical test.

Table 3-6. Laminate stacking sequences

Laminate	Lamina thickness, $2h^{(k)}$[mm]	Lamina materials	Lamina orientation [°]
Twill Woven Sandwich	6.0/14.0/4.8/1.2	CT/M/$(CT)_2$	0/0/0/0

The head of the loading machine pushes the structure downward with a constant velocity of 0.1 [mm/sec] until reaching the maximum deflection of 7 [mm] and is fixed at this position for 50 seconds and then the plate is unloaded at the same rate of the velocity as shown in Fig. 3-13. Such an experimental real-time loading with the constraint conditions ensures a quasi-static torsion/twisting test case on the given wing shape laminate.

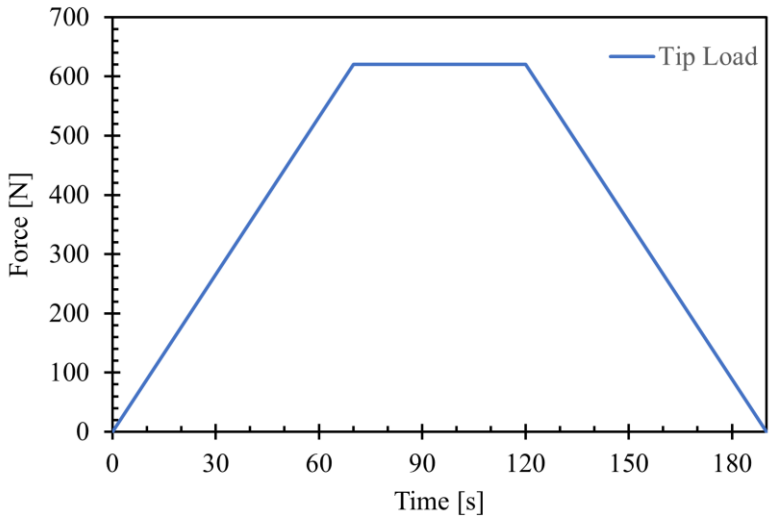

Fig. 3-13. Time dependent variation of force at the tip of the wing shaped sandwich structure.

The loading and unloading procedures are repeated three times to avoid any error in the results and ensure repeatability of the findings. Corresponding force to the maximum displacement is calculated by taking an average value of obtained force data. To establish a reliable and comparable reference solution, a high-fidelity FEM model with identical geometric and boundary conditions is analyzed using ANSYS-APDL software. For such analysis, the plate is discretized into 1386 quadrilateral subdomains possessing 10700 DOFs. The experimental data collected from strain sensors are used as an input for both iFEM-RZT and -FSDT analyses.

To perform these analyses, the whole domain of the plate is divided into 22 quadrilateral subdomains, representing iRZT4 and iQS4 inverse elements as shown in Fig. 3-14(a). Note that the center of these elements is corresponding to the discrete locations of experimental measurement sets. The weighting constants related to the membrane, bending, and zigzag section strains are set to one whereas the weighting coefficients of the transverse shear strains are equated to $w_\gamma = 10^{-7}$ and $w_\eta = 10^{-8}$ for iFEM-RZT, and $w_\gamma = 10^{-8}$ for iFEM-FSDT. Despite the absence of shear and lateral strains for FBG sensors (i.e., only the uniaxial strains are collected along x_1 direction), the corresponding weighting constants are kept as unity to preserve the compatibility of zigzag strains along different coordinate directions.

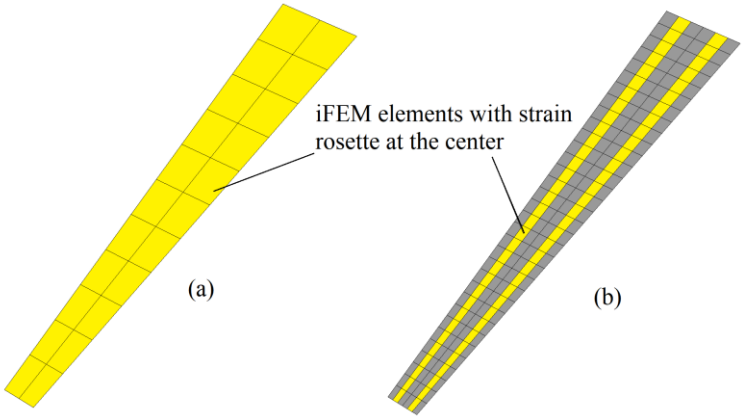

Fig. 3-14. Mesh resolution and iRZT4 elements with strain measurement sets at the center for a) iFEM-RZT and -FSDT analyses, b) iFEM analysis using polynomial smoothing approach.

To compare the performance of the iFEM elements (i.e., iRZT4, and iQS4), the total displacement contours of the wing-shaped sandwich laminate are plotted as illustrated in Fig. 3-15(b). Moreover, as thoroughly explained in [64], a speckle pattern is applied to one edge of the wing-shaped structure to create a suitable surface area for full-field displacement monitoring using a 2D-DIC technique. A CCD camera is placed at a normal distance of 45cm from the edge of the wing. The viewpoint of the camera had a clear image up to 45cm away from the tip of the wing. The video taken during the loading of the structure is post-processed and imported an image into GOM correlate 2020 software for the DIC analysis. The constant thickness size of the wing shape sandwich structure is used for calibration of the software with respect to the taken images. The region of interest for DIC simulation is defined using square facets with a size of 25 × 25 pixels and a step size of 19×19 pixels.

The results of total displacement at the edge of the wing structure (obtained from DIC analysis) are presented in Fig. 3-15(a) at undeformed and maximum deformation states. The comparison of the values between DIC results and FEM solutions clearly shows a high agreement between the predicted experimental and numerical displacements. According to the displacement contours in Fig. 3-15(b), the iFEM-RZT approach can generate a total displacement contour indistinguishable from that of the FEM analysis whereas iFEM-FSDT can only reconstruct an erroneous deformed shape with the dissimilar contours/displacement magnitudes.

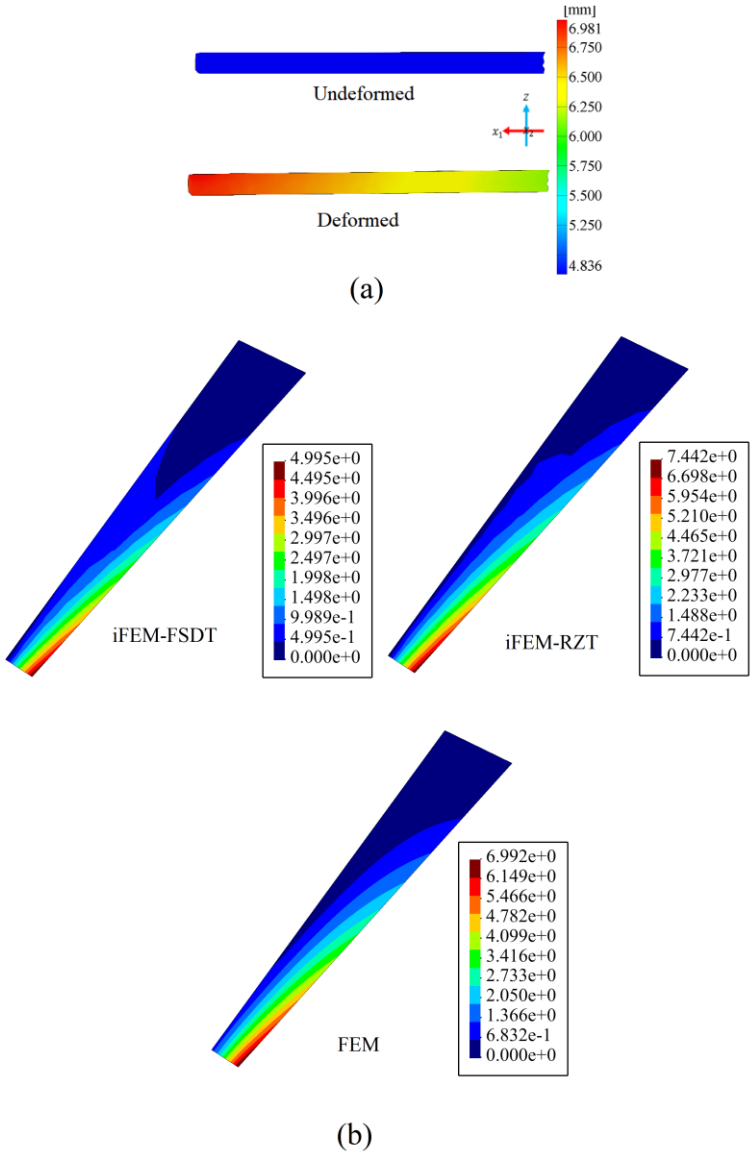

Fig. 3-15. a) Total displacement maps obtained via DIC images at undeformed and deformed states b) iFEM and FEM deflection contours of total displacement.

To elaborate on these results more quantitatively, the magnitudes of maximum total displacements can be compared to each other. The percent difference for the maximum total displacements between the iFEM-FSDT and FEM analyses is 35% whereas this difference reduces down to 6% only in the iFEM-RZT analysis, thereby demonstrating the adequately precise torsion-sensing capability of the iFEM-RZT approach for moderately thick sandwich structures. Besides, these results bespeak that, iFEM-FSDT is incapable of torsional displacement monitoring on thick laminated structures.

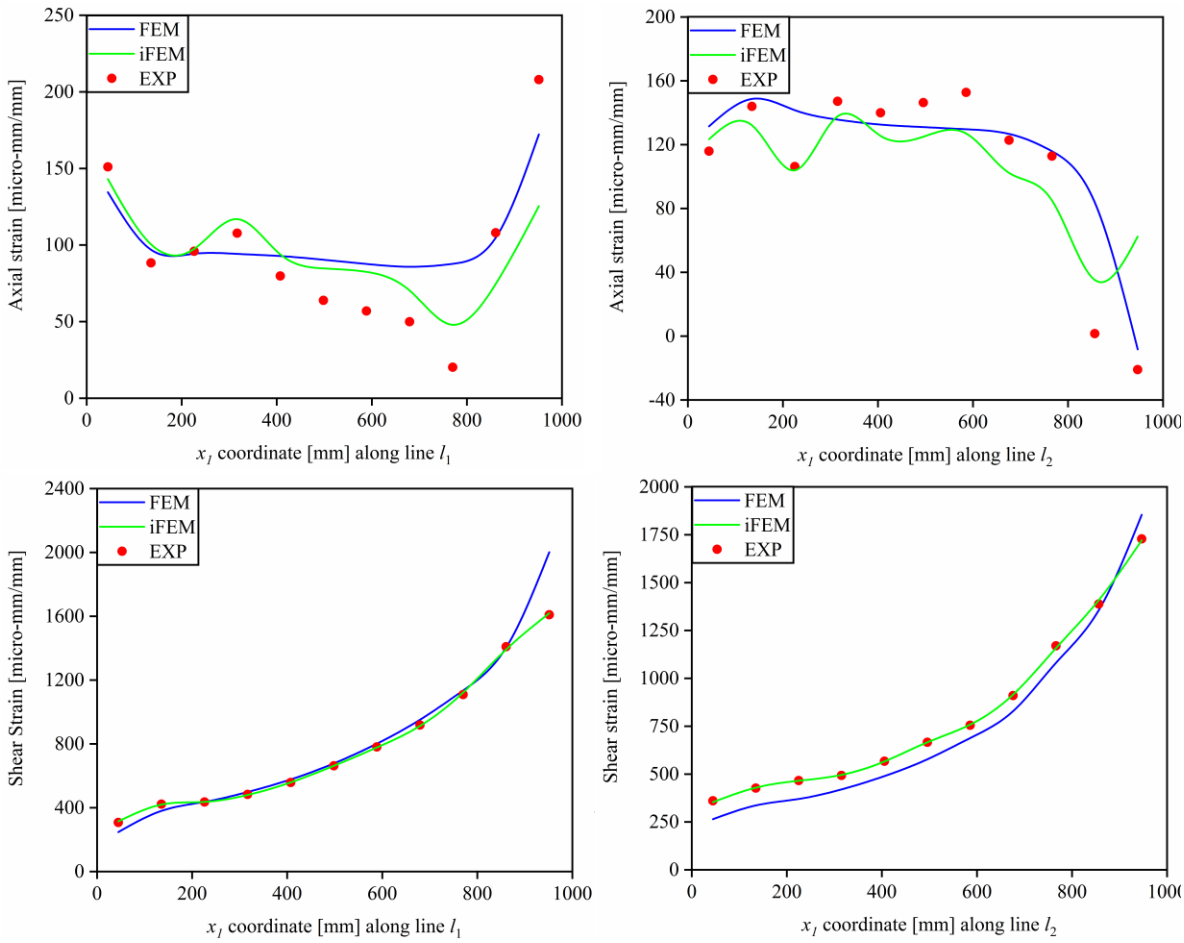

Fig. 3-16. Axial and shear strains of x_1 coordinate along lines l_1 and l_2.

In addition, a higher consistency between iFEM-RZT values and DIC full-field maps is also achieved as compared to those seen between iFEM-FSDT and DIC displacement measurements. From this quantitative comparison, it can be concluded that iFEM-RZT has a superior prediction capability than the iFEM-FSDT approach by considering the reference solution either as FEM or DIC. In Fig. 3-16, the experimental axial and shear strain results along l_1 and l_2 lines are compared with numerical 'FEM' strains. The term 'EXP' in the legend of Fig. 3-16 represents 11 discrete experimental strain collected along each of the lines l_1 and l_2. As an important result, it can be inferred from Fig. 3-16 that the shear strains are the dominant strains. This behavior is expected due to the torsional deformation of the structure.

Moreover, one can easily observe that there is an overall acceptable agreement between the numerical and experimental data, especially regarding the shear strains. However, the

discrete axial experimental data do not match exactly with the numerical trend (Fig. 3-16). This inconsistency might be due to the presence of inherent noise during experimental data collection which reduces the signal-to-noise ratio in small strain levels. Nevertheless, since the axial strains do not have a major contribution compared to the shear strains, their nonconforming effect is negligible for the torsional deformations of the laminate.

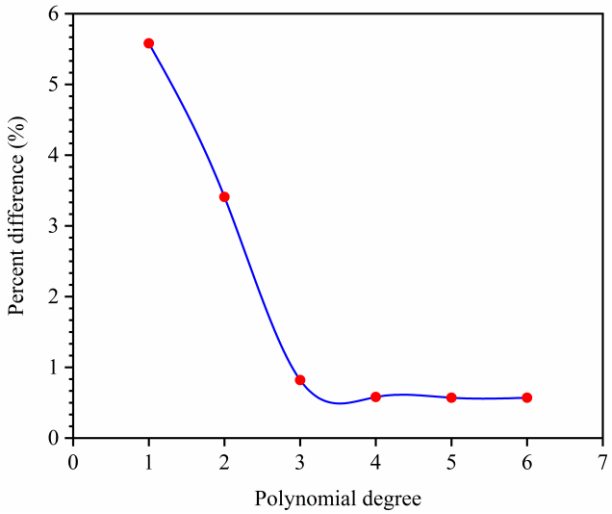

Fig. 3-17. Percent difference between maximum values of total displacement for FEM and iFEM-RZT analyses using different degrees of pre-extrapolation technique.

Similar to numerical examples in previous sections, a polynomial smoothing method is performed over discrete sets of experimental strain data to make the obtained results of the iFEM-RZT analyses more accurate. For this purpose, each iFEM element is divided into nine sub-elements to provide a finer mesh resolution as shown in Fig. 3-14(b). Afterward, a first- to sixth-degree polynomial line and curves are fitted through these discrete strain data providing a higher number of strain measurements available along l_1 and l_2 lines. Consequently, extra pre-computed strain data are generated and used as input in the iFEM-RZT analyses. Herein, the corresponding weighting constants of the membrane, bending, and zigzag strains for the elements having sensor are set to unity. However, for sensor-less elements, these coefficients are defined as a very small value (i.e.,10^{-9}). The weighting constants corresponding to transverse shear strains are set to $w_\gamma = 10^{-7}$, $w_\eta = 10^{-8}$.

Percent differences of the maximum total displacement between smoothed iFEM-RZT and FEM analyses corresponding to each degree of the polynomials are illustrated in Fig. 3-

17. Here, the utilization of the first-degree (linear) polynomial reduces the error percentage to below 6%. Moreover, in the case of the second-and third-degree polynomials, the percent differences come below 4% and 1% in the given order. Furthermore, it can be observed from the results that using the higher-order polynomials does not make further drastic reductions and provide stable convergency to a constant value of 0.57% between iFEM-RZT and reference solution. Hence, it can be concluded that for this special case study, third or fourth-degree polynomials can provide excellent deformation reconstruction in the iFEM-RZT analyses. Overall, this case study experimentally verifies the torsion-sensing capability of the new iRZT4 inverse-shell element and demonstrates the practical utility of the strain pre-extrapolation technique for the iFEM-RZT approach. Finally, the computational strategy presented herein can be leveraged to design precise and efficient applications of iFEM-RZT/iRZT4 methodology to shape sensing of thick sandwich structures using sparse sensor deployments with few sensors.

3.4. Conclusions

Numerical and experimental shape sensing of the moderately thick sandwich plate/shell structures is investigated using the iFEM-RZT approach coupled with strain pre-extrapolation technique. This method is based on the weighted least square functional which enforces the compatibility between analytical and experimental strains. Both numerically and experimentally acquired section strains from three surfaces through the thickness of the sandwich structure are successfully used as the main input for iFEM-RZT formulation. To this end, a new four-node RZT based quadrilateral inverse-shell element called iRZT4, with nine degrees of freedom at each node, is developed and utilized. To verify the accuracy and efficiency of the iRZT4 inverse-shell element, a stiffened sandwich plate, a curved sandwich shell and a wing-shaped sandwich structure are considered as two numerical and one experimental case studies, respectively. Moreover, iFEM-FSDT analysis and reference FEM solution are performed to be compared with iFEM-RZT analysis. Consequently, for both numerical and experimental case studies, a suitable pre-extrapolation technique is implemented using various degree polynomial fitting curves to make the obtained results smoother. Additionally, full-field displacement contours obtained by the DIC technique are used as an extra evaluation method for comparison of the data through iFEM-RZT and -FSDT analyses. Obtained results from numerical and experimental case studies clearly

indicate that iFEM-FSDT is not robust enough to be used as a highly precise shape sensing system for moderately thick sandwich structures. However, iFEM-RZT shows superior performance for the reconstruction of the displacement contours and quantitative results as compared to those of iFEM-FSDT analysis. Besides, it is observed that the in-plane shear strain measurements have a significant contribution to torsional deformations in the experimental case study. Hence, utilizing triaxial strain gauges (i.e., strain rosettes) is crucial to capture precise three-dimensional torsional deformations. To sum up, the obtained results of the iFEM-RZT approach coupled with strain pre-extrapolation technique provide robust and reliable real-time shape sensing of moderately thick sandwich plate/shell structures.

3.5. Appendix

The shape functions N_i, L_i, and M_i, which are used to describe membrane, bending and zigzag capability of the iRZT4 element as given in Eqs. (5a–d), are respectively defined as:

$$\begin{aligned} &N_i = \frac{1}{4}(1+s_i\,s)(1+t_i\,t) \quad (i=1,2,3,4), \\ &N_{i+4} = \frac{1}{2}(1-s^2)(1+t_i\,t) \quad (i=1,3),\ N_{i+4} = \frac{1}{2}(1+s_i\,s)(1-t^2) \quad (i=2,4) \end{aligned} \tag{A.1}$$

$$M_i = a_j N_{j+4} - a_i N_{i+4},\ L_i = b_j N_{j+4} - b_i N_{i+4}\ (i=1,2,3,4;\ j=4,1,2,3) \tag{A.2}$$

with

$$a_i = \frac{x_i - x_k}{8},\ b_i = \frac{y_k - y_i}{8}\ (i=1,2,3,4;k=2,3,4,1) \tag{A.3}$$

where the $s_i, t_i \in [-1,+1]$ $(i=1,2,3,4)$ symbols represent the isoparametric coordinates of iRZT4 element's nodes. The derivatives of shape functions given in Eqs. (A1-A3) can be calculated with respect to x_1 and x_2 axes to define the strain measures of the iRZT4 element. As given in Eqs. (7a-e), these section strains are computed by the $\mathbf{B}^{\chi} = \left[\mathbf{B}_1^{\chi} \quad \mathbf{B}_2^{\chi} \quad \mathbf{B}_3^{\chi} \quad \mathbf{B}_4^{\chi}\right]$ $(\chi = \mathbf{e}, \boldsymbol{\kappa}, \boldsymbol{\mu}, \boldsymbol{\gamma}, \boldsymbol{\eta})$ matrices, which are explicitly defined as:

$$\mathbf{B}_i^{\mathbf{e}} \equiv \begin{bmatrix} N_{i,1} & 0 & 0 & 0 & 0 & L_{i,1} & 0 & 0 & 0 \\ 0 & N_{i,2} & 0 & 0 & 0 & M_{i,2} & 0 & 0 & 0 \\ N_{i,2} & N_{i,1} & 0 & 0 & 0 & L_{i,2}+M_{i,1} & 0 & 0 & 0 \end{bmatrix} \tag{A.4}$$

$$\mathbf{B}_i^{\kappa} \equiv \begin{bmatrix} 0 & 0 & 0 & 0 & N_{i,1} & 0 & 0 & 0 & 0 \\ 0 & 0 & 0 & -N_{i,2} & 0 & 0 & 0 & 0 & 0 \\ 0 & 0 & 0 & -N_{i,1} & N_{i,2} & 0 & 0 & 0 & 0 \end{bmatrix} \tag{A.5}$$

$$\mathbf{B}_i^{\mu} \equiv \begin{bmatrix} 0 & 0 & 0 & 0 & 0 & 0 & 0 & N_{i,1} & 0 \\ 0 & 0 & 0 & 0 & 0 & 0 & -N_{i,2} & 0 & 0 \\ 0 & 0 & 0 & 0 & 0 & 0 & 0 & N_{i,2} & 0 \\ 0 & 0 & 0 & 0 & 0 & 0 & -N_{i,1} & 0 & 0 \end{bmatrix} \tag{A.6}$$

$$\mathbf{B}_i^{\eta} \equiv \begin{bmatrix} 0 & 0 & N_{i,1} & -L_{i,1} & -M_{i,1}+N_i & 0 & L_{i,1} & M_{i,1}-N_i & 0 \\ 0 & 0 & N_{i,2} & -L_{i,2}-N_i & -M_{i,2} & 0 & L_{i,2}+N_i & M_{i,2} & 0 \end{bmatrix} \tag{A.7}$$

$$\mathbf{B}_i^{\gamma} \equiv \begin{bmatrix} 0 & 0 & N_{i,1} & -L_{i,1} & -M_{i,1}+N_i & 0 & L_{i,1} & M_{i,1} & 0 \\ 0 & 0 & N_{i,2} & -L_{i,2}-N_i & -M_{i,2} & 0 & L_{i,2} & M_{i,2} & 0 \end{bmatrix} \tag{A.8}$$

where the subscript $i = 1,2,3,4$ corresponds to the local node numbers. Note that the derivative operation for calculating $N_{i,j}, L_{i,j}, M_{i,j}$ $(j = 1,2)$ functions can be achieved by using chain rule and associated Jacobian matrix $\mathbf{J}$ as follows:

$$\begin{Bmatrix} \chi_{i,1} \\ \chi_{i,2} \end{Bmatrix} = \mathbf{J}^{-1} \begin{Bmatrix} \chi_{i,s} \\ \chi_{i,t} \end{Bmatrix} \quad (\chi = N, L, M), \quad \mathbf{J} = \begin{bmatrix} x_{1,s} & x_{2,s} \\ x_{1,t} & x_{2,t} \end{bmatrix} \tag{A.9}$$

where the comma subscript followed by isoparametric axes (s, t) indicates the partial derivative of $(\cdot)_{,\alpha} = \frac{\partial(\cdot)}{\partial \alpha}$ $(\alpha = s, t)$.

CHAPTER 4. Experimental and Numerical Investigation on Large Deformation Reconstruction of Thin Laminated Composite Structures Using Inverse Finite Element Method

The inverse finite element method (iFEM) is one of the best candidates to perform displacement monitoring (shape sensing) of structures using a set of on-board/embedded strain sensors. This study demonstrates the high efficiency, robustness, and accuracy of the iFEM approach to reconstruct geometrically non-linear deformations of thin laminated plates and shells by performing experimental measurements and numerical analyses. The iFEM formulation is derived based on the first-order shear deformation theory of plates. A weighted least-squares variational principle is utilized with incremental non-linear strains while performing the geometrical update of the model using predicted incremental deformations. Moreover, a quadrilateral inverse-shell element (iQS4) is employed to discretize the whole domain of the laminated panels and solve the numerical/experimental shape-sensing problems. Further, a polynomial strain pre-extrapolation technique is incorporated with the iQS4 formulation to smoothen the discrete strain data obtained from a few strain rosettes placed along the entire length of the structures. For each case study, a high-fidelity finite element analysis is performed to establish a reference displacement solution. Finally, the qualitative and quantitative comparison of reconstructed displacement results with reference solutions confirms the superior potential of the iFEM-iQS4 approach for full-field shape sensing of thin laminates undergoing non-linear deformations.

4.1. Introduction

Long fiber-reinforced polymer composites with advanced mechanical performances are commonly used to manufacture laminated structures of two or more plies with variable fiber angles to offer high flexural rigidity and lighter weight. These laminated structures can be classified according to their span-to-thickness ratio as thin (slender), moderately thick, and thick plates or shells [92]. Among this class of composites, thin laminated plates are widely used for various types of aerospace, marine, and civil structures due to their improved mechanical properties, i.e., long fatigue life [93-94], high strength [95-96], and superior corrosion resistance [97]. However, the thin laminated structures are susceptible to geometrically non-linear displacements due to harsh operating conditions, such as large

deflections and/or buckling deformations. Therefore, the safety of these structures must be ensured by a reliable inspection system in real time. To this end, structural health monitoring (SHM) systems can be effectively employed to dynamically track large structural deformations for predicting any occurrence of progressive damage accumulation before catastrophic structural failure. For instance, in the last few decades, various SHM techniques have been used to detect damage and failure modes of composite structures utilizing embedded and/or surface-mounted sensor systems [98-101]. Hence, smart composites integrated with sensors and SHM systems is key to future engineering science and technology.

Shape sensing is one of the critical aspects of SHM systems that deals with the real-time reconstruction of deformation levels on structural components. This approach utilizes experimental strain data collected from a network of on-board/embedded sensors which can be transmitted via wireless or wired (conventional) techniques to data processing platforms. Fiber Bragg Grating (FBG) sensors and strain rosettes are among the wired systems primarily used in composite structures due to their simple and efficient applicability. FBG sensors are flexible and durable enough to embed in composite materials easily. When these sensors are embedded in the laminated structure, they can observe temporary and permanent strain variations at discrete positions within the composite materials [102-104]. Shape sensing is an inverse problem. Inverse problems arise in a variety of sensing applications. Recently, data-driven methods using neural networks have been shown to be significantly superior to classical solution methods for inverse problems [105]. Moreover, surrogate modelling is also created to speed up the solution of the inverse problems as well [106]. To obtain a full-field displacement solution, in-situ sensor measurements must be employed in an inverse method to solve the shape-sensing problem. To this end, several inverse methods such as modal [6-8], curve-fitting [11], and analytical [12] approaches have been proposed in the literature. The inverse finite element method is a state-of-the-art robust shape-sensing algorithm [14-15] that has recently attracted much more attention than other inverse methods due to its unique features. These advantages mainly include (i) no requirement of loading/material information and (ii) full-field deformation reconstruction capability over the entire structural domain.

The iFEM method was initially developed based on the first-order shear deformation theory (FSDT) for the shape estimation of plate structures. The critical input of this method is triaxial strain data obtained from a discrete number of on-board sensors, e.g., strain rosettes. The iFEM algorithm minimizes the difference between the calculated numerical strains and their experimental counterparts utilizing a weighted least-squares functional. Thus far, different types of the inverse beam [34,81] and plate/shell [42-44] elements have been proposed using iFEM methodology for real-time monitoring of complex deformed shapes. In a recent comparative study, the performance of C^0-continuous inverse shell elements was investigated for shape sensing and damage detection of various plate/shell-like geometries [16]. Furthermore, experimental, and numerical studies leveraged the iFEM algorithm for displacement and stress monitoring of different marine [19,22,28,53] aerospace [49,56,107,108], and civil structures [109-111]. Also, recent research efforts have addressed the optimal placement of sensors for iFEM analyses using effective optimization methods [112-114].

Additionally, isogeometric iFEM formulations were developed for displacement monitoring of thin-shell [82,115] and beam-like [83-84] structures. Most recently, Kefal et al. [116] have introduced coupling of iFEM methodology with a nonlocal meshless approach known as peridynamics for crack propagation monitoring of laminated composite plates. Besides, the ability of the iFEM approach was numerically demonstrated for shape sensing of isotropic plates undergoing large deformations [117]. Since the FSDT-based iFEM method may not always be applicable to accurate reconstruction of the displacement, strain, and stress fields of thick multi-layered composite and sandwich structures, enhanced iFEM formulations [39-40] were developed by extending kinematic relations towards zigzag theories [88]. On this basis, smoothed iFEM approach has been proposed by coupling enhanced iFEM formulation with smoothing element analysis for effective shape sensing application [87]. The predictive capability of the enhanced iFEM approaches was numerically and experimentally assessed on real-time displacement monitoring of moderately thick sandwich structures [17,118]. In addition to top/bottom sensor, these iFEM formulations require an additional set of interlaminar in-situ strain data (which can be obtained from embedded FBG sensors) for thick structures. Therefore, the iFEM-FSDT formulation is preferable compared to enhanced iFEM methods in terms of practical

experimental implementation on thin-walled structures with a smaller number of strain sensors. Real-time deformation prediction of thin laminated plates/shells plays a critical role in the realistic assessment of structural damage and fatigue life of structural components used in today's engineering industry. In this regard, the need for an extensive numerical-experimental application of iFEM-FSDT to thin-walled composite structures is evident. Nevertheless, the predictive capability of the iFEM algorithm has not been assessed for reconstructing geometrical nonlinear deformations of thin composite structures subjected to bending and/or post-buckling loads. Among the myriad of computational or experimental shape-sensing investigations, the application of iFEM-FSDT to displacement monitoring of composites is limited to only a few studies, which include linear elastic shape-sensing of thin composite structures under thermo-mechanical [118], compressive linear-buckling [89], and impact [119] loads.

To fill the critical gap mentioned above, this study performs geometrically nonlinear deformation reconstruction of thin composite plates and shells using experimental strain measurements employing iFEM-FSDT formulation for the first time. Therefore, the novelty of this study lies in the numerical and experimental investigation of the iFEM-FSDT approach for shape sensing of thin laminated structures undergoing large bending/post-buckling deflections in real time. For this purpose, two numerical and one experimental study cases are performed to verify the iFEM approach for nonlinear shape sensing of thin laminates. A robust and computationally efficient quadrilateral inverse shell element (iQS4) [43] is used to perform the nonlinear iFEM analysis. This inverse element needs less computational time compared to other existing inverse curved shell element (iFEM-iCS8). In addition, the iFEM-iQS4 model is extended through a smoothing analysis to recover continuous strains from discrete strain measurements obtained during the experimental test. Finally, the obtained iFEM results are validated by the reference solutions generated using a well-known commercial finite element software, i.e., ANSYS APDL.

This paper is organized in the following order. In Section 2, the fundamental formulation of the iQS4 element, the algorithm of nonlinear-displacement geometric update, and the polynomial smoothing approach are summarized. Section 3 first describes the numerical examples, (1) a post-buckling analysis of a thin laminated plate and (2) bending

analysis of a curved plate with large deflection using the iFEM technique. Then, experimental shape-sensing implementation of iFEM-iQS4 for thin laminated plate is elaborated in Section 3. Finally, in Section 4, several important implications are drawn from the iFEM results of the thin multi-layered composite structures exposed to large bending/buckling deformations.

4.2. Theoretical Framework

4.2.1 The iFEM-iQS4 Element for Shape Sensing of Thin Laminated Structures

The iQS4 is an inverse shell element with four nodes, originally developed by Kefal et al. [43], for shape and stress sensing of plate/shell structures. Each node of this inverse element has three translational (v_{1i}, v_{2i}, v_{zi}) and three rotational ($\theta_{1i}, \theta_{2i}, \theta_{zi}$) degrees of freedom (DOF) with the positive directions as shown in Fig. 4-1(a). With the use of hierarchical drilling rotation DOF, θ_{zi}, this element becomes a robust iFEM tool for modelling curved/blade-stiffened shell geometries. Mathematical fundamentals for the development of the elements with drilling DOF were investigated in detail by Hughes and Brezzi [60].

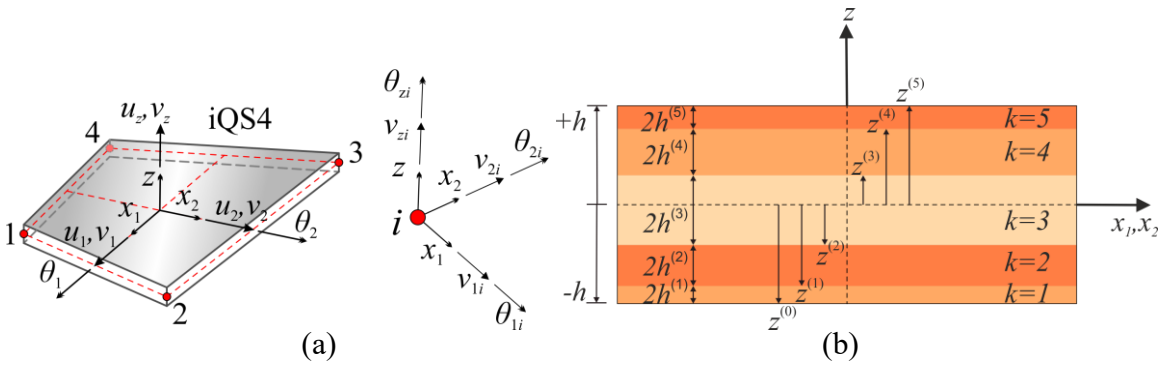

Fig. 4-1. (a) Geometry of iQS4 inverse shell element with associated coordinates and its nodal DOFs, (b) Cross-section of a laminated panel.

The element has a total thickness of 2*h*, and therefore its thickness coordinate is defined as $z \in (-h, +h)$. Besides, the element is oriented with respect to a local (element) coordinate system, $\mathbf{x} \equiv (x_1, x_2)$, representing the in-plane coordinates of the element. Here, the iQS4 element is employed to model a laminate with a total number of n_L layers (made of isotropic or orthotropic materials) as shown in Fig. 4-1(b). The laminate notation can be described as

follows. The superscript (*k*) is utilized to identify the interlaminar strain field and thickness coordinate between $(k-1)$-th and k-th plies. Besides, the (*k*)-th lamina has thickness of $2h^{(k)}$ with the top and bottom thickness coordinates, $z^{(k-1)}$ and $z^{(k)}$, respectively, as illustrated in Fig. 4-1(b).

Regardless of the individual ply kinematics, the in-plane and out-of-plane displacement components of any material point can be described according to FSDT as a function of five independent kinematic variables as:

$$u_1(\mathbf{x},z) = v_1(\mathbf{x}) + z\theta_2(\mathbf{x}) \tag{1}$$

$$u_2(\mathbf{x},z) = v_2(\mathbf{x}) - z\theta_1(\mathbf{x}) \tag{2}$$

$$u_z(\mathbf{x},z) = v_z(\mathbf{x}) \tag{3}$$

where translational (v_1, v_2, v_z) and rotational (θ_1, θ_2) kinematic variables can be approximated utilizing shape functions of the iQS4 element as [43]:

$$v_1(\mathbf{x}) = \sum_{i=1}^{4}\left(N_i v_{1i} + L_i\theta_{zi}\right) \tag{4}$$

$$v_2(\mathbf{x}) = \sum_{i=1}^{4}\left(N_i v_{2i} + M_i\theta_{zi}\right) \tag{5}$$

$$v_z(\mathbf{x}) = \sum_{i=1}^{4}\left(N_i v_{zi} - L_i\theta_{1i} - M_i\theta_{2i}\right) \tag{6}$$

$$\theta_i(\mathbf{x}) = \sum_{j=1}^{4} N_j\theta_{ij} \quad (i=1,2) \tag{7}$$

where the isoparametric mapping of in-plane coordinates to parent domain (s,t) can be performed using the nodal coordinates of the iQS4 element, x_{1i}, x_{2i} $(i=1,2,3,4)$, as:

$$\mathbf{x} = \begin{Bmatrix} x_1(s,t) \\ x_2(s,t) \end{Bmatrix} = \sum_{i=1}^{4} N_i \begin{Bmatrix} x_{1i} \\ x_{2i} \end{Bmatrix} \tag{8}$$

In Eqs. (4-7), the $L_i \equiv L_i(s,t)$ and $M_i \equiv M_i(s,t)$ functions are the second order anisoparametric shape functions [118], and $N_i \equiv N_i(s,t)$ is bilinear isoparametric shape functions. The explicit form of these shape functions can be found in references [43, 46].

Substituting Eqs. (4-7) to Eqs. (1-3) and subsequently taking the spatial derivatives of the resultant displacement vector according to infinitesimal strain theory, the in-plane, $\boldsymbol{\varepsilon}$, and transverse-shear, $\boldsymbol{\gamma}$, strains at every position of the plate/shell domain can be derived analytically in terms of the nodal DOF vector of the iQS4 element, $\mathbf{u}^e$, as:

$$\boldsymbol{\varepsilon}(\mathbf{u}^e) = \mathbf{e}(\mathbf{u}^e) + z\boldsymbol{\kappa}(\mathbf{u}^e) = (\mathbf{B}^e + z\mathbf{B}^\kappa)\mathbf{u}^e \tag{9}$$

$$\boldsymbol{\gamma}(\mathbf{u}^e) = \mathbf{B}^\gamma \mathbf{u}^e \tag{10}$$

$$\mathbf{u}^e = \begin{bmatrix} \mathbf{u}_1^e & \mathbf{u}_2^e & \mathbf{u}_3^e & \mathbf{u}_4^e \end{bmatrix}^T \tag{11}$$

$$\mathbf{u}_i^e = \begin{bmatrix} v_{1i} & v_{2i} & v_{zi} & \theta_{1i} & \theta_{2i} & \theta_{zi} \end{bmatrix} \ (i = 1,2,3,4) \tag{12}$$

where $\mathbf{u}_i^e$ represents the DOF of the *i*-th node, the $\mathbf{e}(\mathbf{u}^e)$ and $\boldsymbol{\kappa}(\mathbf{u}^e)$ vectors are the membrane and bending section strains, respectively, and the $\mathbf{B}^\chi = \begin{bmatrix} \mathbf{B}_1^\chi & \mathbf{B}_2^\chi & \mathbf{B}_3^\chi & \mathbf{B}_4^\chi \end{bmatrix} (\chi = e, \kappa, \gamma)$ matrices are the strain-displacement matrices of the iQS4 element. These matrices contain derivatives of the shape functions with respect to x_1 and x_2 axes and can be explicitly described as [43]:

$$\mathbf{B}_i^e \equiv \begin{bmatrix} N_{i,1} & 0 & 0 & 0 & 0 & L_{i,1} \\ 0 & N_{i,2} & 0 & 0 & 0 & M_{i,2} \\ N_{i,2} & N_{i,1} & 0 & 0 & 0 & L_{i,2} + M_{i,1} \end{bmatrix} (i = 1,2,3,4) \tag{13}$$

$$\mathbf{B}_i^\kappa \equiv \begin{bmatrix} 0 & 0 & 0 & 0 & N_{i,1} & 0 \\ 0 & 0 & 0 & -N_{i,2} & 0 & 0 \\ 0 & 0 & 0 & -N_{i,1} & N_{i,2} & 0 \end{bmatrix} (i = 1,2,3,4) \tag{14}$$

$$\mathbf{B}_i^\gamma \equiv \begin{bmatrix} 0 & 0 & N_{i,1} & -L_{i,1} & -M_{i,1} + N_i & 0 \\ 0 & 0 & N_{i,2} & -L_{i,2} - N_i & -M_{i,2} & 0 \end{bmatrix} (i = 1,2,3,4) \tag{15}$$

where the comma subscript followed by 1 and 2 indicates the partial derivative of $(\cdot)_{,\alpha} = \frac{\partial(\cdot)}{\partial x_\alpha} (\alpha = 1,2)$. Using the chain rule and the inverse of the Jacobian matrix of the iQS4 element, one can calculate the derivatives of the shape functions, $N_{i,j}, L_{i,j}, M_{i,j}$ $(j = 1,2)$, as:

$$\begin{Bmatrix} \chi_{i,1} \\ \chi_{i,2} \end{Bmatrix} = \begin{bmatrix} x_{1,s} & x_{2,s} \\ x_{1,t} & x_{2,t} \end{bmatrix}^{-1} \begin{Bmatrix} \chi_{i,s} \\ \chi_{i,t} \end{Bmatrix} \quad (\chi = N, L, M) \tag{16}$$

where the symbol $(\cdot)_{,\alpha} = \frac{\partial(\cdot)}{\partial \alpha}$ $(\alpha = s, t)$ indicates the partial derivatives of the shape functions or local in-plane coordinates with respect to the isoparametric coordinates.

The experimental surface strains collected from the on-board strain rosettes and/or embedded FBG sensors are the main input of the iFEM-iQS4 formulation. To provide this data, the sensors must be located in at least two different positions along the thickness coordinate of the laminate for a given discrete in-plane position, $\mathbf{x}_i \equiv (x_1, x_2)_i$ $(i = 1, 2, ..., n_S)$, where the n_S represents the number of the two strain rosettes set. For clarity, an example of sensor placement configuration is depicted in Fig. 4-2, where $\boldsymbol{\varepsilon}_i^{(\chi)}$ $(\chi = k_1, k_2)$ denotes the interlaminar triaxial strains measured at k_1 and k_2 interface of the plies at $\mathbf{x}_i$ position. Here, $k_i \in [0, n_L]$ $(i = 1, 2)$ interfaces can be assigned to any arbitrarily integer and it is assumed that k_2 interface is closer to the top surface of the laminate than k_1 interface as such $k_2 > k_1$

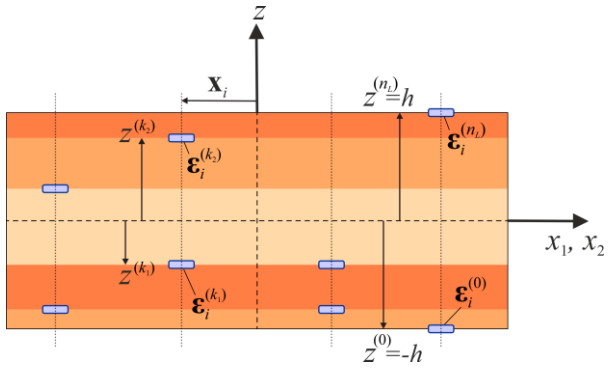

Fig. 4-2. Layout of strain sensors along the thickness coordinate of the thin laminated composite structure.

Utilizing the in-plane strain definition given in Eq. (9), experimental surface strains, $\boldsymbol{\varepsilon}_i^{(k_1)}$ and $\boldsymbol{\varepsilon}_i^{(k_2)}$, can be expressed in terms of the experimental membrane, $\mathbf{e}^{\varepsilon}$, and bending, $\boldsymbol{\kappa}^{\varepsilon}$, section strains as:

$$\boldsymbol{\varepsilon}_i^{(k_1)} \equiv \boldsymbol{\varepsilon}(\mathbf{x}_i, z^{(k_1)}) = \mathbf{e}^{\varepsilon}(\mathbf{x}_i) + z^{(k_1)} \boldsymbol{\kappa}^{\varepsilon}(\mathbf{x}_i) \tag{17}$$

$$\boldsymbol{\varepsilon}_i^{(k_2)} \equiv \boldsymbol{\varepsilon}(\mathbf{x}_i, z^{(k_2)}) = \mathbf{e}^{\varepsilon}(\mathbf{x}_i) + z^{(k_2)}\boldsymbol{\kappa}^{\varepsilon}(\mathbf{x}_i) \tag{18}$$

which be solved to obtained general description of experimental membrane and bending section strains of laminate with n_L plies as:

$$\mathbf{e}^{\varepsilon}(\mathbf{x}_i) \equiv \mathbf{e}_i^{\varepsilon} = \frac{\boldsymbol{\varepsilon}_i^{(k_1)} z^{(k_2)} - \boldsymbol{\varepsilon}_i^{(k_2)} z^{(k_1)}}{\sum_{k=k_1+1}^{k_2} 2h^{(k)}} \quad (i = 1,2,...,n_S;\ k_2 > k_1) \tag{19}$$

$$\boldsymbol{\kappa}^{\varepsilon}(\mathbf{x}_i) \equiv \boldsymbol{\kappa}_i^{\varepsilon} = \frac{\boldsymbol{\varepsilon}_i^{(k_2)} - \boldsymbol{\varepsilon}_i^{(k_1)}}{\sum_{k=k_1+1}^{k_2} 2h^{(k)}} \quad (i = 1,2,...,n_S;\ k_2 > k_1) \tag{20}$$

It is important to recall that the $\mathbf{e}_i^{\varepsilon}$ and $\boldsymbol{\kappa}_i^{\varepsilon}$ vectors are the experimental counterparts of the membrane, $\mathbf{e}(\mathbf{u}^e)$, and bending, $\boldsymbol{\kappa}(\mathbf{u}^e)$, section strains given in Eq. (9), and thus can be directly computed during the experimental test given that the $\boldsymbol{\varepsilon}_i^{(k_1)}$ and $\boldsymbol{\varepsilon}_i^{(k_2)}$ are gathered by sensors. If no experimental test is available, these strain measurements can be simulated using numerical methods such as finite element method to be able to optimize sensor placement configurations for an experimental setup. If surface mounted strain gauges are located on top and bottom position of the laminate (i.e., no embedded FBG sensors), the interface indices are automatically set to $k_1 = 0;\ k_2 = n_L$ in Eqs. (19-20), leading to the original expression of the iFEM-iQS4 formulation for isotropic plates/shells as [14]:

$$\mathbf{e}_i^{\varepsilon} = \frac{\boldsymbol{\varepsilon}_i^{(0)} z^{(n_L)} - \boldsymbol{\varepsilon}_i^{(n_L)} z^{(0)}}{\sum_{k=1}^{n_L} 2h^{(k)}} = \frac{\boldsymbol{\varepsilon}_i^{(0)} h - \boldsymbol{\varepsilon}_i^{(n_L)}(-h)}{2h} = \frac{\boldsymbol{\varepsilon}_i^{(0)} + \boldsymbol{\varepsilon}_i^{(n_L)}}{2} \tag{21}$$

$$\boldsymbol{\kappa}_i^{\varepsilon} = \frac{\boldsymbol{\varepsilon}_i^{(n_L)} - \boldsymbol{\varepsilon}_i^{(0)}}{\sum_{k=1}^{n_L} 2h^{(k)}} = \frac{\boldsymbol{\varepsilon}_i^{(n_L)} - \boldsymbol{\varepsilon}_i^{(0)}}{2h} \tag{22}$$

where the vectors $\boldsymbol{\varepsilon}_i^{(n_L)}, \boldsymbol{\varepsilon}_i^{(0)}$ represent the top and bottom surface triaxial strains collected from sensors at any $\mathbf{x}_i$ position (Fig. 4-2). Unlike the membrane and bending section strains, experimental counterpart of the transverse-shear strains $\boldsymbol{\gamma}(\mathbf{u}^e)$ cannot be extracted directly using surface strain data, $\boldsymbol{\varepsilon}_i^{(\chi)}$ $(\chi = k_1, k_2)$. However, the contributions of transverse-shear

strains to large bending deformations can be ignored for shape sensing of thin-walled structures.

For an individual iQS4 element with the area of A^e, the weighted least-squares functional of iFEM methodology can be expressed based on calculated errors between analytical and experimental section strains as [15, 43]:

$$\Phi(\mathbf{u}^e)=\frac{1}{A^e}\iint_{A^e}\left(w_e\left\|\mathbf{e}(\mathbf{u}^e)-\mathbf{e}^{\varepsilon}\right\|^2+w_{\kappa}(2h)^2\left\|\boldsymbol{\kappa}(\mathbf{u}^e)-\boldsymbol{\kappa}^{\varepsilon}\right\|^2+w_{\gamma}\left\|\boldsymbol{\gamma}(\mathbf{u}^e)\right\|^2\right)dx_1dx_2 \tag{23}$$

where the w_e and w_{κ} represent the weighting constants related to the membrane and bending strains respectively, and w_{γ} stands for the weighting coefficient of transverse-shear strains that is always set to a small number compared to unity, e.g., $w_{\gamma}=10^{-5}$, due to the lack of experimental counterpart. In the case of $\mathbf{e}^{\varepsilon}$ and $\boldsymbol{\kappa}^{\varepsilon}$ section strains being available for the iQS4 element, the weighting coefficients take the value of unity ($w_e=w_{\kappa}=1$). Otherwise, they should be set to relatively small values such as $w_e=w_{\kappa}=10^{-5}$. Minimizing the $\Phi(\mathbf{u}^e)$ functional with respect to the unknown $\mathbf{u}^e$ nodal displacement of the iQS4 element, the final equation system of the element can be written as:

$$\frac{\partial\Phi(\mathbf{u}^e)}{\partial\mathbf{u}^e}=0\ \Rightarrow\ \mathbf{k}^e\mathbf{u}^e=\mathbf{f}^e \tag{24}$$

$$\mathbf{k}^e=\frac{1}{A^e}\iint_{A^e}\left(w_e(\mathbf{B}^e)^T\mathbf{B}^e+w_{\kappa}(2h)^2(\mathbf{B}^{\kappa})^T\mathbf{B}^{\kappa}+w_{\gamma}(\mathbf{B}^{\gamma})^T\mathbf{B}^{\gamma}\right)dx_1dx_2 \tag{25}$$

$$\mathbf{f}^e=\frac{1}{A^e}\iint_{A^e}\left(w_e(\mathbf{B}^e)^T\mathbf{e}^{\varepsilon}+w_{\kappa}(2h)^2(\mathbf{B}^{\kappa})^T\boldsymbol{\kappa}^{\varepsilon}\right)dx_1dx_2 \tag{26}$$

where the $\mathbf{k}^e$ and $\mathbf{f}^e$ indicate shape matrix and experimental strain vectors corresponding to an individual element in the given order. Note that, unlike shape matrix $\mathbf{k}^e$, the $\mathbf{f}^e$ vector is dependent on experimental measurements. To numerically compute the area integral in Eq. (26), the discrete values of the experimental section strains, $\mathbf{e}_i^{\varepsilon}$ and $\boldsymbol{\kappa}_i^{\varepsilon}$, given by Eqs. (19-20) are required at the Gauss points of the iQS4 element. One can employ *'a priori'* strain smoothing methods or "smoothed iFEM" to overcome this issue for practical applications [39]. Alternatively, if a single sensor set is available within the iQS4 element, then the

experimental data can be assigned uniformly to each Gauss integration point (e.g., the same $\mathbf{e}_i^{\varepsilon}$ and $\boldsymbol{\kappa}_i^{\varepsilon}$ values for each of four Gauss points). For reasonable averaging of the sensor data, the centroid element can be chosen to mount this sensor set [44]. A suitable transformation matrix, $\mathbf{T}^e$, should be utilized to transform the iFEM equation (Eq. 24) from local to global coordinate system, and then they can be assembled for the entire iQS4 discretization as:

$$\mathbf{KU} = \mathbf{F} \tag{27}$$

$$\mathbf{K} = \bigcup_{e=1}^{n_{el}} \left((\mathbf{T}^e)^T \mathbf{k}^e \mathbf{T}^e \right) \tag{28}$$

$$\mathbf{F} = \bigcup_{e=1}^{n_{el}} \left((\mathbf{T}^e)^T \mathbf{f}^e \right) \tag{29}$$

$$\mathbf{U} = \bigcup_{e=1}^{n_{el}} \left((\mathbf{T}^e)^T \mathbf{u}^e \right) \tag{30}$$

where n_{el} denotes the number of inverse elements for a given discretization, and the $\bigcup$ operator represents the finite element assembly process. The details of computing the $\mathbf{T}^e$ transformation matrix by using global coordinates of the nodes were given in reference [44]. In Eq. (27), the $\mathbf{K}$, $\mathbf{U}$ and $\mathbf{F}$ symbols are referred to global shape matrix, displacement vector and experimental strain vector, respectively. Note that since $\mathbf{F}$ vector is dependent on experimental strain data, it needs to be updated at each time step to provide a real-time monitoring system. After imposing displacement and loading boundary conditions, the Eq. (27) can be updated for the reduced forms of global equations. Then, an inversion process is performed to solve this equation system as:

$$\mathbf{K}_R \mathbf{U}_R = \mathbf{F}_R \;\; \Rightarrow \;\; \mathbf{U}_R = \mathbf{K}_R^{-1} \mathbf{F}_R \tag{31}$$

which provides the real-time deformations (nodal DOF of the entire iQS4 model) for any strain increment. To obtain more accurate non-linear large deformations reconstruction for a given strain increment step, ls, the global displacement vector of the nodes, $\mathbf{U}_i \equiv \begin{bmatrix} U_i & V_i & W_i \end{bmatrix}^T$ $(i = 1, 2, ..., n_{node})$, can be utilized to update the geometry of the iFEM-iQS4 domain before the shape analysis for next strain-increment step, $ls+1$, as:

$$(\mathbf{X}_i)_{ls+1} = (\mathbf{X}_i)_{ls} + (\mathbf{U}_i)_{ls} \quad (ls = 1,2,...,n_{step};\ i = 1,2,3,...,n_{node}) \tag{32}$$

where the vector $(\mathbf{X}_i)_{ls} \equiv \begin{bmatrix} X_i & Y_i & Z_i \end{bmatrix}_{ls}^T$ indicates the global coordinates of the *i*-th node at strain increment step of ls, the n_{node} and n_{step} symbols stand for the total number of nodes and strain-acquisition step. Note that the $(\mathbf{U}_i)_{ls}$ displacements are calculated by performing linear iFEM analysis. Nonlinear deformation reconstruction is enforced by using new geometrical surface, $(\mathbf{X}_i)_{ls+1}$, for the next iFEM analysis. Besides, the nonlinear deformations can be calculated correctly since the experimental section strains vary nonlinearly in case of large displacement event. If the incremental deformations are not large enough as compared to geometrical dimensions of the iQS4 model, they can be neglected for next steps. Accurate large deformation can still be monitored in this case due to the nonlinear input of experimental data. For further details of the incremental iFEM analysis, the reader can refer to the reference [50]. To facilitate the computer implementation, the flowchart and pseudocode of the iFEM-iQS4 approach have been scrutinized in Fig. 4-3 and Algorithm 1, respectively.

Algorithm 1 iFEM analysis for displacement reconstruction of non-linear deformations

- **procedure** iFEM SOLUTION
- Read nodal coordinates and elements connectivity data

for e = 1 to n_{el} **do**

- Compute $\mathbf{B}^{\chi}(\chi = e, \kappa, \gamma)$ matrix defined in Eqs. (13-15)
- Compute $\mathbf{f}^{e}$ and $\mathbf{k}^{e}$ matrix using Eqs. (25-26)
- Assemble $\mathbf{f}^{e}$ and $\mathbf{k}^{e}$ matrices for all inverse elements

end

- Read constraint boundary conditions
- Compute $\mathbf{F}_R$ and $\mathbf{K}_R$ reduced matrices using constraint conditions and obtain $\mathbf{U}_R$

for e = 1 to n_{el} **do**

- Compute the kinematic variables using element DOF vector
- Compute full-field strain components
- Compute full-field stress components

end

if the reconstructed results are far from the reference solution

- Update the geometry of the structure using Eq. (32) for each time step and repeat the process until the result matches the FEM solution

end

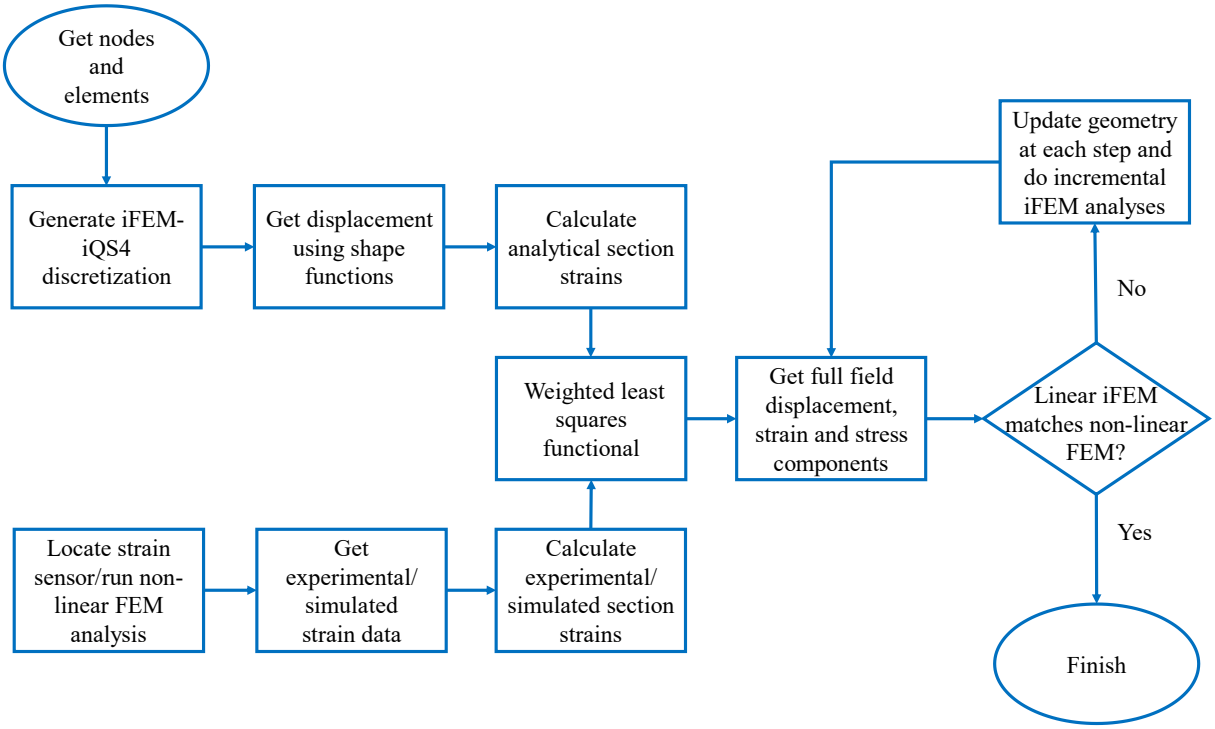

Fig. 4-3. Flowchart of iFEM solution for geometrically non-linear deformations.

4.2.2. The Role of Strain Pre-extrapolation Technique for iFEM Analysis

The experimental strain measurements are most likely noisy and erroneous, either due to operator error or poor equipment. In addition, due to the tendency to use a minimum number of sensors in real conditions, the number of sensors is optimally chosen, which can lead to discontinuity between strain data. To minimize this type of errors and to obtain a continuous distribution of experimental strains over the entire area of the plate, the experimental strain data can be processed using analytical techniques. Different types of smoothing techniques for stress and strain recovery and error estimating have been discussed in the literature [121]. Strain pre-extrapolation is one of those techniques which is based on data smoothing. To implement the proposed methodology for the experimental example, the number of sensors is kept constant while a high-resolution iFEM mesh is used to generate additional elements throughout the domain. A multinomial curve is then fitted through the available discrete experimental strain measurement points to replace the missing strain values with virtual strain data. The least squares method is a curve fitting technique which fits

polynomials through discretely determined strain data. The general form of a polynomial with *k*-th order takes the form:

$$\varepsilon(\xi) = \alpha_k \xi^k + \cdots + \alpha_2 \xi^2 + \alpha_1 \xi + \alpha_0 \tag{33}$$

where α_i $(i = 0,1,2,...,k)$ is the polynomial coefficient and the term *k* is the degree of the polynomial curve. The least-squares method minimizes the difference between the estimated values of the polynomial and the expected values from the data set. The coefficients of the polynomial regression model are determined by solving system of linear equations as follows:

$$\begin{bmatrix} n_P & \sum_{i=1}^{n_P} \xi_i & \cdots & \sum_{i=1}^{n_P} \xi_i^{\,k} \\ \sum_{i=1}^{n_P} \xi_i & \sum_{i=1}^{n_P} \xi_i^{\,2} & \cdots & \sum_{i=1}^{n_P} \xi_i^{\,k+1} \\ \vdots & \vdots & \ddots & \vdots \\ \sum_{i=1}^{n_P} \xi_i^{\,k} & \sum_{i=1}^{n_P} \xi_i^{\,k+1} & \cdots & \sum_{i=1}^{n_P} \xi_i^{\,2k} \end{bmatrix} \begin{Bmatrix} \alpha_0 \\ \alpha_0 \\ \vdots \\ \alpha_k \end{Bmatrix} = \begin{Bmatrix} \sum_{i=1}^{n_P} \varepsilon_i \\ \sum_{i=1}^{n_P} \xi_i \varepsilon_i \\ \vdots \\ \sum_{i=1}^{n_P} \xi_i^{\,k} \varepsilon_i \end{Bmatrix} \tag{34}$$

where n_P is the number of points to be regressed, and ε_i is the discrete strain data obtain during the experimental test from sensors. These set of equations can be represented in a general form of $\mathbf{H} = \boldsymbol{\alpha}\mathbf{Q}$ and the coefficients α_k can be determined as:

$$\alpha_k = \frac{\det(\mathbf{H}_i)}{\det(\mathbf{H})} \tag{35}$$

where the $\mathbf{H}_i$ is a new matrix with the *i*-th column replaced by the column vector $\mathbf{Q}$. An example of $\mathbf{H}_0$ matrix computation can be found in [18]. Solving these equations for different polynomial order, the best curve fit for the discrete experimental strain measurements can be obtained and accordingly the results of pre-extrapolated strains can be employed in iFEM-iQS4 analysis.

4.3. Numerical and Experimental Examples

In this section, the ability of the iFEM method to reconstruct the geometrically non-linear deformation of thin laminated plates and shell structures is thoroughly investigated

numerically and experimentally. The numerical problems involve flat and curved laminated panels subjected to increasing compressive load and exhibiting geometrically non-linear buckling and bending deformations. In the experimental case, a rectangular thin laminated plate is subjected to a line load that leads to deformation with a large deflection in the center of the plate. It should be noted that these case studies are carefully selected to demonstrate the inherent geometric application of the iFEM-iQS4 element for flat and curved thin laminated composite panels. As mentioned earlier, strain values have a critical role in iFEM shape sensing methodology. These required strain data are obtained for the numerical problems by performing non-linear FEM analysis utilizing ANSYS-APDL software [122]. However, these strain values are collected for the experimental case by using a network of strain gauges on the surface of the plate. To improve the accuracy of iFEM analyses with discrete in-situ strain data, a polynomial extrapolation strategy is used to smooth the discrete in-situ strain data. Finally, all the numerical and experimental results are verified using high-fidelity FEM analyses.

4.3.1 Post-buckling Analysis of a Flat Laminate: First Numerical Case Study

A carbon fiber reinforced polymer (CFRP) laminate with a square shape of 1 [m^2] area is considered as shown in Fig. 4-4. The stacking order of the laminate is $[\pm 30]_{3s}$, with a total of 12 layers symmetric about the midplane. Each layer has a thickness of 0.3 [mm], resulting in a total laminate thickness of 3.6 [mm]. The right edge of the plate is rigid, and a concentrated axial load of 60 [kN] is applied across this rigid end, thereby resulting in a uniform displacement in the negative x-direction, as depicted in Fig. 4-4. Since the load is applied so slowly that there are no dynamic effects within the structure, which is called quasistatic, the non-linear nature of the problem requires that the load be increased gradually. The initial load of 600 [N] is applied and then ramped to 60 [kN] with 17 incremental steps. Nonlinear analyses are performed using FEM software (i.e., ANSYS APDL). This software uses Newton-Raphson convergence criteria for nonlinear problems. The maximum number of equilibrium iterations is set to 1000 in ANSYS for each load increment to ensure a correct convergence and load-equilibrium analysis. The left edge of the laminated plate is fully clamped. However, only the transverse displacement w and bending rotation about the y-

axis θ_y are considered constrained for both top and bottom edges of the plate, as shown in Fig. 4-4. The mechanical properties of the CFRP material are listed in Table 4-1. This post-buckling analysis aims to evaluate the ability of the iFEM analyses to track the variations of the translational and rotational displacement at points A, B, and C as the load increases (the exact positions of points A, B, and C are depicted in Fig. 4-4). For this purpose, a non-linear FEM analysis is performed to simulate the required strain data as input to the iFEM analysis.

Table 4-1. Mechanical properties of the CFRP material

Lamina material	Young's modulus [GPa]	Poisson's ratio	Shear modulus [GPa]
Carbon-epoxy unidirectional composite	$E_1^{(k)} = 157.9$	$\nu_{12}^{(k)} = \nu_{13}^{(k)} = 0.32$	$G_{12}^{(k)} = G_{13}^{(k)} = 5.93$
	$E_2^{(k)} = E_3^{(k)} = 9.584$	$\nu_{23}^{(k)} = 0.49$	$G_{23}^{(k)} = 3.227$

The entire area of the plate is discretized into 100 sub-areas, as shown in Fig. 4-5. Three types of sensor placement models, namely 'Model I', 'Model II', and 'Model III' are used to perform the iFEM analyses at the same mesh resolution. In the arrangement of sensors for Model I, all inverse elements contain two strain measurement sets at the center of the element at two different interlaminar positions. These positions are chosen preferably through the thickness of the laminate (as mentioned in Section 4.2) with a total number of $2\times100=200$ strain rosettes. The sensor placement strategy of Model II uses $2\times40=80$ strain rosettes placed in the center of 40 elements. In the last sensor configuration (Model III), the total number of strain rosettes is reduced to $2\times16=32$ sensors, as shown in Fig. 4-5.

The weighting coefficients for elements owning sensors at the middle are assigned as $w_e = w_\kappa = 1$ and $w_\gamma = 10^{-7}$. However, for elements without sensors, these constants are set to $w_e = w_\kappa = w_\gamma = 10^{-4}$. It is worth noting that although thin plates undergo large deformations, but the strain values remain small, i.e., 1 to 10 micro strains. Therefore, when performing iFEM analyses, it is not practical to update the in-plane geometry and sensor positions with respect to each time step. However, the out-of-plane geometry (i.e., deflection) of the plate may need to be updated at each loading step. Since there is no significant

deflection between each time step, a linear iFEM analysis is preferred in the first numerical case compared to incremental linear iFEM analysis.

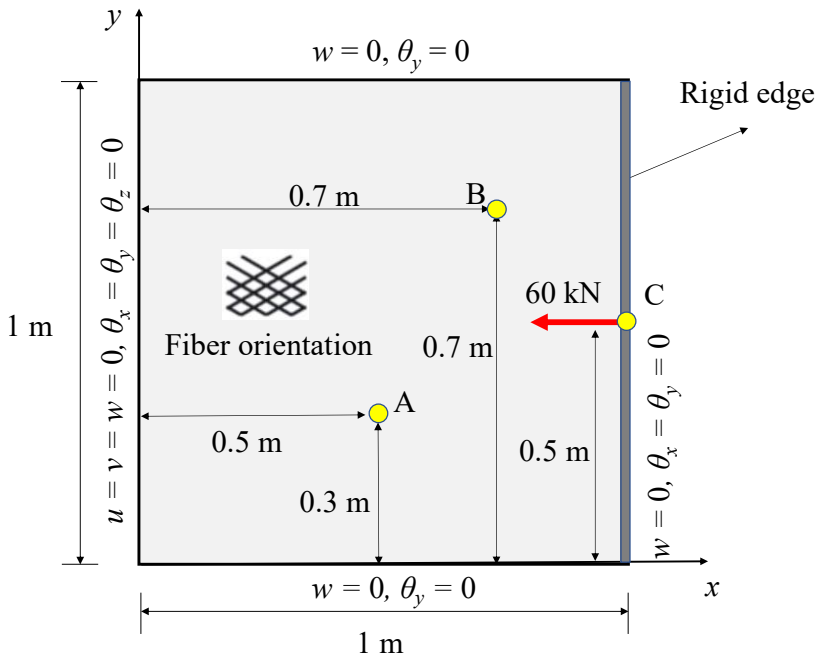

Fig. 4-4. Dimensions, fiber orientation, and boundary conditions of the laminated plate.

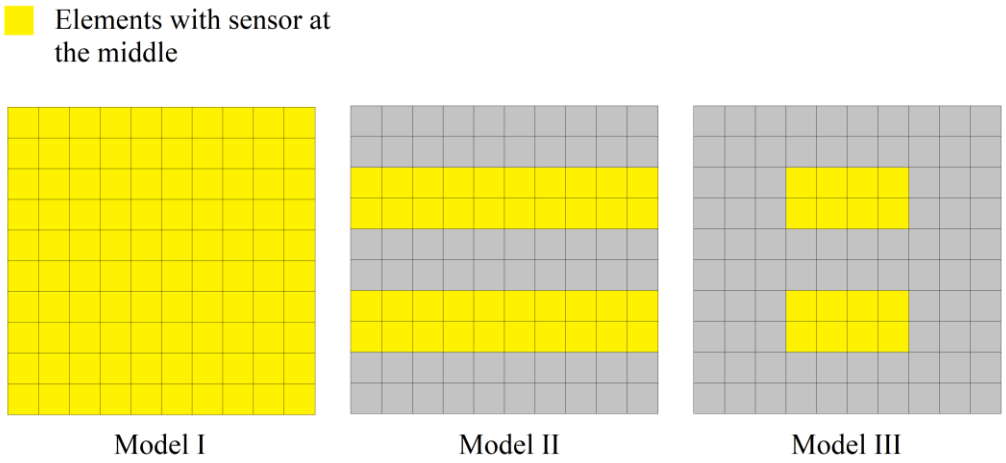

Fig. 4-5. Different sensor placement models of the plate.

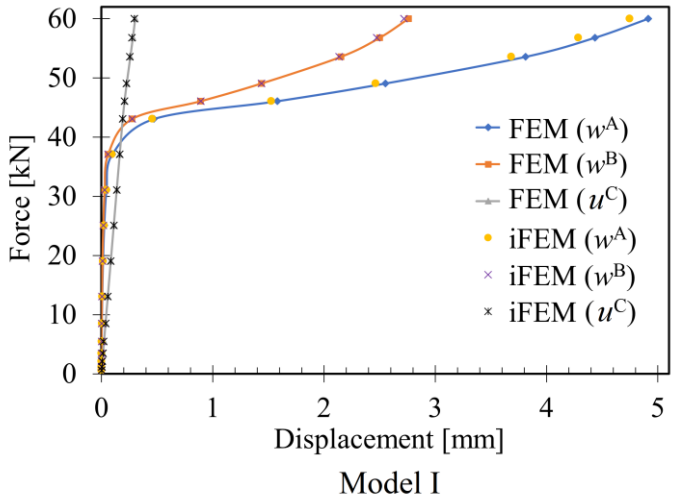

Model I

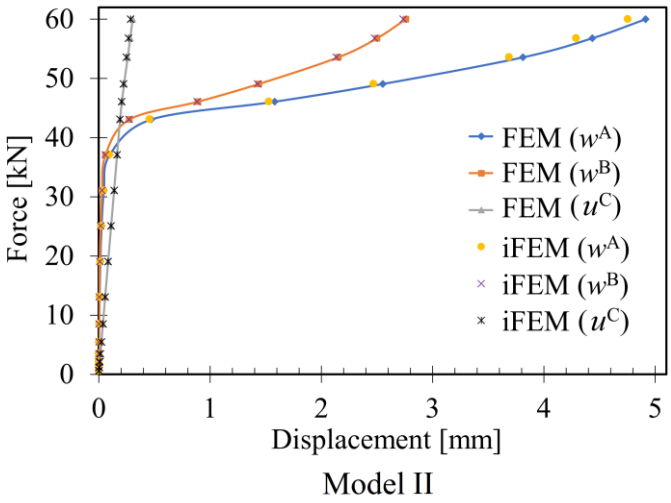

Model II

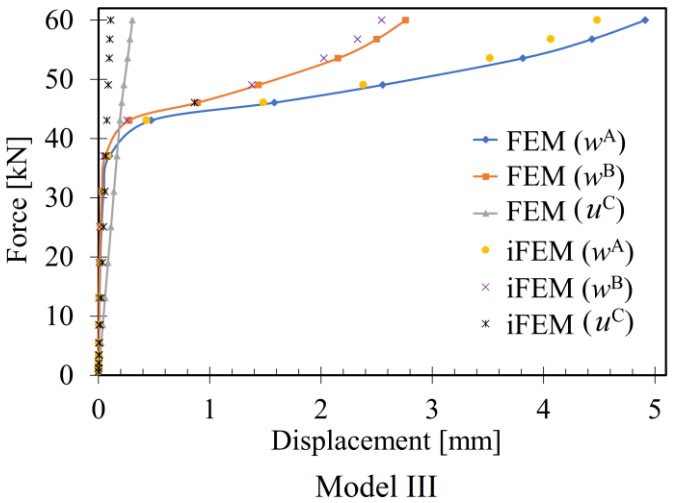

Model III

Fig. 4-6. Variation of transverse and axial displacement components at points A, B, and C.

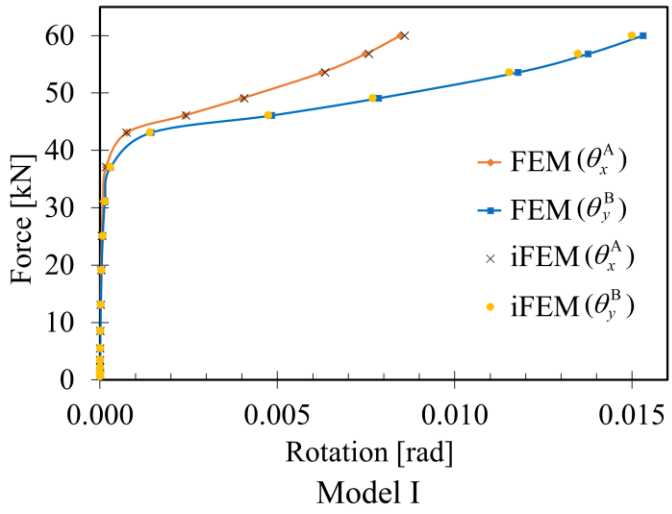

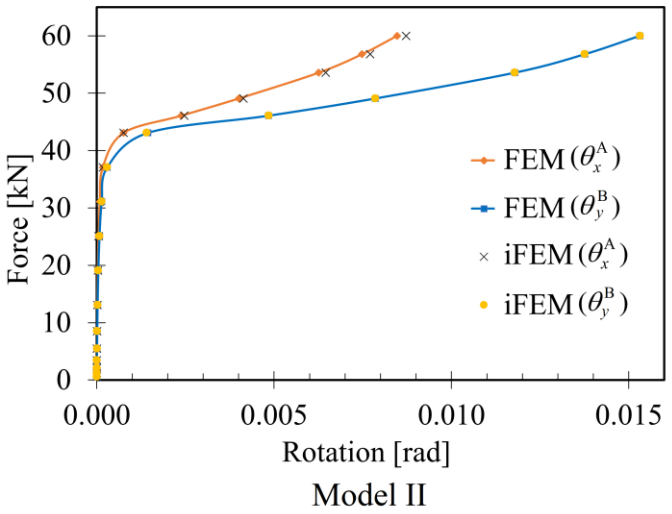

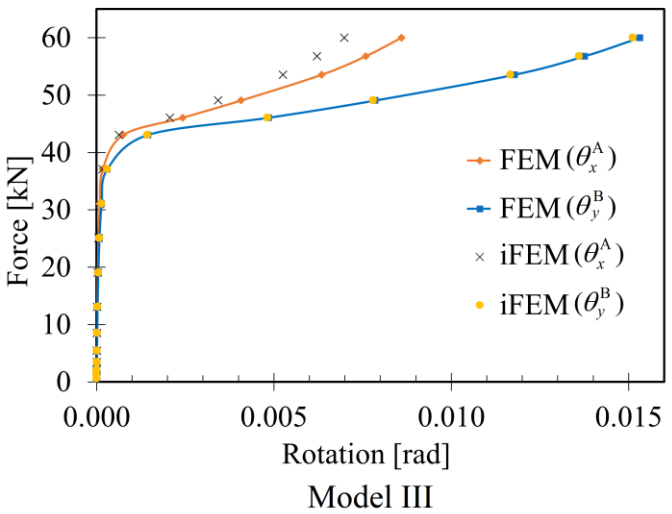

Fig. 4-7. Variation of rotational displacement components at points A, and B.

Fig. 4-6 shows the change in *z*-displacements *w* for points A and B, and the absolute value of *x*-displacement *u* at point C under incremental loading obtained by FEM and iFEM analysis using three types of sensor configuration. Moreover, the rotation variation about the *x*-axis θ_x for point A and the *y*-axis θ_y for point B is illustrated in Fig. 4-7. The force-displacement diagrams (Figs. 4-6, 4-7) exhibit that points A and B of the plate experience linearly transverse and rotational displacement almost up to 35 [kN] load level. After that, as the load increases, the plate experiences geometrically non-linear deformations up to 60 [kN]. However, point C experiences bilinear axial deformation throughout the loading history, as shown in Fig. 4-6. It can be observed from Figs. 4-6,4-7 that the iFEM can accurately capture the bilinear and non-linear behavior of the plate using Model I and Model II. However, regarding Model III, the iFEM results are slightly deviating from FEM results due to a smaller number of sensors, but it can still forecast the trend of FEM results.

The contour plots of obtained transverse and rotational displacements are compared between FEM and iFEM analyses with different sensor deployments are shown in Figs. 4-8, 4-9, 4-10. These figures show that the last time-step contour plots of transverse and rotational displacement of iFEM analyses are compared with the reference FEM solution. It can be seen from these figures that the iFEM results are quite similar to each other and almost indistinguishable from the FEM result. These contour results confirm the superior ability of the iFEM-iQS4 element to reconstruct post-buckling analyses of thin laminates.

To compare the quantitative results related to Figs. 4-8, 4-9, 4-10., a percent differences calculation is performed between maximum values of FEM and the iFEM analyses. In this regard, the percent differences between the reference solution and the iFEM analyses using sensor positions of Model I to III for the maximum transverse displacement are about 0.0%, 0.15%, and 5.4% in the given order. However, the same comparison for the maximum rotation about the *x*-axis between FEM and the iFEM analyses are 0.0%, 0.03%, and 1.1%, respectively. Finally, the comparison between the FEM and iFEM analyses for the maximum rotation about the *y*-axis are 0.45%, 2.5%, and 3%, respectively. This quantitative evaluation proves that iFEM is accurate enough to predict the maximum values of the translation and rotation field with only a small margin of error, even when only a few discrete sensor data are used.

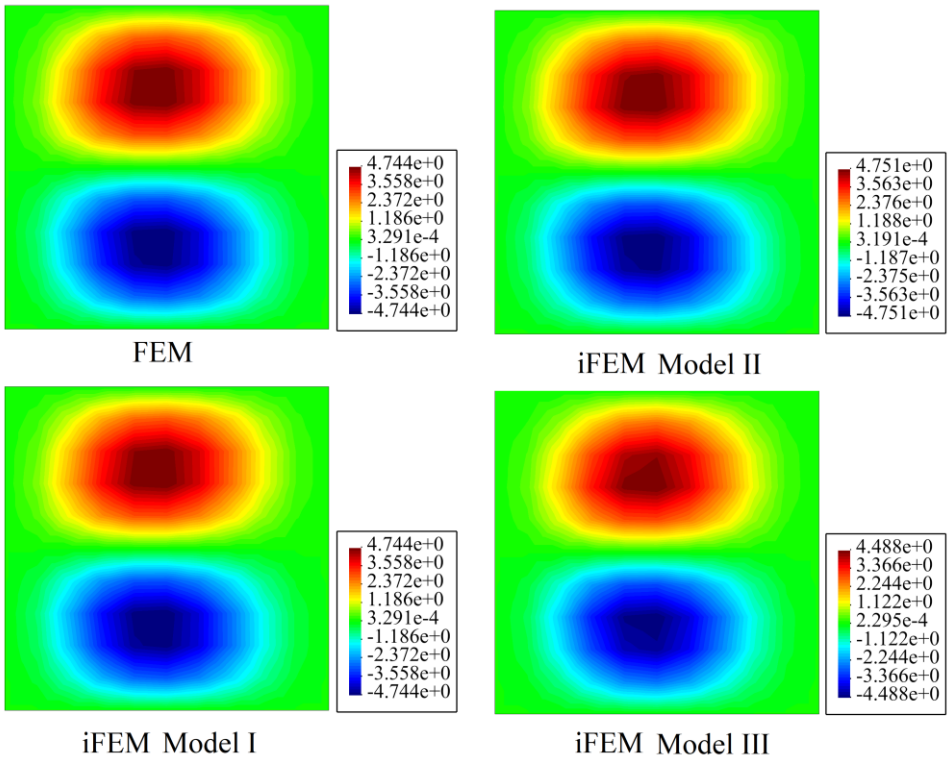

Fig. 4-8. Contours of transverse displacement *w* [mm] between FEM and iFEM analyses.

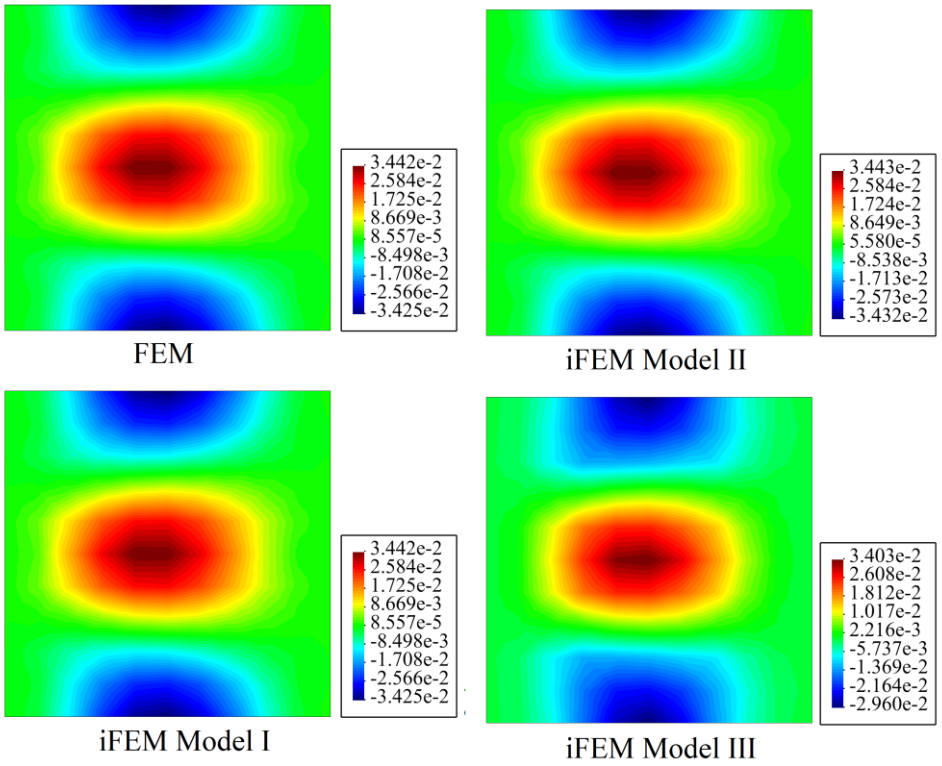

Fig. 4-9. Contours of rotation [rad] around *x*-axis between FEM and iFEM analyses.

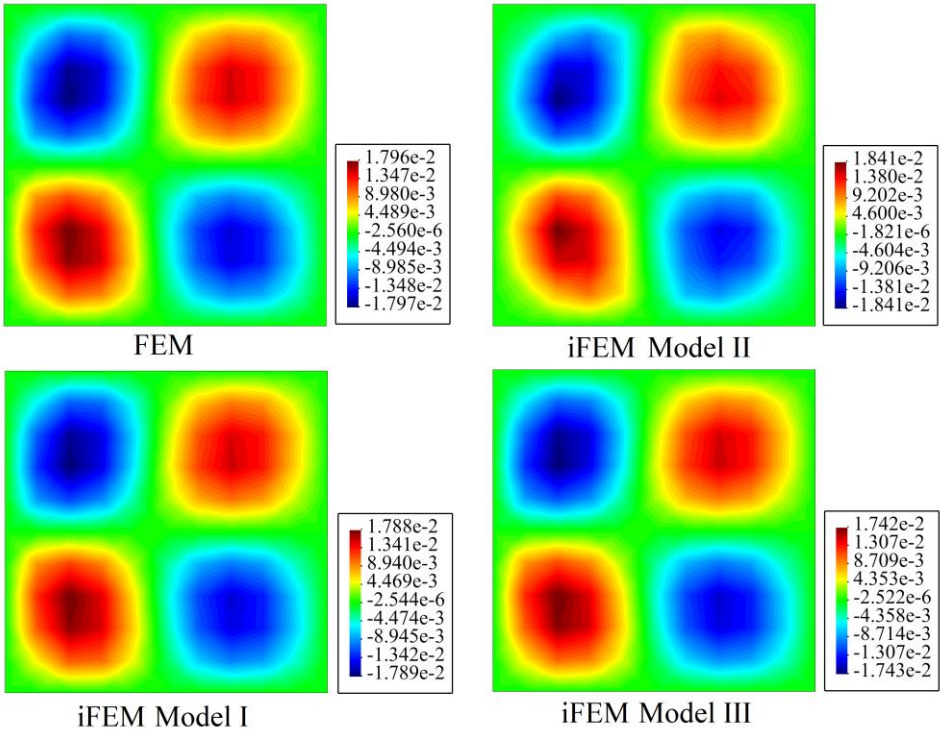

Fig. 4-10. Contours of rotation [rad] around *y*-axis between FEM and iFEM analyses.

4.3.2 Large Deflection of a Clamped Laminated Cylindrical Panel: Second Numerical Case Study

A deep cylindrical CFRP laminated plate under a point load with a stacking order of $(0/90/0/90)_s$ is evaluated by iFEM analyses. The geometry and boundary conditions are similar to a benchmark problem performed in some preliminary studies [123] with the following data: R = 500 [mm], L = 450 [mm], $\beta = 30^{\circ}$, h = 4 [mm] (refer to Fig. 4-11). The plate is subjected to gradually increasing concentrated loads of a maximum of 4 [kN] to achieve geometrically non-linear deflection. Like the previous example, three sensor positions are used to provide the required strain values for the iFEM formulation. Herein, the whole curved domain is divided into 144 sub-elements. For the first type of sensor distribution, indicated by the legend 'Model I,' all elements are instrumented using $2\times144=288$ strain sensors. The second model of sensor deployment is labelled as 'Model II', and the number of sensors is reduced to half ($2\times72=144$). However, for the third model of sensor distribution, 'Model III', the number of rosettes is reduced to one-sixth ($2\times24=48$) as shown in Fig. 4-12. The weighting constants for elements with sensors are set as

$w_e = w_\kappa = 1$, $w_\gamma = 10^{-6}$. However, for elements without sensors, they are assigned as $w_e = w_\kappa = w_\gamma = 10^{-3}$.

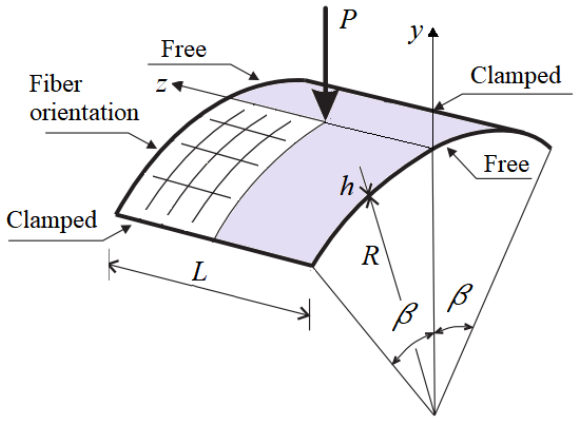

Fig. 4-11. Clamped laminated cylindrical panel under point load.

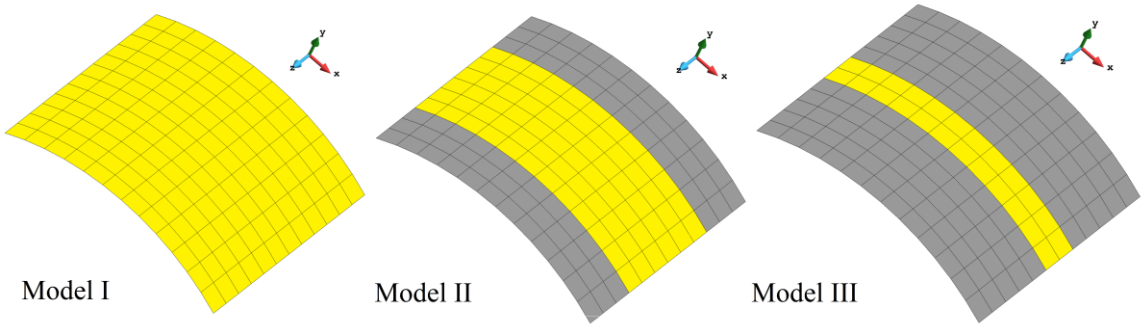

Fig. 4-12. Different types of sensor placement for cylindrical panel.

The capabilities of iFEM analyses in terms of shape sensing of curved laminates under point loads are evaluated. The central point of the laminate is subjected to a gradually increasing load of a maximum of 4 [kN]. The load is applied to the structure in ten increasing steps with equal intervals of 400 [N], as shown in Fig. 4-13. In this way, the central point of the plate is deflected as a function of incremental forces. Since the incremental strain values associated with the alternating time-steps are large enough to affect the deflection results of the iFEM analyses, the incremental linear iFEM formulation is applied at each loading step to reconstruct the current deformed shape. Then, the geometry is updated, and the iFEM analyses are performed based on the incremental strain data utilizing three types of sensor configurations (i.e., Models I to III).

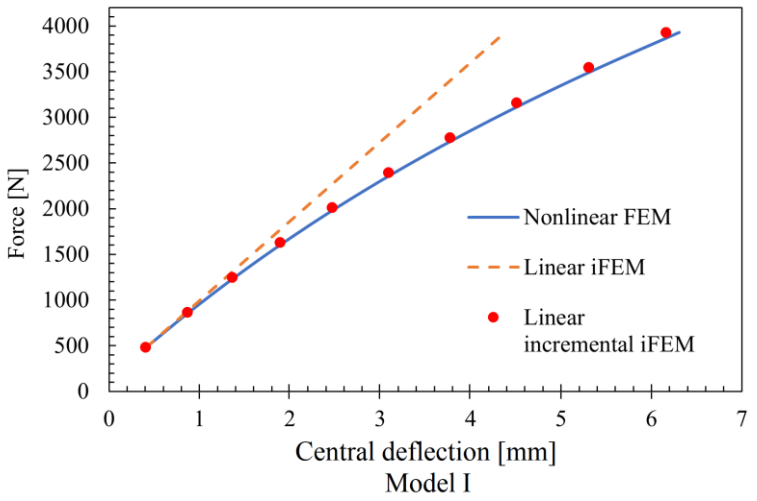

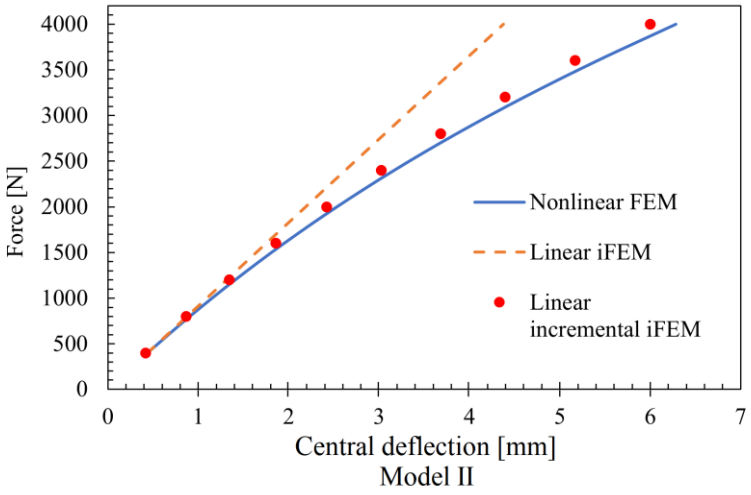

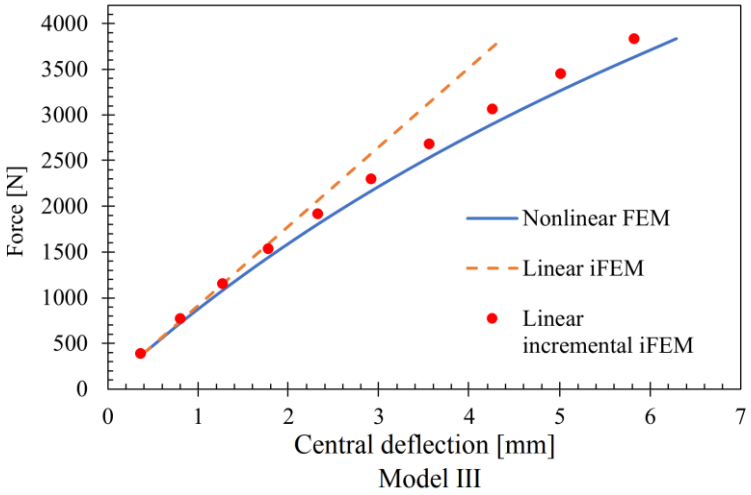

Fig. 4-13. Central deflection of the cylindrical laminate using three types of sensor placement.

Fig. 4-13 obviously shows that the deflection predicted by the linear incremental iFEM approach agrees quite well with the FEM solution when the first sensor model is used. It is also clear that as the number of strain gauges decreases, there is a discrepancy between the linear incremental iFEM and FEM results. However, these error margins are negligibly small, indicating that the incremental linear iFEM approach can capture well the geometrically non-linear deflection of a thin laminated shell structure. The linear iFEM results are calculated and compared with the FEM solution and are exhibited in Fig. 4-13. In the current case study, it can be observed that, unlike the previous numerical example, linear iFEM analyses cannot be a substitute for the shape sensing of curved laminates.

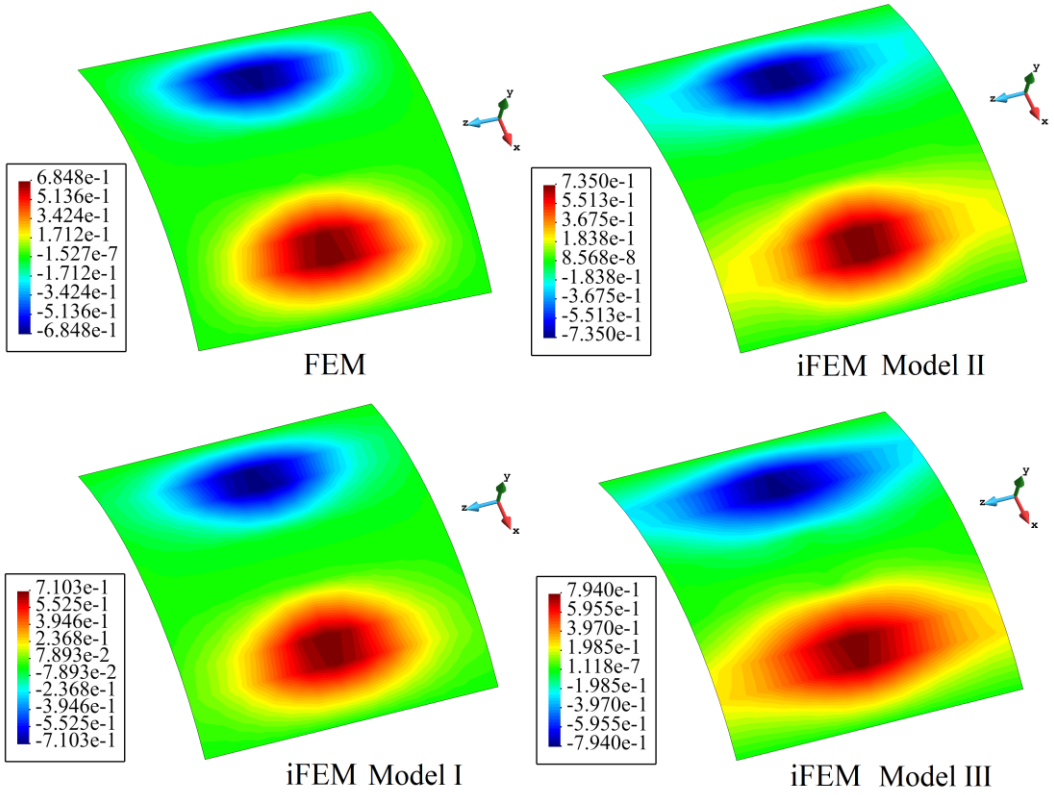

Fig. 4-14. Contours of *x*-displacement [mm] component obtained by iFEM and FEM analyses.

Additionally, the ability of the incremental iFEM approach to reconstruct the axial and rotational displacements of the last time-step using the Model I, Model II, and Model III sensor configurations are illustrated in Figs. 4-14, 4-15, and 4-16. These axial and rotational displacement contours show that the iFEM analysis with the sensor distribution of Model I reconstructs quite similar contours to the reference FEM solution. Moreover, the obtained

contours of the iFEM analyses with the Models II and III sensor configuration are less accurate but still comparable to FEM solutions. It should be noted that although the use of a smaller number of sensors leads to a minor contour inconsistency compared to the reference solution, it predicts the precise location of the occurrence of the maximum displacement, which fulfills the most crucial requirement of a reliable shape sensing system.

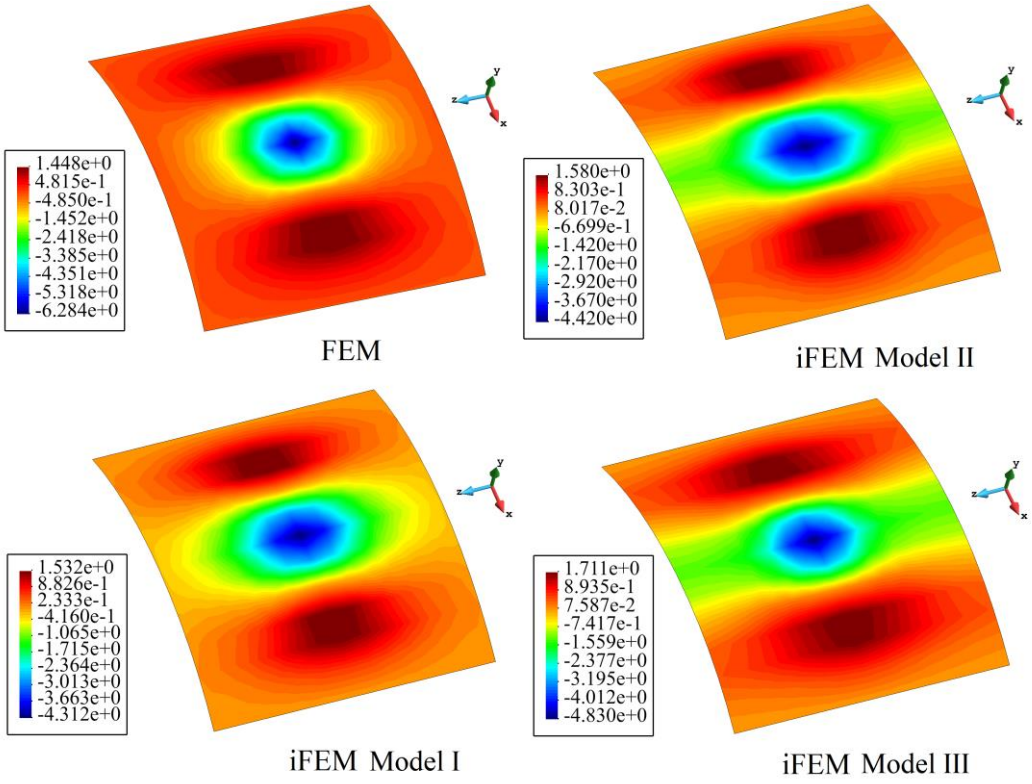

Fig. 4-15. Contours of *y*-displacement [mm] component obtained by iFEM and FEM analyses.

Quantitatively speaking, the percent differences for the maximum x and y displacements between the FEM reference and the iFEM analyses are calculated as (3.7%, 7.3%, 16%) and (5.8%, 9.1%, 18%), respectively, for the Models (I, II, III). However, when a similar comparison is made between FEM and iFEM analyses for the case of rotation θ_z (around global *z*-axis), these margins of error are reduced to 0.04%, 0.9%, and 0.91% in the given order. These values for the percent difference show the superior performance of the iFEM approach at a higher sensor density, especially at the maximum rotational displacement. Although the values for the percent difference increase at lower sensor densities, these error percentages are not significant enough to affect the reconstruction

performance of the iFEM method. Overall, based on the obtained quantitative and qualitative results, it can be declared that the iFEM-iQS4 element is efficient enough to reconstruct the non-linear deformations as well as the axial and rotational contours with only a few sensors. These two numerical investigations clearly illustrate that using iFEM analyses for shape sensing of thin laminated plates and shells leads to reliable and cost-effective results.

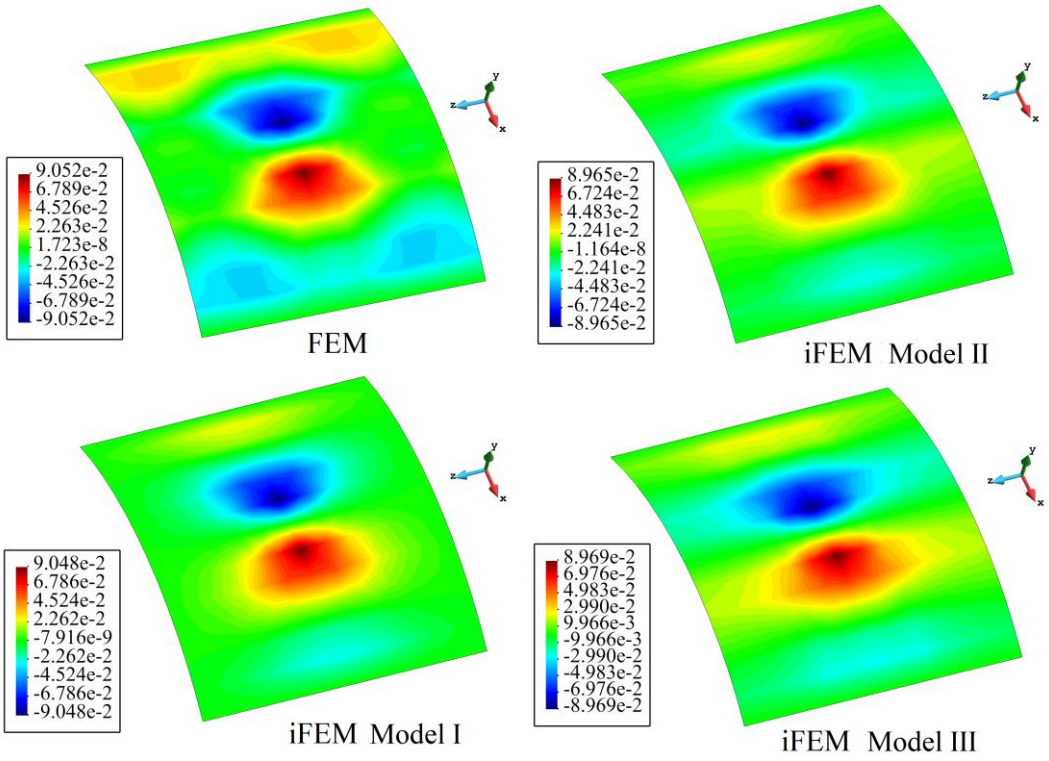

Fig. 4-16. Contours of rotation [rad] around *z*-axis obtained by iFEM and FEM analyses.

4.3.3 Large Deflection Sensing of a Clamped Laminated Flat Panel: Experimental Case Study

4.3.3.1 Laminate manufacturing and testing

E-glass fiberglass woven roving fabric with an areal weight of 300 g/m^2 and Biresin CR120 resin and CH120 hardener were procured from Metyx-Turkey and Sika for fabrication, respectively. The vacuum-assisted resin infusion process is used to fabricate the composite sheet with a uniform thickness of almost 0.83 [mm]. For the resin infusion, a flat

stainless-steel surface of the table was prepared by applying coats of sealant and release films. Four layers of fibers were placed on the prepared surface and covered with a peel ply and then flow-mesh, which helps prevent the air entrapment and assists the uniform resin flow. A vacuum bag was sealed with the help of sealant tape, and then a debulking process was carried out for 30 minutes. Resin and hardener were mixed in a ratio of 100:30 wt% and then degassed for 20 minutes to remove entrapped air. After degassing, epoxy was injected into the system, and a temperature of 120ºC was applied through Wittmann Tempro plus D-18 for 24 hours. The samples from the composite plate were machined by a Kuka KR16 Ultra-F-robot water jet to characterize the material properties.

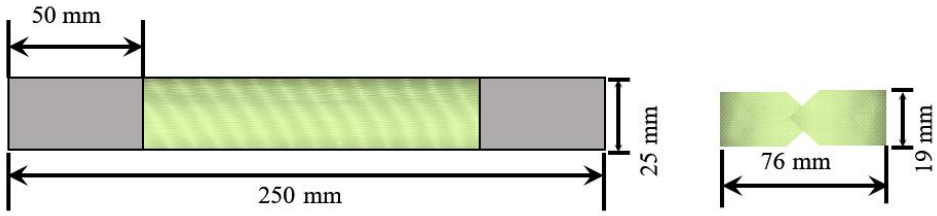

Fig. 4-17. The schematics of tensile and shear test specimens.

Table 4-2. Mechanical properties of the Glass-Epoxy material

Lamina material	Young's modulus [GPa]	Poisson's ratio	Shear modulus [GPa]
Glass-epoxy twill composite	$E_1^{(k)} = E_2^{(k)} = 24$ $E_3^{(k)} = 7.1$	$\nu_{12}^{(k)} = \nu_{13}^{(k)} = \nu_{23}^{(k)} = 0.14$	$G_{12}^{(k)} = G_{13}^{(k)} = G_{23}^{(k)} = 3.1$

Tensile test was performed according to ASTM D-3039 standard to determine the elastic modulus and Poisson's ratio, whereas Iosipescu shear test was performed as per ASTM D5379 to measure the shear modulus. For the tensile test, six specimens with a size of 250×25 [mm^2] were cut and tabbed with 50 [mm] aluminum, while for the shear test, five specimens with a size of 76×19 [mm^2] were tested. Both shear and tensile tests were performed with the help of the Instron universal testing machine (UTM) 5982, which is equipped with a 100 [kN] load cell. Fig. 4-17 depicts the schematic of tensile and V-notch shear test specimens. The obtained mechanical properties of the glass-epoxy material are listed in Table 4-2. It is noteworthy that a bending test cannot determine the out-of-plane material properties because

the plate is not thick enough. Therefore, these material properties are approximated and calibrated using the FEM analysis.

3.3.2 Large deformation test setup

For the large deformation test setup, sixteen Type I C2A-06 125ww-350 strain gauges with quarter bridges are used to measure the strain. These strain gauges have a grid resistance of 350 ± 0.6% [Ohms] and are stacked as 0º-45 º-90 º rosette, recommended for steep strain gradient and limited gaging areas. These strain gauges are attached to the bottom of the 1200×300 [mm^2] composite laminate. The laminate is fixed in a metal fixture, and a compression line load is applied along the length of the laminate (refer to Fig. 4-19). The geometry, boundary conditions, and sensor positions of the clamped flat plate are shown in Fig. 4-18. The whole area of the plate is discretized into several elements. Some of these elements have sensors at their centers marked with yellow color as seen in Fig. 4-18. The exact location of these sensors is shown in Table 4-3.

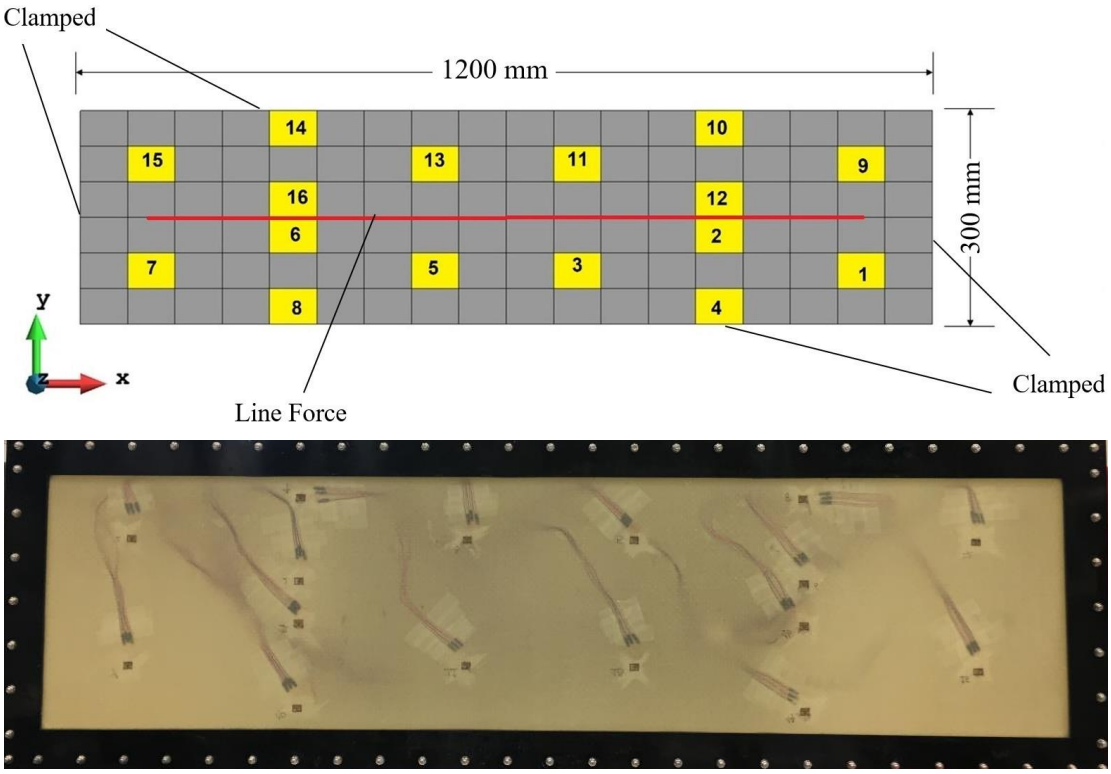

Experimental Sensor Placement on the Composite Plate

Fig. 4-18. The geometry, boundary conditions and sensor positions of the flat plate under line load.

Table 4-3. Coordinates of sensors on experimental laminated plate

Sensor	x [mm]	y [mm]	Sensor	x [mm]	y [mm]
1	1100	75	9	1100	225
2	900	125	10	900	275
3	700	75	11	700	225
4	900	25	12	900	175
5	500	75	13	500	225
6	300	125	14	300	275
7	100	75	15	100	225
8	300	25	16	300	175

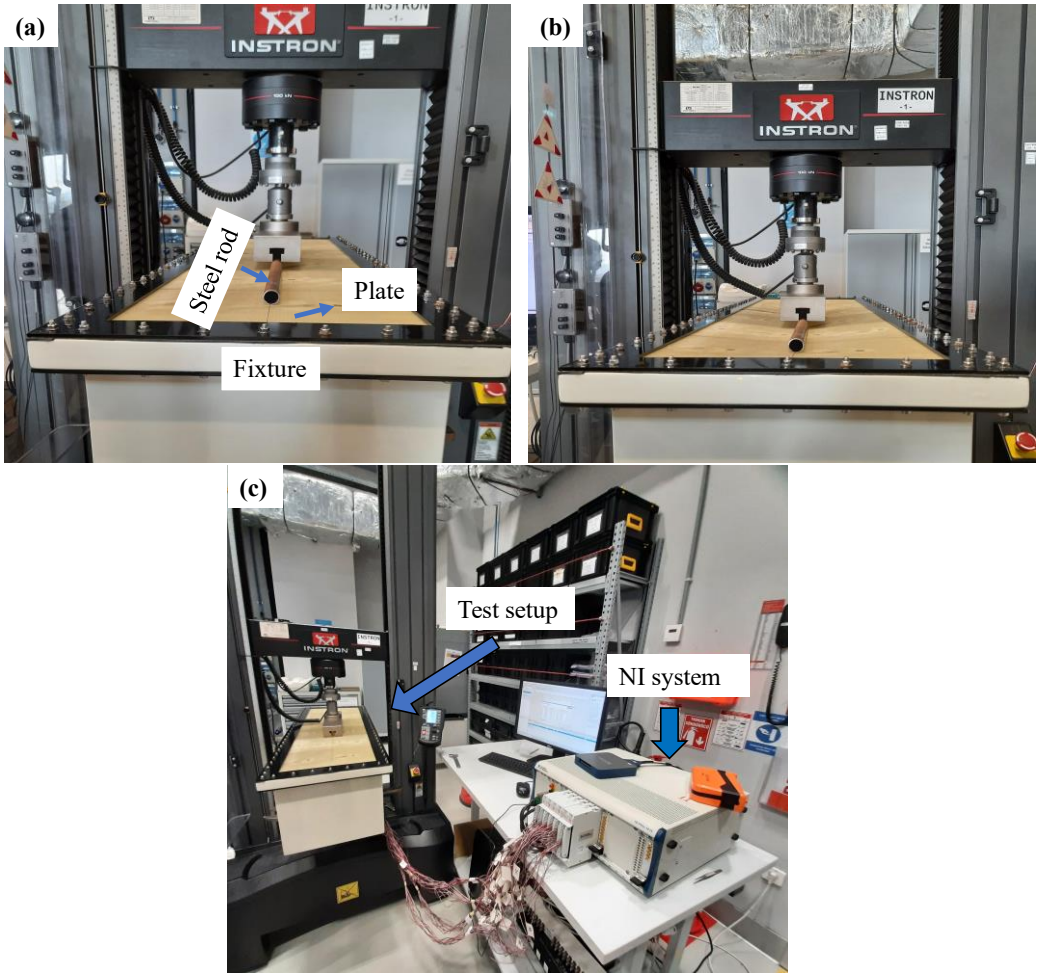

Fig. 4-19. Test setup a) before loading, b) after loading, c) data acquisition system.

Strain data is acquired using the NI PXIe-1075 chassis via the NI 6363 strain card, using the NI signal express software to record the continuous data. To achieve a homogeneous distribution of strains, a preload of 100 [N] is applied to the surface of the plate via a steel bar. At a preload of 100 [N], the strain gauges are calibrated to use the zero value

as a reference. A continuous ramp load of 100 [N] to 750 [N] with a hold time of 10 seconds between each ramp is applied to the plate within an interval of 250 seconds, as shown in Fig. 4-20. Strain data are post-processed using NI- DIAdem 2021 software, where strain data for each 10-second hold step (13 in total) from each strain gauge are averaged and then used for iFEM calculations. As shown in Fig. 4-18, the arrangement of the sensors and the applied boundary condition are symmetrical, which also results in symmetrical strain data. Therefore, one set of strain gauges (1 to 4) can represent the strain distribution across the whole laminate. Fig. 4-21 shows the non-linear variation of axial strains of these sensors (1 to 4) over the time-steps.

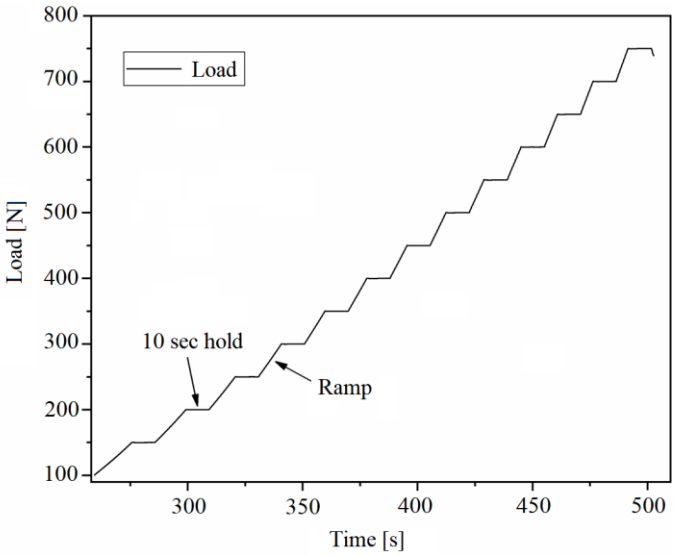

Fig. 4-20. Time-loading history.

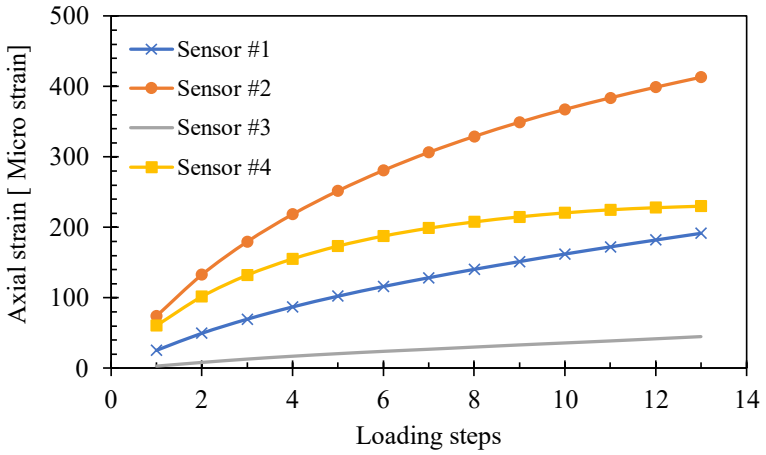

Fig. 4-21. The variation of axial strains of sensors number 1 to 4 over the time steps.

4.3.3.3 iFEM-based Shape Sensing

This section presents real-time shape sensing for the clamped laminated plate by performing iFEM analyses. As described in the previous sections, a prior smoothing analysis is performed over the obtained experimental strain data. For this purpose, a moderately fine resolution of the iFEM discretization is used with discrete strain data obtained through strain gauges, as shown in Fig. 4-22(a). After that, the missing strain values of the empty elements are predicted by performing a strain pre-extrapolation technique to fit a fourth-order polynomial curve through discrete strain values aligned along the *x*-axis as shown in Fig. 4-22(b). Thus, the number of available strain data is increased from sixteen to forty-four, and this extensive strain data is used in the iFEM formulation. The iFEM analyses are then performed for all incremental loading steps to reconstruct the non-linear large deflection of the entire laminate. The weighting values for the elements accommodated with sensors are set as $w_e = w_\kappa = 1$ and $w_\gamma = 10^{-6}$. However, these constants are assigned as $w_e = w_\kappa = w_\gamma = 10^{-5}$ for elements without sensors (strain-less elements). Finally, a high-fidelity FEM analysis with 14701 nodes and 88206 DOFs is performed to serve as a reference solution to compare with the iFEM results as illustrated in Fig. 22(c).

The central deflection (maximum displacement) of the laminate for all loading levels obtained by experiment, FEM, iFEM using discrete strain data, and iFEM coupled with the pre-extrapolation technique are shown in Fig. 23. This figure shows that the iFEM (pre-extrapolated strain data), experimental results and FEM analyses have a higher degree of agreement compared to iFEM (discrete strain data), thereby proving the advantage of the strain extrapolation before running an iFEM analysis. In other words, the use of polynomial smoothing analyses for iFEM analysis results in almost identical nonlinear deflection predictions to the experimental deflections and reference FEM solutions, whereas iFEM analysis with discrete strains underestimates the maximum deflections as shown in Fig. 23. This behaviour is even more apparent at the higher loading levels (after load step of 6). For smaller loads (before load step 6), both iFEM approaches produce more erroneous deformations due to the fully clamped constrained boundary condition of the plate and absence of enough sensors near the clamped edges as can be observed from Figs. 22a-b.

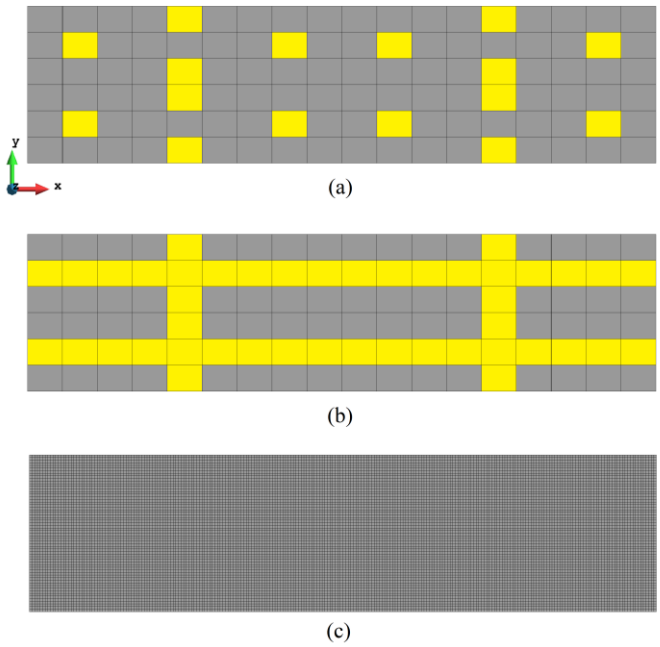

Fig. 4-22. Mesh resolution and iQS4 elements with strain measurement sets at the center for a) iFEM analysis using discrete sensors, b) iFEM analyses using polynomial smoothing approach, and c) FEM model.

This means that in the lower loading stages, the strains dominate at the edges of the laminates whereas, at higher load levels, these strain magnitudes become smaller as compared to the strains at the centre of the plate, thereby allowing a better deformation reconstruction after load step of 6. In sum, since the edge lines of the plate do not have enough sensors to detect these experimental strains, the iFEM-reconstructed displacements at low loading levels become less accurate than that of the higher loading stages.

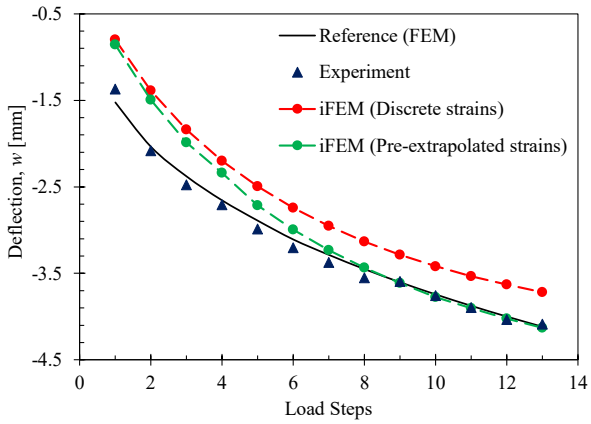

Fig. 4-23. Central deflection of the plate obtained from experimental, FEM and iFEM analyses.

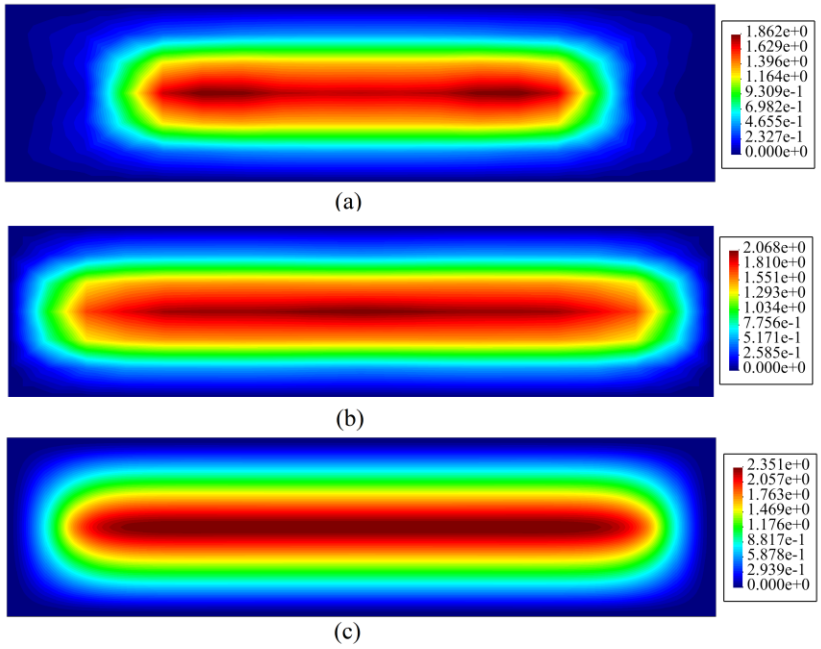

Fig. 4-24. Total displacement contours at time-step 3 obtained by (a) iFEM analysis using discrete sensors, (b) iFEM analysis using polynomial smoothing approach, and (c) FEM analysis.

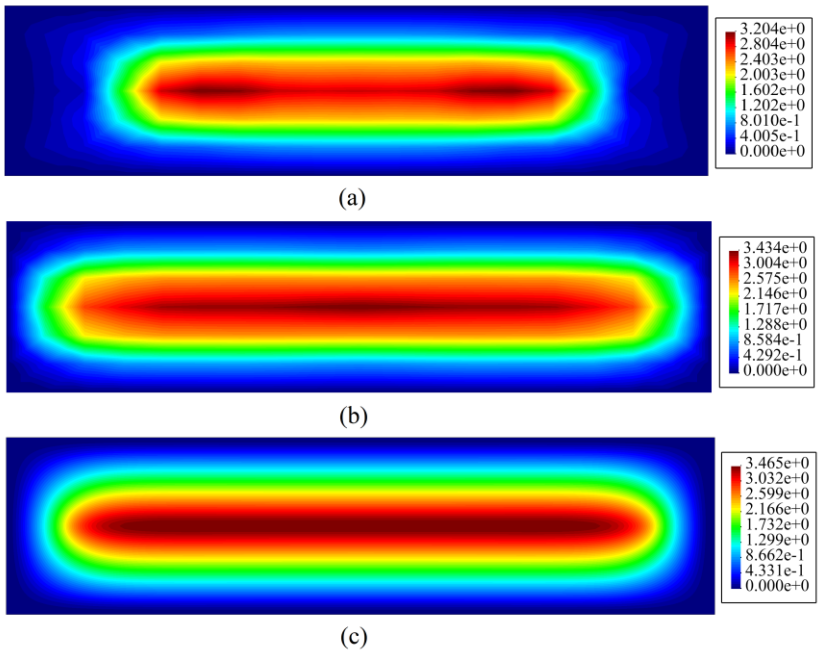

Fig. 4-25. Total displacement contours at time-step 8 obtained by (a) iFEM analysis using discrete sensors, (b) iFEM analysis using polynomial smoothing approach, and (c) FEM analysis.

Figs. 4-24, 4-25, and 4-26 illustrate full-field deflection of the plate obtained with iFEM using discrete and pre-extrapolated strains and FEM analyses for three arbitrarily selected

time loading levels (i.e., steps 3, 8, and 13). As can be seen in these figures, the total displacement contours obtained using iFEM in conjunction with a polynomial smoothing approach are comparable to the reference FEM, which also confirms the high performance of the iFEM method for full-field reconstruction in real-time. However, the iFEM analyses with discrete strains show lower accuracy in reconstructing the full-field displacement contours. In terms of numbers, the maximum values of the total displacement between FEM and the iFEM analyses using the strain pre-extrapolated technique are 12%, 0.9%, and 0.3% for steps 3, 8, and 13, respectively. However, the percentage errors between FEM and the iFEM analyses using discrete strain data are 21%, 7.5%, and 7% in the given order, confirming the higher accuracy and efficiency of the iFEM analyses using the pre-extrapolated strain data.

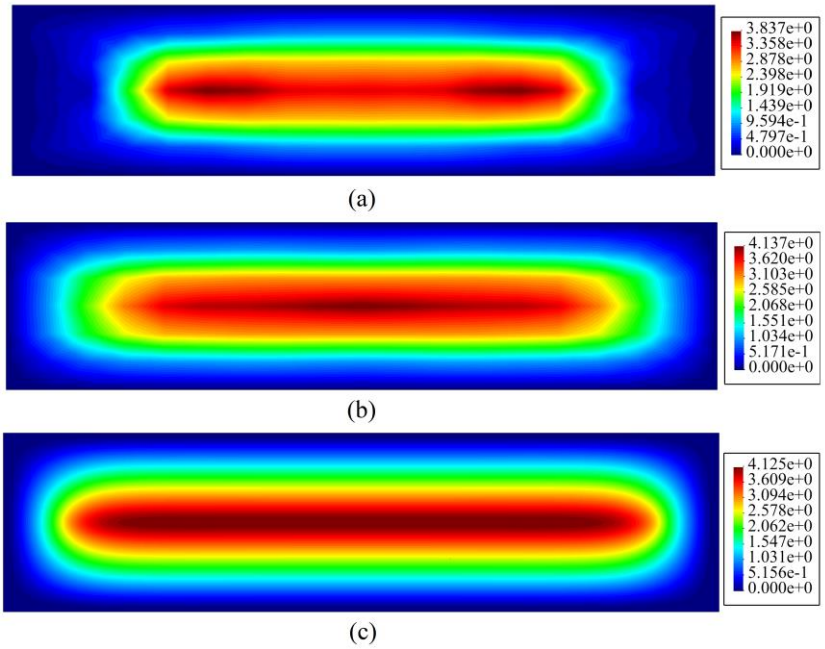

Fig. 4-26. Total displacement contours at time-step 13 obtained by (a) iFEM analysis using discrete sensors, (b) iFEM analysis using polynomial smoothing approach, and (c) FEM analysis.

Finally, the three-dimensional deformed shapes reconstructed utilizing the iQS4 models of the iFEM (discrete and pre-extrapolated strains) are compared with each other and reference solutions in Fig. 4-27. According to these deformed shapes, the improved performance of iFEM-iQS4 with pre-extrapolated strains can be observed for full-field large deformation sensing, thus proving the experimental advantages of the proposed method.

Overall, this study case experimentally verifies the ability of the iFEM-iQS4 inverse element to capture the geometrically non-linear deflection of thin laminates and validates the practical utility of the strain pre-extrapolation technique for the iFEM-FSDT approach. The computational strategy presented here can be used to develop accurate and efficient applications of the iFEM-FSDT method in future research on shape detection of thin laminated structures subjected to large deformations using a small number of discrete sensors.

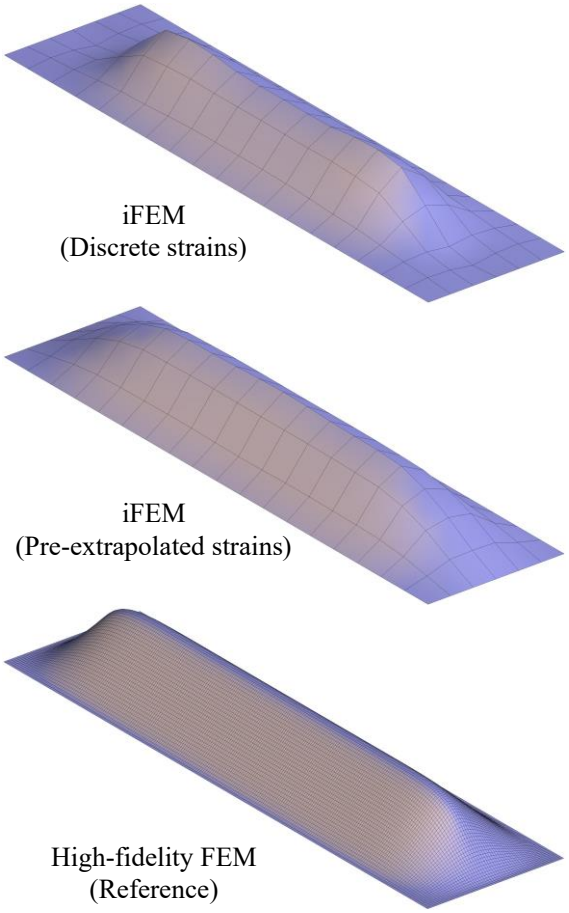

Fig. 4-27. Comparison of three-dimensional deformed shapes (30 times magnified) obtained at time-step 13.

4.4. Conclusions

This study presents an experimental and numerical evaluation for shape sensing of thin laminated structures subjected to large deformations using the iFEM approach. The iFEM is a sensor-based algorithm that uses a weighted least squares function to minimize the error between experimental and numerical section strains to predict full-field deformations. To this

end, the entire domain of the structure is discretized into quadrilateral inverse shell elements, referred to as the iFEM-iQS4 model. For the numerical verification of the iFEM approach for geometrically non-linear displacement monitoring of thin laminated structures, two case studies are considered, including a post-buckling analysis of a thin laminated plate and a curved thin laminated shell geometry subjected to large deformations. For this purpose, three different sensor placement models are used for these laminates.

Furthermore, the efficiency of the iFEM-iQS4 element is verified through experiments where initially a thin laminate is fabricated, and then the mechanical properties of the laminate are measured through tensile and shear tests. Moreover, this thin laminate is clamped on a fixture and then tested under large deflection deformation. The appropriate locations for installing sixteen strain rosettes are calculated to obtain the required strain data for the iFEM analysis. Then, these sensors are placed at the designated locations on the surface of the plate, and the strain data is collected using data acquisition systems. Since the sensors are discretely distributed from each other, the iFEM formulation is coupled with a strain data smoothing technique known as the “strain pre-extrapolation technique” to recover these sparse strain data over the entire area of the structure. This smoothing method also helps to neglect strain measurement errors and other operational mistakes during the analyses.

The obtained quantitative and qualitative results of the post-buckling analysis clearly show the high performance and accuracy of iFEM in buckling deformation reconstruction of thin laminates even by employing a few sensors. Moreover, the incremental iFEM analyses obtained for the curved shell laminate show a good agreement with the reference FEM solution by using sparse sensor deployments. In the experimental analyses, the efficiency of the coupled iFEM method with the pre-extrapolated strain technique is well demonstrated in recovering discrete strain data over the entire domain of the structure. This smoothed strain data leads to almost excellent reconstruction of the displacement field of the thin laminates subjected to large deformation. In conclusion, the knowledge acquired from this study can be utilized as a practical guideline for future applications of the iFEM-iQS4 algorithm for displacement monitoring of thin laminated structural components subjected to geometrically non-linear deformations.

CHAPTER 5. Numerical Applications of Inverse Finite Element Method for Shape Sensing of Marine and Aerospace Structural Components

Marine and aerospace structural components are usually exposed to harsh environmental conditions which can lead to damage/failure of the structure. Therefore, the implementation of a reliable Structural Health Monitoring (SHM) system is crucial to reduce the economic cost and improve the predictive maintenance plan. As an important part of SHM, shape sensing reconstructs the displacement field using in-situ strain sensors. The inverse finite element method (iFEM) is a powerful technique for tracking the static and dynamic response of structural components in three dimensions in real time. For this purpose, iFEM uses strain data collected from a discrete number of on-board/embedded sensors. The main objective of this chapter is to monitor the deformation of a ship hull structure and a doubly curved aft fuselage panel under representative loads using the iFEM method. A robust inverse shell element, called iQS4, is used to estimate the iFEM capability in three-dimensional shape sensing with only a number of sensors on board. A direct Finite Element Analysis (FEM) is performed to simulate the strain information required for the iFEM analysis. The obtained reference results are compared with the iFEM analysis to prove the efficiency and accuracy of the iFEM method in predicting the full-field deformation of such structural components with only a few sensor paths. In addition, the accuracy of iFEM approach is also assessed for broken/damaged sensors among other sensors.

5.1. Introduction

Stiffened panels are widely used to build structural elements of aerospace and marine structures. One of the most common types of those panels are aft fuselage structures in aerospace engineering and ship-hull structure in marine engineering. However, the harsh environmental conditions may sometimes cause damage in them which may lead to catastrophic failure of the overall structure. To detect such probable flaws in composite structures, a suitable structural health monitoring (SHM) system is necessary to be installed onboard structure. Reconstructing the displacement field from in-situ sensors in real-time is referred to as “shape sensing”, which is an important part of the SHM process. The inverse finite element method (iFEM) is a powerful shape-sensing technique, introduced by Tessler and Spangler [14,15], which can be potentially useful for SHM of plate/shell structures. The

iFEM methodology performs the shape sensing by minimizing a weighted-least-squares functional that aims to match the experimental strain measurements with their theoretical counterparts. The minimization process leads to a system of linear algebraic equations that can be solved to determine the unknown displacements in real-time. Once the displacement field is reconstructed, the strains throughout the field can be calculated using the strain-displacements relationships based on iFEM. Then, the three-dimensional stress state of the structure can be calculated using the full-field strains and the material properties of the structure. Finally, the three-dimensional stresses can be fitted to an equivalent stress using an appropriate failure criterion (e.g., von Mises yield criterion), allowing real-time damage predictions. The applications of iFEM to damage detection and SHM of metal and composite structures have been recently carried out [58,59,116,124].

In addition to damage detection based on iFEM, several robust inverse elements have been developed for shape sensing beam/plate/shell-like structural components based on iFEM formulations [35,44,45]. Abdollahzadeh, Kefal, and Yildiz [16] provided a comparison study among existing inverse shell elements (i.e., iMIN3, iQS4, and iCS8). The iQS4 element is a four-node quadrilateral inverse-shell element which firstly introduced by Kefal et al. [43]. The kinematic relations of the iFEM-iQS4 formulation are based upon Mindlin's plate theory [125]. The iFEM analyses have been widely used to shape and stress monitoring of different engineering applications with different geometrical topologies and types of materials [18,19,126]. Moreover, coupled refined zigzag theory with iFEM approach is developed and introduced to better study the shape and stress monitoring of thick multilayered structures [17,40,57,86,87]. Coupled iFEM with isogeometric and peridynamics analyses can also be found in the literature [116,82].

To the best of the authors' knowledge, there is no research has been dedicated to verifying the capability of iFEM for shape sensing of aft fuselages and representative ship-hull structures in the literature. The problem mentioned above is addressed in the current study through performing various numerical shape-sensing analyses on a doubly curved composite panel as an aft fuselage and a stiffened representative ship-hull structure by utilizing the iFEM-iQS4 methodology. The iFEM-iQS4 element requires less computational effort than the other robust curved inverse shell element called iFEM-iCS8. Therefore, to

achieve fast real-time response, we used the iQS4 element. To this end, a high-fidelity FEM analysis is performed using ANSYS-APDL to provide simulated strain data (that can be considered as a representative of experimental sensor data) as well as to be a reliable reference solution to be compared with iFEM results. The obtained full-field displacement and strain contours demonstrate a high consistency between iFEM and FEM solutions. The obtained results also prove that iFEM can reliably predict full-field displacements of such structures with complex geometries by using sparse strain data collected from few numbers of sensors onboard. In addition, the efficiency and accuracy of iFEM approach are also assessed for broken/damaged sensors among other sensors. It is shown that in the case of loss of a few sensors, iFEM still can provide a reliable 3D shape reconstruction.

5.2. Mathematical formulation

iQS4 is a four-node quadrilateral inverse plate/shell element with six degrees of freedom (DOF) per node as shown in Fig. 5-1(a). The main advantage of using iQS4 is the inclusion of the drilling rotations which enables superior shape-sensing of different applications with complex geometries.

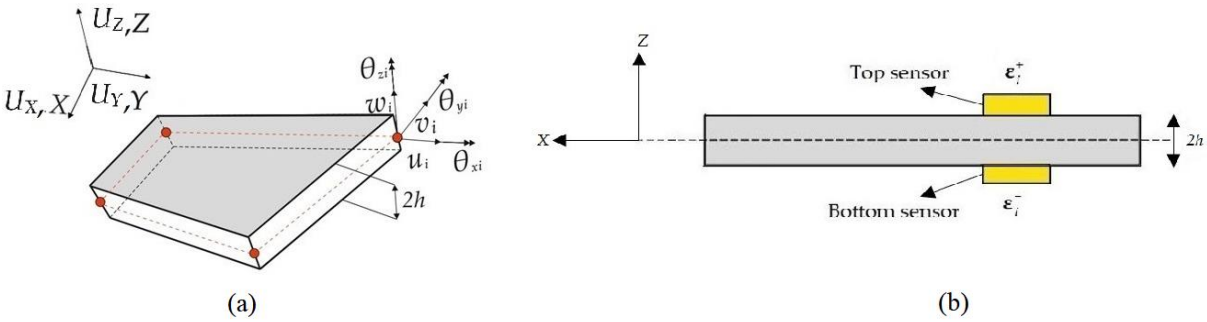

Fig. 5-1. (a) Geometry of iQS4 inverse shell element with related global and local coordinate systems, (b) Position of the strain sensors at top and bottom of the element's surface.

The detailed formulation of the shape functions, displacement vectors and displacement-strain relationships are provided in [3]. The analytical strain components can be calculated in terms of the nodal displacement vector, $\mathbf{u}^e$, as

$$\begin{Bmatrix} \varepsilon_{xx} \\ \varepsilon_{yy} \\ \gamma_{xy} \end{Bmatrix} = \mathbf{e}(\mathbf{u}^e) + z\boldsymbol{\kappa}(\mathbf{u}^e) \;=\; \mathbf{B}^m\mathbf{u}^e + z\mathbf{B}^k\mathbf{u}^e \tag{1a}$$

$$\begin{Bmatrix} \gamma_{xz} \\ \gamma_{yz} \end{Bmatrix} = \mathbf{g}(\mathbf{u}^e) = \;\mathbf{B}^s\mathbf{u}^e \tag{1b}$$

where $\mathbf{e}$, $\boldsymbol{\kappa}$, and g represent the analytical membrane, bending, and transverse shear strains respectively and $\mathbf{B}^s$, $\mathbf{B}^m$ and $\mathbf{B}^k$ are the matrices containing derivatives of the iQS4 shape functions. The explicit forms of these matrices can be found in [3]. To calculate the experimental counterparts of the numerical section strains, strain rosettes should be located on top and bottom surfaces of each iQS4 element as depicted in Fig. 5-1(b). Using these in-situ strain measures, one can easily calculate the experimental section strains as:

$$\left[\mathbf{e}_{\mathrm{i}}^{\varepsilon} \quad \boldsymbol{\kappa}_{\mathrm{i}}^{\varepsilon}\right] \equiv \left[\frac{1}{2}(\boldsymbol{\varepsilon}_i^+ + \boldsymbol{\varepsilon}_i^-) \quad \frac{1}{2h}(\boldsymbol{\varepsilon}_i^+ - \boldsymbol{\varepsilon}_i^-)\right] \quad (i = 1,2,...,n_s) \tag{2}$$

where $\mathrm{e}_{\mathrm{i}}^{\varepsilon}$ and $\kappa_{\mathrm{i}}^{\varepsilon}$ show the experimental counterparts of the membrane and bending strains for n_s numbers of discrete sensors, respectively. The experimental transverse shear strain $\mathrm{g}_{\mathrm{i}}^{\varepsilon}$ cannot be directly extracted from the obtained strain measurements. Nevertheless, the contribution of this shear strain for shape sensing of slender structures can be safely omitted due to its minor effect among other strains. The weighted least-square functional can be defined based on the numerical and experimental section strains as follows:

$$\Phi(\mathbf{u}^e) = \mathrm{w}_e \left\|\mathbf{e}(\mathbf{u}^e) - \mathrm{e}^{\varepsilon}\right\|^2 + \mathrm{w}_k \left\|\boldsymbol{\kappa}(\mathbf{u}^e) - \boldsymbol{\kappa}^{\varepsilon}\right\|^2 + \mathrm{w}_g \left\|\mathbf{g}(\mathbf{u}^e) - \mathbf{g}^{\varepsilon}\right\|^2 \tag{3}$$

where the weighting constants of individual section strains w_e, w_k, and w_g are related to membrane, bending, and transverse shear section strains, respectively. If any of the experimental section strain data is missing, then the related weighting constants are set to a small positive value such as $\mathrm{w}_e = \mathrm{w}_k = \mathrm{w}_g = 10^{-4}$. Otherwise, they are assumed to be equal to unity. Minimizing the Φ functional with respect to the nodal displacement vector results in an equation in the form below:

$$\frac{\partial \Phi(\mathbf{u}^e)}{\partial \mathbf{u}^e} = \mathbf{k}^e \mathbf{u}^e - \mathbf{f}^e = 0 \Rightarrow \mathbf{k}^e \mathbf{u}^e = \mathbf{f}^e \tag{4}$$

where the $\mathbf{k}^e$ and $\mathbf{f}^e$ are analytical shape matrix and experimental shape vector in the local coordinate system, respectively. These local quantities can be transformed into a global coordinate system by using an appropriate transformation matrix, $\mathbf{T}^e$ as:

$$\mathbf{KU} = \mathbf{F} \tag{5a}$$

$$\mathbf{K} = \bigcup_{e=1}^{N_{el}} \left[(\mathbf{T}^e)^T \mathbf{k}^e \mathbf{T}^e \right], \; \mathrm{F} = \bigcup_{e=1}^{N_{el}} \left[(\mathbf{T}^e)^T \mathbf{f}^e \right], \; \mathbf{U} = \bigcup_{e=1}^{N_{el}} \left[(\mathbf{T}^e)^T \mathbf{u}^e \right] \tag{5b}$$

where the $\bigcup$ operator denotes assembly process of the finite element method, and the $\mathbf{U}, \mathbf{F}$, and $\mathbf{K}$ represent the shape matrix, displacement vector, and experimental shape vector, in global coordinate system in the given order. In this study, the accuracy and efficiency of the iFEM element are assessed by computing the percent difference for the maximum values of the total displacement between iFEM and FEM analyses as

$$\text{Percent Difference}(\%) = \left| \frac{\delta^{\text{iFEM}} - \delta^{\text{FEM}}}{\delta^{\text{FEM}}} \right| \times 100 \tag{6}$$

5.3. Shape Sensing of a Doubly Curved Aft Fuselage Panel using Inverse Finite Element Method

Shape sensing of a three-dimensional multi-layered aft fuselage panel is performed based on the iFEM analyses. The panel has a doubly curved geometry which is supported by longitudinal girders and lateral stiffeners as shown in Fig. 5-2. Both the plate and the stringers have a uniform thickness of 10 mm and an unsymmetric balanced angle-ply lamination stacking sequence with fiber angles of (-30/45/0/-45/30). Each of these layers is made of carbon-epoxy material and has an equal thickness of 2 [mm] resulting in a total laminate thickness of 10 [mm]. The mechanical properties of the carbon-epoxy material are provided in Table 5-1. The panel is subjected to a constant pressure of 24 [MPa] along positive z-direction and all the edges are fully clamped. The geometrical dimensions of the panel are illustrated in Fig. 5-2.

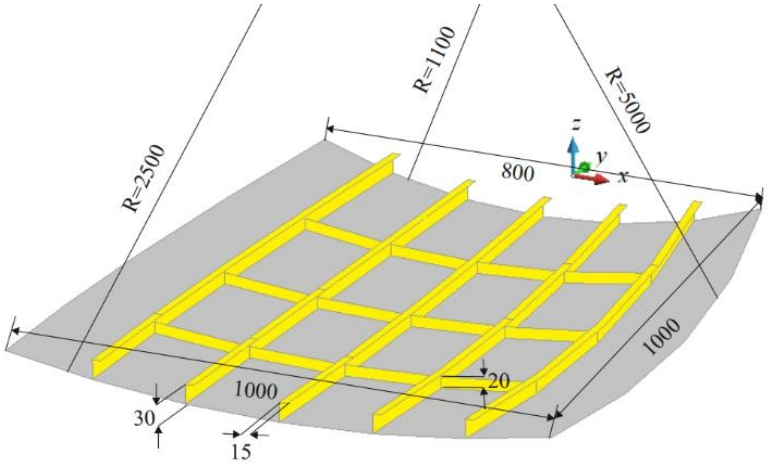

Fig. 5-2. Dimensions of the stiffened multi-layered aft fuselage panel (all in millimeters).

As previously discussed, the most critical part of iFEM analyses is collecting the experimental strain measurements from the top and bottom surfaces of the structural components. Before installing the sensor network to the structure experimentally, one must configure a precise layout of the sensors' locations.

Table 5-1. Mechanical properties of the unidirectional carbon-epoxy material

Lamina material	Young's modulus [GPa]	Poisson's ratio	Shear modulus [GPa]
Unidirectional carbon-epoxy composite	$E_1^{(k)} = 157.9$ $E_2^{(k)} = E_3^{(k)} = 9.584$	$\upsilon_{12}^{(k)} = \upsilon_{13}^{(k)} = 0.32$ $\upsilon_{23}^{(k)} = 0.49$	$G_{12}^{(k)} = G_{13}^{(k)} = 5.93$ $G_{23}^{(k)} = 3.227$

The required experimental strain data can be obtained either by in-situ strain measurement systems (e.g., strain gauges, rosettes, and FBGs) or simulated through a high-fidelity FEM analysis, which can be utilized as discrete strain data in the iFEM formulation. Furthermore, the FEM analysis is used as a reliable reference solution to be compared with iFEM results. In the current study, the iFEM and FEM models possess 96 and 2573 elements, respectively. The weighting constants corresponding to the membrane and bending strains of the elements mounted a sensor at the center were set to unity. However, for the elements with no sensors, these constants were defined as a very small value (i.e.,10-6). Weighting coefficient of the transverse shear strains was set to for all iQS4 elements.

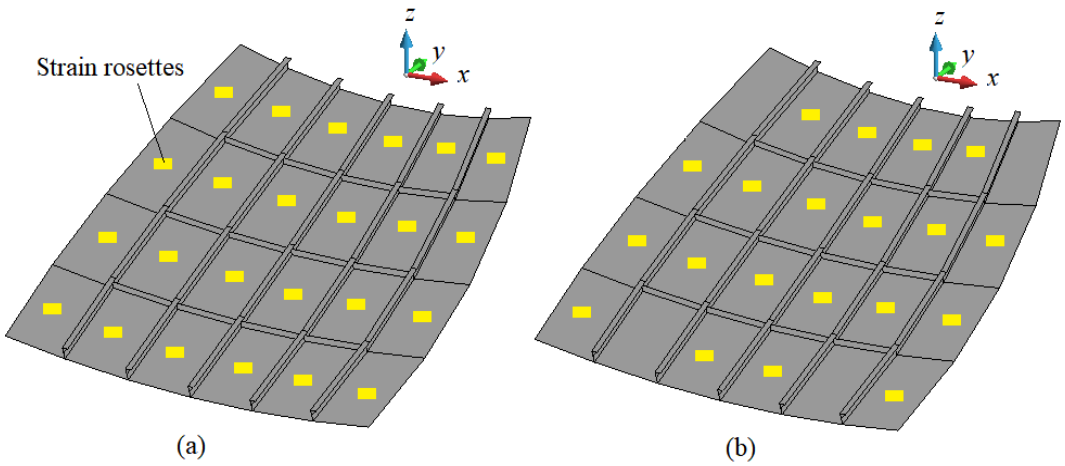

Fig. 5-3. Sensor deployment used for a) iFEM, and b) iFEM(D) analyses.

The iFEM-iQS4 model utilizes the strain data collected from the sensors located on the surface elements of the panel and therefore, it has just 20 elements installed with top and bottom strain rosettes as shown in Fig. 5-3(a). For most of engineering applications, sensor damage/loss is almost inevitable during severe manufacturing and/or operational conditions. Therefore, to illustrate the practical efficiency and accuracy of the iFEM approach, some damaged/broken sensors were simulated arbitrarily among other sensors. For this purpose, one-sixth of the whole sensors (i.e., four sensors) are assumed to be out of service as depicted in Fig. 5-3(b). The symbol 'iFEM(D)' is used to represent the iFEM analyses possessing damaged/broken sensors.

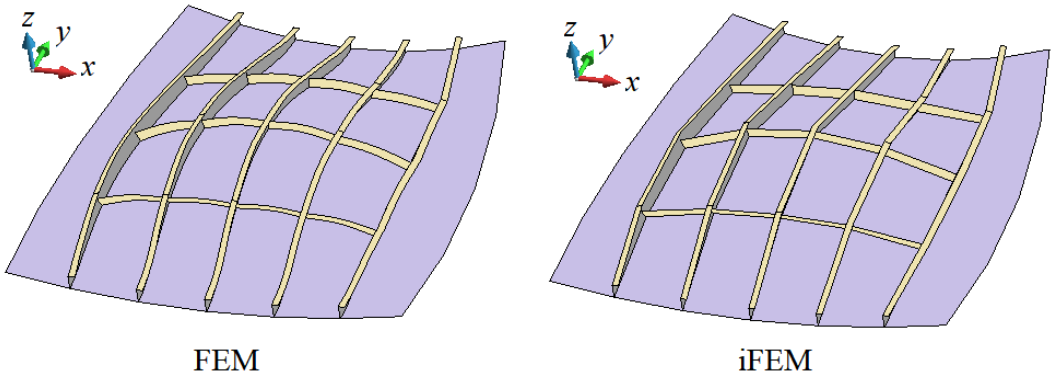

Fig. 5-4. The FEM and iFEM deformed shapes (with same magnitude factor of 2000).

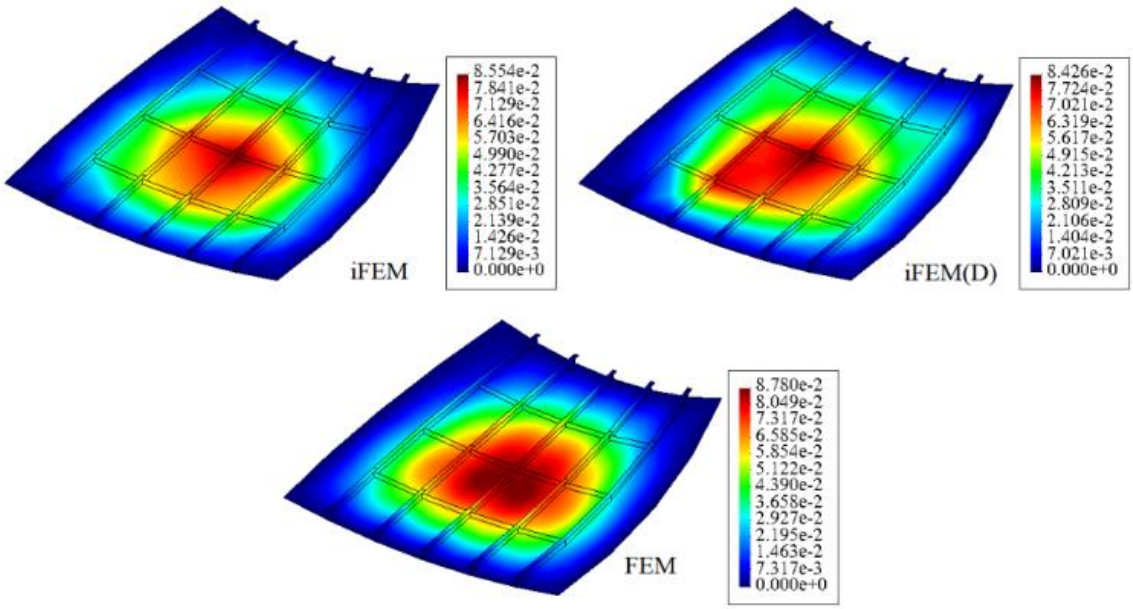

Fig. 5-5. Total displacement fields obtained by FEM, iFEM, and iFEM(D) analyses.

Regarding the quantitative results in Figs. 5-5,5-6, the percentage differences in the maximum total displacement for iFEM and iFEM(D) analyses compared to the reference solutions FEM are about 2.6% and 4.0%, respectively. This error percentage for maximum total rotation between the mentioned analyses are 0.4%, and 1.0% in the given order. Furthermore, the total displacement and rotation contours obtained from the iFEM analyses show superior reconstruction capability of the iQS4 approach for the SCP. In the case of the iFEM(D) model, the obtained contours also show high efficiency and reliable accuracy, even though they are less precise than those of the iFEM model with intact sensors.

Moreover, to investigate the ability of the iFEM approach to reconstruct the full-field strain components, the equivalent strain state obtained from the iFEM analyses for a single layer, i.e., the top layer, is compared with the results from FEM in Fig. 5-7. This equivalent strain state can be used to predict damage and can be calculated under plane stress conditions as follows:

$$\varepsilon_{eq} = \frac{\sqrt{2}}{3}\sqrt{(\varepsilon_1 - \varepsilon_2)^2 + (\varepsilon_2 - \varepsilon_3)^2 + (\varepsilon_1 - \varepsilon_3)^2} \tag{7}$$

where, and are principal strains obtained from iFEM analyses. The reconstructed contours are quite similar to the FEM reference solution and the percentage error between the maximum values of FEM and the iFEM results is less than 1.3%. Overall, the quantitative contour results and the reconstructed deformed shapes indicate that the iFEM approach can be readily used to predict high-precision full-field displacements, even in the case of an on-board sensor network with multiple defective/damaged sensors. Moreover, the obtained equivalent strain contours and results prove that iFEM is capable of reconstructing strain fields with high precision. Therefore, for structural monitoring of various aircraft components (particularly, aft fuselage panels), iFEM can be classified as one of the most robust and accurate systems for shape sensing and real-time monitoring.

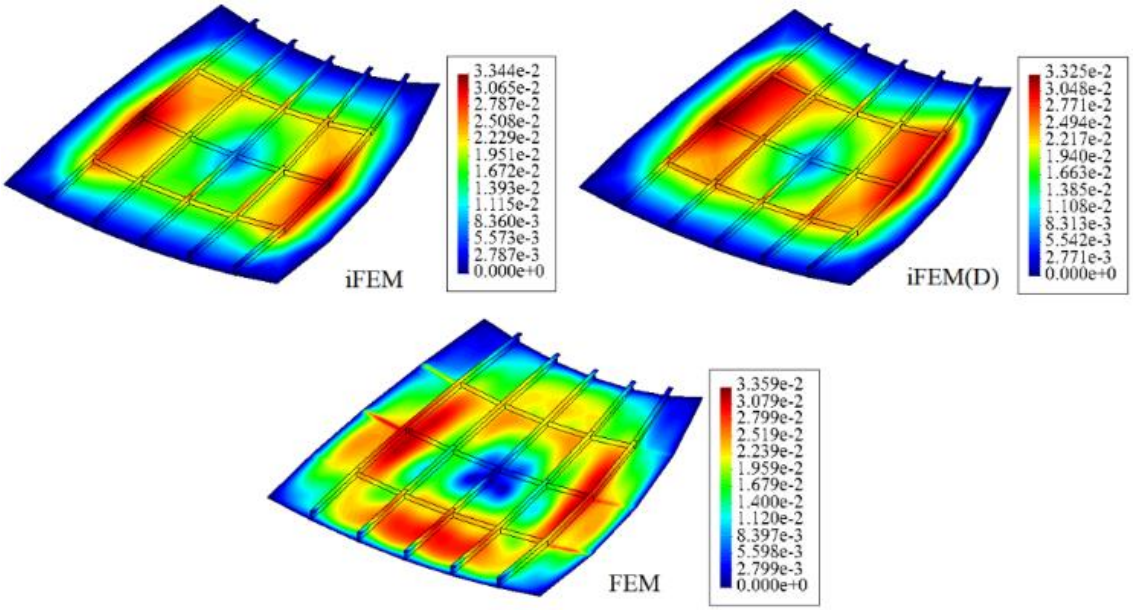

Fig. 5-6. Total rotation fields obtained by FEM, iFEM, and iFEM(D) analyses.

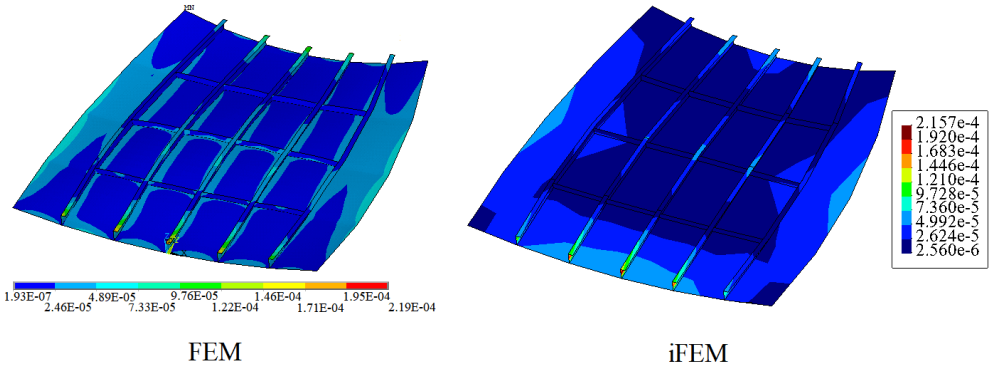

Fig. 5-7. Equivalent strain fields obtained by FEM, and iFEM analyses.

Overall, the quantitative contour results and the reconstructed deformed shapes indicate that the iFEM approach can readily be used to predict high-precision full-field displacements, even in the case of an on-board sensor network that has multiple defective/damaged sensors. Therefore, for structural health monitoring of various aircraft components (particularly, aft fuselage panels), iFEM can be classified as one of the most robust and accurate systems for shape sensing and real-time monitoring.

5.4. Three-Dimensional Shape Sensing of a Representative Ship-Hull Cross-Section Based on Inverse Finite Element Method

A representative cross-section of a small ship-hull is considered to be shape estimated using the iFEM method. The cross-section of this ship-hull has a width of 5m, a height of 2.5 m, and a depth of 2 m as demonstrated in Fig. 5-8. The hull is stiffened laterally and longitudinally using girders with 0.2 m width as shown in Fig. 5-8. All components of this hull are made of 5 mm thick sheets of AISI type 304 stainless steel. It is presumed that 1.5 m of the hull becomes under the water subjected to hydrostatic pressure. Moreover, the right and left panels of the hull are exposed to water wave strikes of maximum a 6 KPa pressure. Moreover, all the cross-sectional edges are considered to be fully clamped.

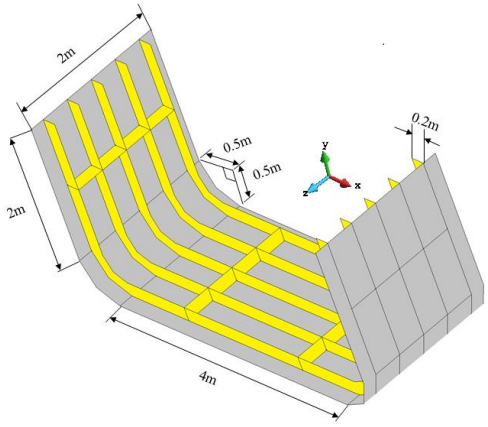

Fig. 5-8. Dimensions of the stiffened ship-hull.

The most important part of the iFEM analyses is the acquisition of the experimental strain measurements on the top and bottom of the structural components. Before installing the sensor network experimentally on the structure, you must create an accurate layout for the location of the sensors. The required experimental strain data can be obtained either by in-situ strain measurement systems (e.g., strain gauges, rosettes and FBGs) or simulated by

a FEM analysis, which can be used as discrete strain data in the iFEM formulation. Moreover, the FEM analysis is used as a reliable reference solution that can be compared with the iFEM results. In the current study, the iFEM model consist of 148 elements which 48 of them are accommodated with strain rosettes as shown in Fig 5-9(a). The weighting constants corresponding to the membrane and bending strains of the elements that have a sensor in the center were set to unity. However, for the elements without sensors, these constants were defined with a very small value (i.e., 10^{-8}). The weighting coefficient of the transverse shear strains was set to $w_g = 10^{-5}$ for all iQS4 elements.

In most engineering applications, damage or loss of the sensors is almost inevitable under difficult manufacturing and/or operating conditions. Therefore, to illustrate the practical efficiency and accuracy of the iFEM approach, some damaged/broken sensors were randomly simulated among other sensors. For this purpose, one-sixth of the total sensors (i.e., eight sensors) are assumed to be out of service, as shown in Fig. 5-9(b). The symbol 'iFEM_D' is used to represent the iFEM analyses with damaged/defective sensors.

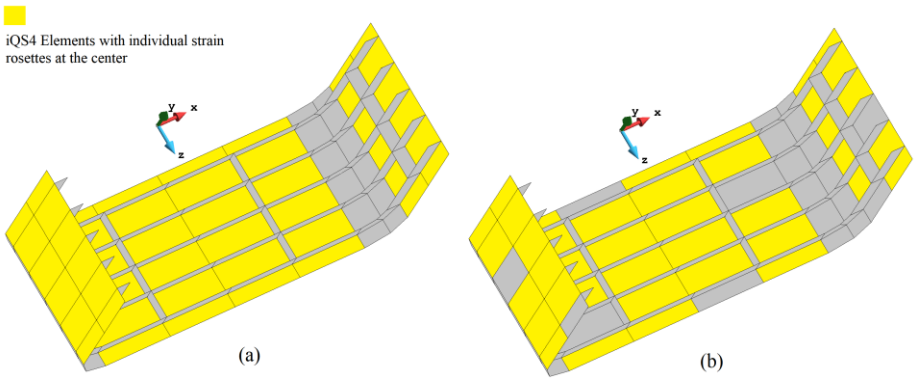

Fig. 5-9. Sensor deployment used for (a) iFEM, and b) iFEM_D analyses.

In this section, the results of the iFEM and FEM analyses are compared and discussed in detail to verify the predictive shape detection capability of the iQS4 element. Fig. 5-10 shows the deformed shapes of the preventative ship-hull cross section obtained from both FEM and iFEM analyses. Note that the deformation values for both solutions are magnified by the same factor 4000. Observing Fig. 5-11, one can easily understand that iFEM has reasonable potential to reconstruct the 3D full-field deformations compared to the results obtained by FEM. This proves the practical suitability of iFEM-iQS4 as a reliable system for shape acquisition.

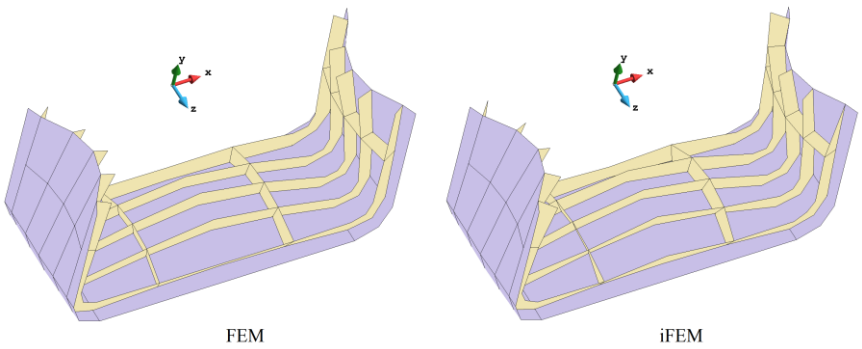

Fig. 5-10. The FEM and iFEM deformed shapes (with same magnitude factor of 4000).

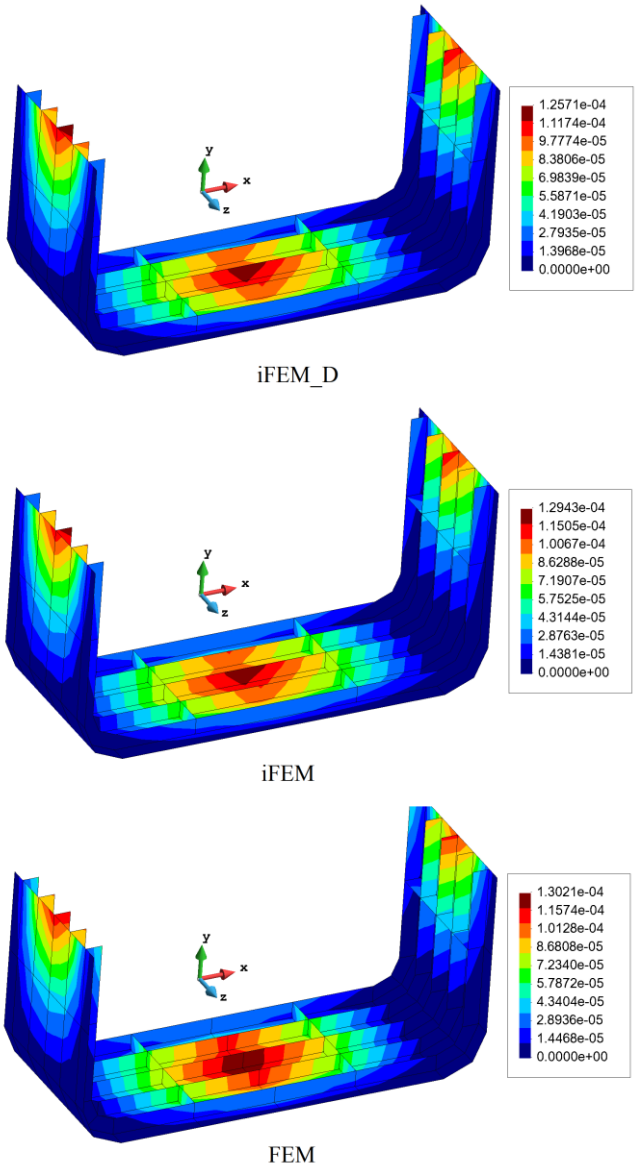

Fig. 5-11. Total displacement fields obtained by FEM, iFEM, and iFEM_D analyses.

As for the quantitative results in Fig. 5-11, the percentage differences between the maximum total displacement of iFEM, iFEM_D and the reference solution FEM are about 0.6% and 3.4%, respectively. Moreover, the total displacement contours obtained from the iFEM analyses show a superior similarity between FEM and iFEM analyses. Overall, the quantitative contour results and the reconstructed deformed shapes show that the iFEM approach can be easily used to predict high-precision full-field displacements, even in the case of an on-board sensor network with multiple defective/damaged sensors. Therefore, for monitoring the structural health of various marine components iFEM can be classified as one of the most robust and accurate shape detection and real-time monitoring systems.

5.5. Conclusions

The shape sensing of a multilayered aft fuselage panel with double curved geometry and a representative ship hull structure are carried out using a new sensor-based approach called iFEM. The obtained results clearly show that this method is robust enough to reconstruct the translational and rotational fields and is able to predict quantitative results with a small deviation from the FEM reference solution, even when some of the sensors are out of service due to operational and application situations. This study is one of the first attempts to capture the shape of aft fuselage panels of aircrafts using iFEM methodology. The knowledge gained from this study may lead to the expansion of numerical applications of shape sensing other aircraft and marine structural components using iFEM technique in the future.

CHAPTER 6. General Conclusions

6.1 Achievements against the Objectives

The main objective of this dissertation was to investigate numerical and experimental applications for shape and stress sensing of shell structures using iFEM analysis. The results of this work, which are consistent with the research objectives, are given below:

1. The main existing iFEM shell elements (i.e., iMIN3, iQS4 and iCS8) are compared in terms of their accuracy and efficiency for shape and stress sensing of structural components with simple and complex geometries. For this purpose, three numerical benchmark problems are considered to be evaluated by these iFEM elements. Moreover, the damage detection capability of these iFEM elements is evaluated as the fourth numerical example. FEM analyses are utilized as a reference solution to compare with iFEM results. It was demonstrated that quadrilateral inverse elements (i.e., iQS4 and iCS8) are more accurate regarding the shape and stress sensing of complex geometries. Between two quadrangular elements, iCS8 shows more promising results. This improvement in iCS8 prediction is due to the higher order serendipity shape functions, which allow an additional middle node to better precede shape and stress field reconstruction and damage prediction.

2. An improved iFEM formulation compatible with the RZT approach was developed based on a weighted least-squares variational principle using the full set of strain measures. A new iFEM-RZT-based inverse element, named iRZT4, is derived using this formulation to investigate the shape and stress sensing of thick and moderately thick sandwich structures. The robustness and effectiveness of this new element is demonstrated through a series of experimental and numerical case studies using only a few discrete sensors. Furthermore, an efficient smoothing method, called the strain pre-extrapolation technique, is coupled with iFEM-RZT analyses to obtain smoother strain results over the entire aera of the structure. In addition to the FEM analyses, the full-field displacement contours obtained with the DIC technique used as an additional evaluation method for comparing the data from iFEM-RZT and -FSDT analyses.

3. Shape sensing of geometrically nonlinear deformations of thin multilayer plates/shells was evaluated by numerical and experimental case studies using iFEM analyses. Large deformations and post-buckling analyses of flat and curved multilayer thin composites were investigated numerically, while the geometrically nonlinear deformation of a thin multilayer plate was studied experimentally. The obtained qualitative and quantitative results show the high accuracy of the iFEM method in predicting the translational and rotational displacement fields. Moreover, in the case of the experimental example, a pre-extrapolation technique was coupled with iFEM analyses to obtain the strain data from a discrete set of sensors over the entire domain of the structure.

4. Health monitoring of structural components for marine and aerospace applications has been studied using iFEM. These applications are the most common uses of shell-like structures in engineering fields. For this purpose, a representative ship hull and aft fuselage structures was modeled and evaluated by iFEM analyses. In this work, the effects of the absence of some sensors during operation are investigated. The obtained results clearly show that this method is robust enough to reconstruct the translational and rotational fields and is able to predict quantitative results with a small deviation from the FEM reference solution, even when some of the sensors are out of service due to operational and application situations.

6.2 Novelty and Contribution to the Field

Nowadays, there are many research papers using iFEM approach for shape and stress sensing of different structural components. However, no comparative study had investigated the efficiency and accuracy of different iFEM elements for shape and stress sensing and damage identification of structural components with simple/complex geometries. The study described in Chapter 2 provides an overview and comparative study between existing inverse shell elements in terms of their performance in predicting full-field displacements, strains and stresses, and damage prediction capability. This work will be a reliable guide for other researchers to select a suitable inverse shell element considering the desired geometry.

In recent decades, the use of composite and sandwich material systems as primary structures in various engineering applications has increased significantly. The study described in Chapter 3 presents a newly developed RZT-based inverse shell element suitable for shape sensing of thick and moderately thick sandwich and multilayer composite structures, where iFEM-FSDT loses accuracy due to the linear relationship between kinematic variables through the thickness of the structure. Furthermore, since the number of sensors used in experimental analyses is limited, a smoothing method is needed to cover all missing strain data. This study fills this gap by introducing a highly efficient smoothing method (strain pre-extrapolation technique) to recover strain data over the entire domain of the structure. By coupling iFEM-RZT with extrapolated strain data, a robust shape sensing algorithm is provided for the various engineering applications of composite materials.

Thin multilayer composites are widely used in industry. These components are usually subjected to geometrically nonlinear deformations that can lead to complete failure of the structure. iFEM as a reliable health monitoring system can also play a shape sensing role for this type of requirements. The study described in Chapter 4 demonstrates this capability of iFEM methodology for shape sensing of thin plate/shell multilayered structures subjected to nonlinear deformations. Finally, the study described in Chapter 5 shows the applications of the iFEM/iQS4 methodology for shape sensing of marine and aerospace structures. The literature was lacking such a novel application, which can now be found in this thesis.

6.3 Gaps and Future Studies

- Regarding the best performance of the iFEM-iCS8 element presented in Chapter 2, there are few numerical studies, and no experimental study has been conducted to better evaluate the capability of this element in engineering applications. Therefore, this high-performance element can be further considered in iFEM shape sensing applications.

- The iFEM-iRZT4 inverse shell element presented in Chapter 3 can be further investigated for shape and stress sensing of thick and moderately thick sandwich and multilayer composites with curved fiber orientations and/or functionally graded materials that impart different stiffness properties to the structure.

- Although Chapter 4 explored the superior capabilities of the iFEM approach for shape sensing of composites subjected to geometrically nonlinear deformations, this performance can also be examined for structures where material nonlinearity (plasticity) and contact issues are present.

- In addition to aerospace and marine structural components, which were explained as iFEM applications in Chapter 5, other technical areas such as the automotive as well as oil, gas and petrochemical industries can be scrutinized as SHM applications of iFEM technology.

- In the present work, the performance of iFEM is evaluated only for the static and quasi-static load cases. However, the structural components under dynamic load effects can also be evaluated using iFEM methodology.

REFERENCES

1. Tikhonov, A. N., Arsenin, V. I., & Arsenin, V. Y. (1977). Solutions of ill-posed problems. Vh Winston.

2. Maniatty, A., & Zabaras, N. (1989). Method for solving inverse elastoviscoplastic problems. Journal of engineering mechanics, 115(10), 2216-2231.

3. Schnur, D. S., & Zabaras, N. (1990). Finite element solution of two-dimensional inverse elastic problems using spatial smoothing. International Journal for Numerical Methods in Engineering, 30(1), 57-75.

4. Maniatty, A. M., & Zabaras, N. J. (1994). Investigation of regularization parameters and error estimating in inverse elasticity problems. International journal for numerical methods in engineering, 37(6), 1039-1052.

5. Tarantola, A. (2005). Inverse problem theory and methods for model parameter estimation. Society for Industrial and Applied Mathematics.

6. Davis, M. A., Kersey, A. D., Sirkis, J., & Friebele, E. J. (1996). Shape and vibration mode sensing using a fiber optic Bragg grating array. Smart Materials and Structures, 5(6), 759.

7. Kang, L. H., Kim, D. K., & Han, J. H. (2007). Estimation of dynamic structural displacements using fiber Bragg grating strain sensors. Journal of sound and vibration, 305(3), 534-542.

8. Bogert, P., Haugse, E., & Gehrki, R. (2003, April). Structural shape identification from experimental strains using a modal transformation technique. In 44th AIAA/ASME/ASCE/AHS/ASC Structures, Structural Dynamics, and Materials Conference (p. 1626).

9. Jones, R. T., Bellemore, D. G., Berkoff, T. A., Sirkis, J. S., Davis, M. A., Putnam, M. A., ... & Kersey, A. D. (1998). Determination of cantilever plate shapes using wavelength division multiplexed fiber Bragg grating sensors and a least-squares strain-fitting algorithm. Smart materials and structures, 7(2), 178.

10. Glaser, R., Caccese, V., & Shahinpoor, M. (2012). Shape monitoring of a beam structure from measured strain or curvature. Experimental mechanics, 52(6), 591-606.

11. Kim, N. S., & Cho, N. S. (2004). Estimating deflection of a simple beam model using fiber optic Bragg-grating sensors. Experimental mechanics, 44(4), 433-439.

12. Ko, W. L., Richards, W. L., & Fleischer, V. T. (2009). Applications of Ko displacement theory to the deformed shape predictions of the doubly-tapered Ikhana Wing (No. NASA/TP-2009-214652).

13. Chierichetti, M. (2014). Load and response identification for a nonlinear flexible structure subject to harmonic loads. Journal of Computational and Nonlinear Dynamics, 9(1).

14. Tessler, A. (2003). A variational principle for reconstruction of elastic deformations in shear deformable plates and shells. National Aeronautics and Space Administration, Langley Research Center.

15. Tessler, A., & Spangler, J. L. (2005). A least-squares variational method for full-field reconstruction of elastic deformations in shear-deformable plates and shells. Computer methods in applied mechanics and engineering, 194(2-5), 327-339.

16. Abdollahzadeh, M. A., Kefal, A., & Yildiz, M. (2020). A comparative and review study on shape and stress sensing of flat/curved shell geometries using C0-continuous family of iFEM elements. Sensors, 20(14), 3808.

17. Abdollahzadeh, M. A., Tabrizi, I. E., Kefal, A., & Yildiz, M. (2021). A combined experimental/numerical study on deformation sensing of sandwich structures through inverse analysis of pre-extrapolated strain measurements. Measurement, 185, 110031.

18. Abdollahzadeh, M.A., Ali, H.Q., Yildiz, M., and Kefal, A. (2022). Experimental and Numerical Investigation on Large Deformation Reconstruction of Thin Laminated Composite Structures using Inverse Finite Element Method. Thin-walled structures, 178, 109485.

19. Abdollahzadeh, M.A., Yildiz, M. & Kefal, A. (2021). Three-Dimensional Shape Sensing of a Representative Ship-Hull Cross-Section Based on Inverse Finite Element Method. 34th Asian-Pacific Technical Exchange and Advisory Meetings on Marine Structures (TEAM) - Istanbul, Turkey

20. Abdollahzadeh, M.A., Kefal, A. & Yildiz, M. (2022). Shape Sensing of a Doubly Curved Aft Fuselage Panel using Inverse Finite Element Method. 9th IEEE International workshop on Metrology for Aerospace- Pisa, Italy.

21. Glisic, B., & Inaudi, D. (2008). Fibre optic methods for structural health monitoring. Wiley.

22. Kefal, A. (2017). Structural health monitoring of marine structures by using inverse finite element method (Doctoral dissertation, University of Strathclyde).

23. Gherlone, M., Cerracchio, P., & Mattone, M. (2018). Shape sensing methods: Review and experimental comparison on a wing-shaped plate. Progress in Aerospace Sciences, 99, 14-26.

24. Rocha, B., Silva, C., Keulen, C., Yildiz, M., & Suleman, A. (2013). Structural health monitoring of aircraft structures. In New Trends in Structural Health Monitoring (pp. 81-148). Springer, Vienna.

25. Rocha, B., Silva, C., Yildiz, M., & Suleman, A. (2018). Design and development of a phased array system for damage detection in structures. In Structural Health Monitoring for Advanced Composite Structures (pp. 153-189).

26. Yin, T., & Lam, H. F. (2013). Dynamic analysis of finite-length circular cylindrical shells with a circumferential surface crack. Journal of Engineering Mechanics, 139(10), 1419-1434.

27. Moazzez, K., Googarchin, H. S., & Sharifi, S. M. H. (2018). Natural frequency analysis of a cylindrical shell containing a variably oriented surface crack utilizing line-spring model. thin-walled structures, 125, 63-75.

28. Kefal, A., & Oterkus, E. (2016). Displacement and stress monitoring of a Panamax containership using inverse finite element method. Ocean Engineering, 119, 16-29..

29. Kocaman, E. S., Yilmaz, C., Deniz, A., & Yildiz, M. (2018). The performance of embedded fiber Bragg grating sensors for monitoring failure modes of foam cored sandwich structures under flexural loads. Journal of Sandwich Structures & Materials, 20(5), 553-577.

30. Yilmaz, C., Akalin, C., Kocaman, E. S., Suleman, A., & Yildiz, M. (2016). Monitoring Poisson's ratio of glass fiber reinforced composites as damage index using biaxial Fiber Bragg Grating sensors. Polymer Testing, 53, 98-107.

31. Kocaman, E. S., Akay, E., Yilmaz, C., Turkmen, H. S., Misirlioglu, I. B., Suleman, A., & Yildiz, M. (2017). Monitoring the damage state of fiber reinforced composites using an FBG network for failure prediction. Materials, 10(1), 32.

32. Yilmaz, C., & Yildiz, M. (2017). A study on correlating reduction in Poisson's ratio with transverse crack and delamination through acoustic emission signals. Polymer Testing, 63, 47-53.

33. Keulen, C. J., Akay, E., Melemez, F. F., Kocaman, E. S., Deniz, A., Yilmaz, C., ... & Suleman, A. (2016). Prediction of fatigue response of composite structures by monitoring the strain energy release rate with embedded fiber Bragg gratings. Journal of Intelligent Material Systems and Structures, 27(1), 17-27.

34. Gherlone, M., Cerracchio, P., Mattone, M., Di Sciuva, M., & Tessler, A. (2012). Shape sensing of 3D frame structures using an inverse finite element method. International Journal of Solids and Structures, 49(22), 3100-3112.

35. Gherlone, M., Cerracchio, P., Mattone, M., Di Sciuva, M., & Tessler, A. (2014). An inverse finite element method for beam shape sensing: theoretical framework and experimental validation. Smart Materials and Structures, 23(4), 045027.

36. Liu, M., Zhang, X., Song, H., Zhou, S., Zhou, Z., & Zhou, W. (2018). Inverse finite element method for reconstruction of deformation in the gantry structure of heavy-duty machine tool using FBG sensors. Sensors, 18(7), 2173.

37. Zhao, Y., Du, J., Bao, H., & Xu, Q. (2018). Optimal sensor placement based on eigenvalues analysis for sensing deformation of wing frame using iFEM. Sensors, 18(8), 2424.

38. Tessler, A., Di Sciuva, M., & Gherlone, M. (2010). A consistent refinement of first-order shear deformation theory for laminated composite and sandwich plates using

improved zigzag kinematics. Journal of Mechanics of Materials and Structures, 5(2), 341-367.

39. Cerracchio, P., Gherlone, M., Di Sciuva, M., & Tessler, A. (2015). A novel approach for displacement and stress monitoring of sandwich structures based on the inverse Finite Element Method. Composite Structures, 127, 69-76.

40. Kefal, A., Tessler, A., & Oterkus, E. (2017). An enhanced inverse finite element method for displacement and stress monitoring of multilayered composite and sandwich structures. Composite Structures, 179, 514-540.

41. Kefal, A., Tessler, A., & Oterkus, E. (2018). An efficient inverse finite element method for shape and stress sensing of laminated composite and sandwich plates and shells (No. L-20938).

42. Tessler, A., & Spangler, J. L. (2004, January). Inverse FEM for full-field reconstruction of elastic deformations in shear deformable plates and shells. In 2nd European Workshop on Structural Health Monitoring.

43. Kefal, A., Oterkus, E., Tessler, A., & Spangler, J. L. (2016). A quadrilateral inverse-shell element with drilling degrees of freedom for shape sensing and structural health monitoring. Engineering science and technology, an international journal, 19(3), 1299-1313.

44. Kefal, A. (2019). An efficient curved inverse-shell element for shape sensing and structural health monitoring of cylindrical marine structures. Ocean Engineering, 188, 106262.

45. Tessler, A., & Hughes, T. J. (1985). A three-node Mindlin plate element with improved transverse shear. Computer Methods in Applied Mechanics and Engineering, 50(1), 71-101.

46. Tessler, A., & Hughes, T. J. (1983). An improved treatment of transverse shear in the Mindlin-type four-node quadrilateral element. Computer methods in applied mechanics and engineering, 39(3), 311-335.

47. Tessler, A., & Dong, S. B. (1981). On a hierarchy of conforming Timoshenko beam elements. Computers & structures, 14(3-4), 335-344.

48. Ahmad, S., Irons, B. M., & Zienkiewicz, O. C. (1970). Analysis of thick and thin shell structures by curved finite elements. International journal for numerical methods in engineering, 2(3), 419-451.

49. Papa, U., Russo, S., Lamboglia, A., Del Core, G., & Iannuzzo, G. (2017). Health structure monitoring for the design of an innovative UAS fixed wing through inverse finite element method (iFEM). Aerospace Science and Technology, 69, 439-448.

50. Tessler, A., Roy, R., Esposito, M., Surace, C., & Gherlone, M. (2018). Shape sensing of plate and shell structures undergoing large displacements using the inverse finite element method. Shock and Vibration.

51. Kefal, A., & Oterkus, E. (2016). Displacement and stress monitoring of a chemical tanker based on inverse finite element method. Ocean Engineering, 112, 33-46.

52. Kefal, A., Mayang, J. B., Oterkus, E., & Yildiz, M. (2018). Three dimensional shape and stress monitoring of bulk carriers based on iFEM methodology. Ocean Engineering, 147, 256-267.

53. Kefal, A., & Oterkus, E. (2017). Shape and stress sensing of offshore structures by using inverse finite element method. Progress in the Analysis and Design of Marine Structures, 141-148.

54. Li, M., Kefal, A., Oterkus, E., & Oterkus, S. (2020). Structural health monitoring of an offshore wind turbine tower using iFEM methodology. Ocean Engineering, 204, 107291.

55. Kefal, A. (2019). Displacement and stress monitoring of a curved stiffened panel based on inverse finite element method. Trends in the Analysis and Design of Marine Structures, 277-284.

56. Esposito, M., & Gherlone, M. (2020). Composite wing box deformed-shape reconstruction based on measured strains: Optimization and comparison of existing approaches. Aerospace Science and Technology, 99, 105758.

57. Kefal, A., & Yildiz, M. (2017). Modeling of sensor placement strategy for shape sensing and structural health monitoring of a wing-shaped sandwich panel using inverse finite element method. Sensors, 17(12), 2775.

58. Colombo, L., Sbarufatti, C., & Giglio, M. (2019). Definition of a load adaptive baseline by inverse finite element method for structural damage identification. Mechanical Systems and Signal Processing, 120, 584-607.

59. Li, M., Kefal, A., Cerik, B. C., & Oterkus, E. (2020). Dent damage identification in stiffened cylindrical structures using inverse Finite Element Method. Ocean Engineering, 198, 106944.

60. Piraccini, M., & Di Sante, R. (2018). Measurement of nonlinear vibration response in aerospace composite blades using pulsed airflow excitation. Measurement, 130, 422-434.

61. Lolive, E., Casari, P., & Davies, P. (2005). Loading rate effects on foam cores for marine sandwich structures. In Sandwich structures 7: advancing with sandwich structures and materials (pp. 895-903). Springer, Dordrecht.

62. Kefal, A., Hasim, K. A., & Yildiz, M. (2019). A novel isogeometric beam element based on mixed form of refined zigzag theory for thick sandwich and multilayered composite beams. Composites Part B: Engineering, 167, 100-121.

63. Chen, N. Z., Sun, H. H., & Soares, C. G. (2003). Reliability analysis of a ship hull in composite material. Composite structures, 62(1), 59-66.

64. Xie, H., Ren, H., Qu, S., & Tang, H. (2018). Numerical and experimental study on hydroelasticity in water-entry problem of a composite ship-hull structure. Composite Structures, 201, 942-957.

65. Yap, J. W., Scott, M. L., Thomson, R. S., & Hachenberg, D. (2002). The analysis of skin-to-stiffener debonding in composite aerospace structures. Composite Structures, 57(1-4), 425-435.

66. Kassapoglou, C. (2013). Design and analysis of composite structures: with applications to aerospace structures. John Wiley & Sons.

67. Jeyanthi, S., & Rani, J. J. (2012). Improving mechanical properties by kenaf natural long fiber reinforced composite for automotive structures. Journal of Applied Science and Engineering, 15(3), 275-280.

68. Suchat, S., Lanna, A., Chotikhun, A., & Hiziroglu, S. (2020). Some Properties of Composite Drone Blades Made from Nanosilica Added Epoxidized Natural Rubber. Polymers, 12(6), 1293.

69. Manca, M., Quispitupa, A., Berggreen, C., & Carlsson, L. A. (2012). Face/core debond fatigue crack growth characterization using the sandwich mixed mode bending specimen. Composites Part A: Applied Science and Manufacturing, 43(11), 2120-2127.

70. Kim, H., DeFrancisci, G., Chen, Z.M. and Rhymer, J., (2012), April. Impact damage formation on composite aircraft structures. In UCSD FAA JAMS Paper, Technical Review Meeting, 5.

71. Bayraktar, Ş., & Turgut, Y. (2020). Determination of delamination in drilling of carbon fiber reinforced carbon matrix composites/Al 6013-T651 stacks. Measurement, 154, 107493.

72. Zhang, L., Qiu, G., & Chen, Z. (2021). Structural health monitoring methods of cables in cable-stayed bridge: A review. Measurement, 168, 108343.

73. Aulakh, D. S., & Bhalla, S. (2021). 3D torsional experimental strain modal analysis for structural health monitoring using piezoelectric sensors. Measurement, 180, 109476.

74. Lesiak, P., Szeląg, M., Budaszewski, D., Plaga, R., Mileńko, K., Rajan, G., ... & Woliński, T. (2012). Influence of lamination process on optical fiber sensors embedded in composite material. Measurement, 45(9), 2275-2280.

75. Kuang and, K. S. C., & Cantwell, W. J. (2003). Use of conventional optical fibers and fiber Bragg gratings for damage detection in advanced composite structures: A review. Appl. Mech. Rev., 56(5), 493-513.

76. Mieloszyk, M., Andrearczyk, A., Majewska, K., Jurek, M., & Ostachowicz, W. (2020). Polymeric structure with embedded fiber Bragg grating sensor manufactured using multi-jet printing method. Measurement, 166, 108229..

77. Amanzadeh, M., Aminossadati, S. M., Kizil, M. S., & Rakić, A. D. (2018). Recent developments in fibre optic shape sensing. Measurement, 128, 119-137.

78. Minakuchi, S., Okabe, Y., & Takeda, N. (2007). Real-time detection of debonding between honeycomb core and facesheet using a small-diameter FBG sensor embedded in adhesive layer. Journal of Sandwich Structures & Materials, 9(1), 9-33.

79. Rapp, S., Kang, L. H., Han, J. H., Mueller, U. C., & Baier, H. (2009). Displacement field estimation for a two-dimensional structure using fiber Bragg grating sensors. Smart Materials and Structures, 18(2), 025006.

80. Nishio, M., Mizutani, T., & Takeda, N. (2010). Structural shape reconstruction with consideration of the reliability of distributed strain data from a Brillouin-scattering-based optical fiber sensor. Smart Materials and Structures, 19(3), 035011.

81. Savino, P., Tondolo, F., Gherlone, M., & Tessler, A. (2020). Application of inverse finite element method to shape sensing of curved beams. Sensors, 20(24), 7012.

82. Kefal, A., & Oterkus, E. (2020). Isogeometric iFEM analysis of thin shell structures. Sensors, 20(9), 2685.

83. Zhao, F., Xu, L., Bao, H., & Du, J. (2020). Shape sensing of variable cross-section beam using the inverse finite element method and isogeometric analysis. Measurement, 158, 107656.

84. Zhao, F., & Bao, H. (2021). An improved inverse finite element method for shape sensing using isogeometric analysis. Measurement, 167, 108282.

85. Wang, W., Lu, Y., Zhao, D., Zhang, J., & Bai, X. (2020). Research on large deflection deformation reconstruction of elastic thin plate based on strain monitoring. Measurement, 149, 107000.

86. Kefal, A., Tabrizi, I. E., Tansan, M., Kisa, E., & Yildiz, M. (2021). An experimental implementation of inverse finite element method for real-time shape and strain sensing of composite and sandwich structures. Composite Structures, 258, 113431.

87. Kefal, A., Tabrizi, I. E., Yildiz, M., & Tessler, A. (2021). A smoothed iFEM approach for efficient shape-sensing applications: Numerical and experimental validation on composite structures. Mechanical Systems and Signal Processing, 152, 107486.

88. Kefal, A. (2020). A novel four-node inverse-plate element for shape and stress sensing of laminated composite and sandwich plates. Journal of the Faculty of Engineering and Architecture of Gazi University, 35(4), 1767-1781.

89. Oboe, D., Colombo, L., Sbarufatti, C., & Giglio, M. (2021). Comparison of strain pre-extrapolation techniques for shape and strain sensing by iFEM of a composite plate subjected to compression buckling. Composite Structures, 262, 113587.

90. Tessler, A., Riggs, H. R., Freese, C. E., & Cook, G. M. (1998). An improved variational method for finite element stress recovery and a posteriori error estimation. Computer methods in applied mechanics and engineering, 155(1-2), 15-30.

91. Tessler, A., Riggs, H. R., & Dambach, M. (1999). A novel four-node quadrilateral smoothing element for stress enhancement and error estimation. International journal for numerical methods in engineering, 44(10), 1527-1543.

92. Oñate, E. (2013). Structural analysis with the finite element method. Linear statics: volume 2: beams, plates and shells. Springer Science & Business Media.

93. Chen, S., Huang, Y., Gu, P., & Wang, J. Y. (2019). Experimental study on fatigue performance of UHPC-orthotropic steel composite deck. Thin-Walled Structures, 142, 1-18.

94. Jiang, Z., Wan, S., Fang, Z., & Song, A. (2021). Static and fatigue behaviours of a bolted GFRP/steel double lap joint. Thin-Walled Structures, 158, 107170.

95. Sheta, A., Ma, X., Zhuge, Y., ElGawady, M. A., Mills, J. E., Singh, A., & Abd-Elaal, E. S. (2021). Structural performance of novel thin-walled composite cold-formed steel/PE-ECC beams. Thin-Walled Structures, 162, 107586.

96. Dar, M. A., Subramanian, N., Anbarasu, M., Ghowsi, A. F., Arif, P. A., & Dar, A. R. (2021). Testing and FE simulation of lightweight CFS composite built-up columns: Axial strength and deformation behaviour. Thin-Walled Structures, 167, 108222.

97. Kootsookos, A., & Burchill, P. J. (2004). The effect of the degree of cure on the corrosion resistance of vinyl ester/glass fibre composites. Composites Part A: Applied Science and Manufacturing, 35(4), 501-508.

98. Diamanti, K., & Soutis, C. (2010). Structural health monitoring techniques for aircraft composite structures. Progress in Aerospace Sciences, 46(8), 342-352.

99. Yuan, S., Wang, L., & Peng, G. (2005). Neural network method based on a new damage signature for structural health monitoring. Thin-Walled Structures, 43(4), 553-563.

100. Güemes, A., Fernandez-Lopez, A., Pozo, A. R., & Sierra-Pérez, J. (2020). Structural health monitoring for advanced composite structures: a review. Journal of Composites Science, 4(1), 13.

101. Van Driessche, A., Aggelis, D. G., & Tsangouri, E. (2021). Complex fracture on thin-wall textile reinforced cement (TRC) shells monitored by acoustic emission. Thin-Walled Structures, 167, 108216.

102. Luyckx, G., Voet, E., Lammens, N., & Degrieck, J. (2010). Strain measurements of composite laminates with embedded fibre Bragg gratings: Criticism and opportunities for research. Sensors, 11(1), 384-408.

103. Zanjani, J. S. M., Al-Nadhari, A. S., & Yildiz, M. (2018). Manufacturing of electroactive morphing carbon fiber/glass fiber/epoxy composite: process and structural monitoring by FBG sensors. Thin-Walled Structures, 130, 458-466.

104. Zanjani, J. S. M., Louyeh, P. Y., Tabrizi, I. E., Al-Nadhari, A. S., & Yildiz, M. (2021). Thermo-responsive and shape-morphing CF/GF composite skin: Full-field

experimental measurement, theoretical prediction, and finite element analysis. Thin-Walled Structures, 160, 106874.

105. Haltmeier, M., & Nguyen, L. V. (2020). Regularization of inverse problems by neural networks. arXiv preprint arXiv:2006.03972.

106. Papadopoulos, V., Soimiris, G., Giovanis, D. G., & Papadrakakis, M. (2018). A neural network-based surrogate model for carbon nanotubes with geometric nonlinearities. Computer Methods in Applied Mechanics and Engineering, 328, 411-430.

107. Oboe, D., Colombo, L., Sbarufatti, C., & Giglio, M. (2021). Shape sensing of a complex aeronautical structure with inverse finite element method. Sensors, 21(4), 1388.

108. Esposito, M., & Gherlone, M. (2021). Material and strain sensing uncertainties quantification for the shape sensing of a composite wing box. Mechanical Systems and Signal Processing, 160, 107875.

109. You, R., Ren, L., Yuan, C., & Song, G. (2021). Two-dimensional deformation estimation of beam-like structures using inverse finite-element method: theoretical study and experimental validation. Journal of Engineering Mechanics, 147(5), 04021019.

110. You, R., & Ren, L. (2021). An enhanced inverse beam element for shape estimation of beam-like structures. Measurement, 181, 109575.

111. Xu, H., Zhou, Q., Yang, L., Liu, M., Gao, D., Wu, Z., & Cao, M. (2020). Reconstruction of full-field complex deformed shapes of thin-walled special-section beam structures based on in situ strain measurement. Advances in Structural Engineering, 23(15), 3335-3350.

112. Zhao, F., Bao, H., Xue, S., & Xu, Q. (2019). Multi-objective particle swarm optimization of sensor distribution scheme with consideration of the accuracy and the robustness for deformation reconstruction. Sensors, 19(6), 1306.

113. Zhao, Y., Du, J., Bao, H., & Xu, Q. (2018). Optimal sensor placement for inverse finite element reconstruction of three-dimensional frame deformation. International Journal of Aerospace Engineering.

114. Ghasemzadeh, M. and Kefal, A. (2021) Optimization of Sensor Placement for Stiffened Marine Panels Using Coupled Genetic Algorithm, and Inverse Finite Element Method. In 34th Asian-Pacific Technical Exchange and Advisory Meetings on Marine Structures, Istanbul, Turkey.

115. Kefal, A., & Oterkus, E. (2017). Shape Sensing of Aerospace Structures by Coupling Isogeometric Analysis and Inverse Finite Element Method. In 58th AIAA/ASCE/AHS/ASC Structures, Structural Dynamics, and Materials Conference (p. 0427).

116. Kefal, A., Diyaroglu, C., Yildiz, M., & Oterkus, E. (2022). Coupling of peridynamics and inverse finite element method for shape sensing and crack propagation

monitoring of plate structures. Computer Methods in Applied Mechanics and Engineering, 391, 114520.

117. Tessler, A., Roy, R., Esposito, M., Surace, C., & Gherlone, M. (2018). Shape sensing of plate and shell structures undergoing large displacements using the inverse finite element method. Shock and Vibration, 2018.

118. Cerracchio, P., Gherlone, M., & Tessler, A. (2015). Real-time displacement monitoring of a composite stiffened panel subjected to mechanical and thermal loads. Meccanica, 50(10), 2487-2496.

119. Colombo, L., Oboe, D., Sbarufatti, C., Cadini, F., Russo, S., & Giglio, M. (2021). Shape sensing and damage identification with iFEM on a composite structure subjected to impact damage and non-trivial boundary conditions. Mechanical Systems and Signal Processing, 148, 107163.

120. Hughes, T. J., & Brezzi, F. (1989). On drilling degrees of freedom. Computer methods in applied mechanics and engineering, 72(1), 105-121.

121. Tessler, A., Riggs, H. R., & Dambach, M. (1999). A novel four-node quadrilateral smoothing element for stress enhancement and error estimation. International journal for numerical methods in engineering, 44(10), 1527-1543.

122. Stolarski, T., Nakasone, Y., & Yoshimoto, S. (2018). Engineering analysis with ANSYS software. Butterworth-Heinemann.

123. Kreja, I., & Schmidt, R. (2006). Large rotations in first-order shear deformation FE analysis of laminated shells. International Journal of Non-Linear Mechanics, 41(1), 101-123.

124. Kefal, A., & Tessler, A. (2021). Delamination damage identification in composite shell structures based on Inverse Finite Element Method and Refined Zigzag Theory. In Developments in the Analysis and Design of Marine Structures (pp. 354-363). CRC Press.

125. Mindlin, R. (1951). Influence of rotatory inertia and shear on flexural motions of isotropic, elastic plates.

126. Kefal, A., Mayang, J. B., Oterkus, E., & Yildiz, M. (2018). Three dimensional shape and stress monitoring of bulk carriers based on iFEM methodology. Ocean Engineering, 147, 256-267.

LIST OF PUBLICATIONS

1. Abdollahzadeh, M.A., Kefal, A., Yildiz, M., 2020. A comparative and review study on shape and stress sensing of flat/curved shell geometries using C0-continuous family of iFEM elements. Sensors, 20(14), p.3808. https://doi.org/10.3390/s20143808

2. Abdollahzadeh, M.A., Tabrizi, I.E., Kefal, A. and Yildiz, M., 2021. A combined experimental/numerical study on deformation sensing of sandwich structures through inverse analysis of pre-extrapolated strain measurements. Measurement, 185, p.110031. https://doi.org/10.1016/j.measurement.2021.110031

3. Abdollahzadeh, M.A., H.Q. Ali., Yildiz, M., and Kefal, A., 2022. Experimental and Numerical Investigation on Large Deformation Reconstruction of Thin Laminated Composite Structures using Inverse Finite Element Method, Thin-walled structures Vol. 178 p. 109485 . https://doi.org/10.1016/j.tws.2022.109485

4. Abdollahzadeh, M.A., Yildiz, M. and Kefal, A., 2021. Three-Dimensional Shape Sensing of a Representative Ship-Hull Cross-Section Based on Inverse Finite Element Method. In 34th Asian-Pacific Technical Exchange and Advisory Meetings on Marine Structures, Istanbul, Turkey.

5. Abdollahzadeh, M.A., Kefal, A. and Yildiz, M., 2022. Shape Sensing of a Doubly Curved Aft Fuselage Panel using Inverse Finite Element Method, IEEE International Workshop on Metrology for Aerospace, Italy, June 27-29. https://doi.org/10.1109/MetroAeroSpace54187.2022.9856084